



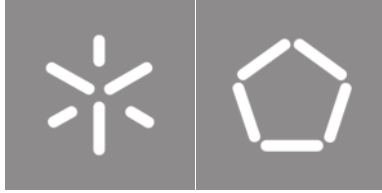
Universidade do Minho

Escola de Engenharia

José Nuno Rocha Gama

**Integration of 2D Materials in Biomimetic
Photonic Structures**

October, 2022



Universidade do Minho

Escola de Engenharia

José Nuno Rocha Gama

**Integration of 2D Materials in Biomimetic
Photonic Structures**

Master Thesis
Master in Physics Engineering
Devices, Microsystems and Nanotechnologies

Work developed under the supervision of:

Dr. Martin Lopez-Garcia
Professor Dr. Pedro Alpuim

COPYRIGHT AND TERMS OF USE OF THIS WORK BY A THIRD PARTY

This is academic work that can be used by third parties as long as internationally accepted rules and good practices regarding copyright and related rights are respected.

Accordingly, this work may be used under the license provided below.

If the user needs permission to make use of the work under conditions not provided for in the indicated licensing, they should contact the author through the RepositoriUM of Universidade do Minho.

License granted to the users of this work



**Creative Commons Attribution-NonCommercial-ShareAlike 4.0 International
CC BY-NC-SA 4.0**

<https://creativecommons.org/licenses/by-nc-sa/4.0/deed.en>

Acknowledgements

Five years have passed. I grew up, learned novel subjects, and made new friends. University is a tumultuous phase, full of courses to study and deadlines to meet, which can only be successfully overcome with commitment and daily work (hard sometimes and sometimes not so much). I leave the motivation to wake up and to continue working forward to myself, who always kept the will to fulfill my life commitments. I also dedicate this to my grandmother, who always insisted on wanting to see her grandson a graduated engineer: *o prometido é devido, Vó!*

I would like to thank my advisor Dr. Martin Garcia-Lopez, head of the Natural and Artificial Photonic Structures research group at the International Iberian Nanotechnology Laboratory, whose support was crucial, for his constant guidance throughout my work and for his deep knowledge in each of the steps I took in this dissertation. I also thank Professor Dr. Pedro Alpuim for being my supervisor from the University of Minho and for trusting my abilities to develop this assigned project.

My appreciation to Miguel Castillo and Francisca Guedes, from the NAPS research group, and Vítor Silva and João Fernandes, from the 2D Materials and Devices research group, for all their help with equipment, measurements, laboratory miscellaneous, and material supply and for the quality time spent beyond researching. To the INL and all its people, thank you for my stay! I was a truly welcome guest. I also thank my colleagues Diogo Baptista and Rafael Vilarinho for the subjects' explanations, the borrowed notes, the solved exercises, and the key support throughout our college course.

Finally, I would like to thank my parents for supporting and encouraging me to work and continue my academic path.

STATEMENT OF INTEGRITY

I hereby declare having conducted this academic work with integrity. I confirm that I have not used plagiarism or any form of undue use of information or falsification of results along the process leading to its elaboration.

I further declare that I have fully acknowledged the Code of Ethical Conduct of the Universidade do Minho.

(Place)

(Date)

Assinado por: **José Nuno Rocha Gama**
Num. de Identificação: 15931355
Data: 2022.12.16 15:24:00+00'00'

(José Nuno Rocha Gama)

“The saddest aspect of life [...] is that science gathers knowledge faster than society gathers wisdom.” (Isaac Asimov, 1988)

Abstract

Integration of 2D Materials in Biomimetic Photonic Structures

Today's society lives in constant dependence on electricity. It is common sense to look for sources that produce electricity with a minimal ecological footprint such as solar energy. The state-of-the-art of solar energy conversion is a very optimistic but uninspiring scenario since the highest efficiency research cell does not exceed 47.1%. Using bioinspired photonic nanostructures, it is possible to improve light-matter interactions of additional light-harvesting layers from volumes as reduced as two-dimensional materials on top of these cells, through techniques available in cleanroom-free environments. This allows a simpler and lower-cost way to increase the performance of the final device without increasing its footprint. The reproduction of sinusoidal optical diffraction gratings (*nanowrinkles*) inspired in epidermal cells' walls of angiosperms to enhance light-matter interactions of adjacent graphene was studied.

A reproducible process was developed for the manufacture of *nanowrinkles* with periodic features of 600, 800, and 1000 nm composed of PDMS activated by an oxygen plasma treatment showing a sinusoidal profile with R^2 of 85.94%, 78.76%, and 97.00% respectively. Almost all fabricated samples behaved as optical diffraction gratings in angular spectrophotometry measurements.

A method for integrating graphene grown by chemical vapor deposition into the aforementioned nanostructures was developed, based on a wet transfer. Fabricated samples with transferred graphene maintained the same periodicity, showing a sinusoidal profile with R^2 of 80.41%, 62.60%, and 43.32% respectively. Optically, the combination of the nanostructure with the material kept the behavior of a diffraction grating. Raman's spectroscopy measurements on transferred graphene onto oxygen plasma-treated PDMS showed a 2D/G bands ratio and G band spectral position expected from a monolayer. Due to the material's brittleness resulting from the oxygen plasma treatment of PDMS, consistently oriented cracks appeared across the entire surface, inhibiting electrical conduction in transferred graphene.

An implementation of gold contacts by sputtering with a copper adhesion layer spaced by 200 μm was developed so that crack-free continuous areas of graphene connected side-by-side contacts. This technique allowed the injection of electric current when voltage was applied between contacts. Resistance was measured with values $R \sim 10^1 - 10^2 \text{ k}\Omega$.

Keywords: solar energy, bioinspired, light-matter, light-harvesting, cleanroom-free, footprint, *nanowrinkles*, PMDS, oxygen plasma, graphene, wet transfer

Integração de Materiais 2D em Estruturas Fotónicas Biomiméticas

A sociedade atual vive em constante dependência de energia elétrica. É do senso comum procurar fontes produtoras de energia elétrica com pegada ecológica mínima, tais como a energia solar. O estado da arte da conversão energética solar é um cenário muito otimista, mas pouco inspirador, já que a célula solar investigada de maior rendimento não ultrapassa os 47.1%. Utilizando nanoestruturas fotónicas bioinspiradas, é possível melhorar interações luz-matéria de camadas adicionais de colheita luminosa de volumes tão reduzidos quanto de materiais bidimensionais no topo destas células, utilizando técnicas disponíveis em ambientes fora de sala-limpa. Isto permite aumentar o rendimento do dispositivo final sem aumentar consideravelmente a sua dimensão, de forma mais simples e barata. Estudou-se a reprodução de redes de difração óticas sinusoidais (*nanorrugas*) bioinspiradas em paredes celulares epidérmicas de angiospermas para melhorar as interações luz-matéria de grafeno adjacente.

Desenvolveu-se um processo consistente de fabrico de *nanorrugas* periódicas de 600, 800 e 1000 nm compostas por PDMS tratado por plasma de oxigénio mostrando um perfil sinusoidal com R^2 de 85.94%, 78.76% e 87.00%, respetivamente. Quase todas as amostras fabricadas comportaram-se como redes de difração ótica em medições de espectrofotometria angular.

Desenvolveu-se um método de integração de grafeno crescido por deposição química a vapor nas nanoestruturas mencionadas acima, com base numa transferência húmida. Amostras fabricadas com grafeno transferido mantiveram a periodicidade, mostrando um perfil sinusoidal com R^2 de 80.41%, 62.60% e 43.32%, respetivamente. Óticamente, a combinação da nanoestrutura com o material manteve o comportamento de uma rede de difração. Medições em espectroscopia de Raman sobre grafeno transferido para PDMS tratado com plasma de oxigénio mostraram um rácio de bandas 2D/G e posição espectral de banda G esperados de uma monocamada. Devido à fragilidade da superfície de PDMS tratada, apareceram fendas que inibem a condução elétrica no grafeno transferido, consistentemente orientadas.

Foi desenvolvida uma implementação de contactos de ouro por pulverização catódica, com camada de adesão de cobre, distanciados por 200 μm , de forma que zonas contínuas de grafeno entre fendas conectassem contactos lado a lado. Esta técnica permitiu a injeção de corrente elétrica quando aplicada tensão entre contactos, tendo sido medidas resistências com valores $R \sim 10^1 - 10^2 \text{ k}\Omega$.

Palavras-chave: luz-matéria, colheita luminosa, *nanorrugas*, PDMS, plasma de oxigénio, grafeno

Contents

List of Figures	xiii
List of Tables	xvii
Glossary	xviii
Acronyms	xx
Symbols	xxii
1 Introduction	1
1.1 Framing and Motivation	1
1.1.1 Natural Photonics Research	1
1.1.2 Optoelectronic Devices	2
1.1.3 Improving Conventional Devices	3
1.2 State of The Art	4
1.2.1 Two-dimensional Materials for Optoelectronic Applications	4
1.2.2 Light-Matter Interaction Enhancement on 2D Materials	6
1.2.3 Wood's Anomalies on Optical Diffraction Gratings	7
1.2.4 Reconfigurable and Programmable Nanostructures	9
1.2.5 Large-Area 2D Material Transfer	11
1.3 Measurement Methods	13
1.3.1 Atomic Force Microscopy	14
1.3.2 Fourier Imaging Setup	14
1.3.3 Optical Microscopy	16
1.3.4 Raman's Spectroscopy	17
1.3.5 Scanning Electron Microscopy	17

2	Photonic Nanostructure Fabrication	18
2.1	Design	18
2.1.1	Substrate Choice and Considerations	20
2.1.2	Skin Layer Definition and Tailoring	20
2.2	Conditions and Parameters	23
2.3	Fabrication Method	23
2.3.1	Calibration of Conditions	25
2.4	Morphological Analysis	27
2.5	Optical Characterization	31
3	Integration of the Two-dimensional Material	34
3.1	Graphene as an Optoelectronic Material	34
3.2	Graphene Integration Methodology	35
3.3	Surface Quality Control	36
3.4	Morphological Analysis	38
3.5	Optical Characterization	43
4	Optoelectronic Wrinkled Graphene	45
4.1	Electrical Contacts	45
4.1.1	Conductive Silver Ink	45
4.1.2	Gold Sputtering	46
4.2	Electronic Inspection	49
5	General Conclusions	51
5.1	Future Perspectives	52
	Bibliography	53
	Appendices	
A	Pictures and Protocols	63
A.1	<i>Nanowrinkles'</i> Fabrication	63
A.2	Graphene on Copper Wet Transfer Protocol	63
A.3	Optoelectronic Experiments	66
B	Statistical Analysis	67
B.1	Useful Equations	67
B.2	Raw Data	68
B.3	Processed Data	69

C	Additional Measurements	72
C.1	Optical Microscopy	72
C.2	Atomic Force Microscopy	75
C.3	Raman's Spectroscopy	77
C.4	Scanning Electron Microscopy	80
C.5	Angular Reflection Spectrophotometry	82

List of Figures

1	Natural biophotonics	2
2	Junction-np working principle	3
3	Reported timeline of research solar cell energy conversion efficiencies since 1976	4
4	2D Materials' Absorbance in VIS/NIR	6
5	Double-mirror optical microcavity schematic	7
6	Double-mirror optical microcavity transmission spectrum	7
7	Single-slit optical diffraction experiment	8
8	Optical diffraction grating signal convention	9
9	Cross-section schematics of growth-induced surface instabilities	10
10	Theoretical 3D phase diagram of the various surface instability patterns	10
11	Schematic wet transfer process of 2DM	11
12	Schematic of the dry transfer process of 2DM	12
13	Schematic of the mechanical transfer process of 2DM	13
14	Schematic of electrochemical transfer process of 2DM	13
15	Schematic of the full Fourier microscope setup used throughout the dissertation.	15
16	Cropped section from WD10.1 Spot 1	16
17	FFT of figure 16	16
18	Solar irradiance spectrum above Earth's atmosphere and at sea level	18
19	Cross-section sketch of the desired 3D nanostructure	19
20	Chemical structure of di-methylsiloxane.	20
21	Effect of the oxygen plasma treatment on PDMS's surface.	21
22	Condensation and Hydrolysis reactions of silanol groups.	21
23	Water-in-air contact angles as a function of aging time	22
24	Chemical changes on PDMS's samples after resting time	22
25	Substrate stretching diagram of the method used in fabrication	24
26	Batch of 3 stretched samples	24

LIST OF FIGURES

27	HARRICK PLASMA high power plasma cleaner	25
28	Sample placement diagram inside the vacuum chamber	25
29	Statistical analysis of fabrication method with varying resting time after oxygen plasma treatment	26
30	Prediction of oxygen plasma intensity distribution inside the vacuum chamber	26
31	Type #1 (larger Δ) sample	27
32	Raman spectra of oxygen plasma-treated and untreated PDMS	28
33	AFM-measured 3D representation of a type #2 sample	28
34	AFM-measured plots of samples of different types	29
35	Cross-section profile over plots from figure 34.	29
36	SEM images of type #1 sample from WD7	30
37	SEM images of type #1 sample from RB8	31
38	Angular reflectance plots of fabricated samples	32
39	Summary diagram of the complete fabrication procedure of the device	35
40	Statistical analysis of fabrication method with graphene transfer included	36
41	Relationship between PDMS swelling ratio on various solvents and their solubility parameter	37
42	4 \times objective images of flat PDMS treated by oxygen plasma after pure acetone bath with different duration	38
43	Oxygen plasma overexposed wrinkled graphene samples	38
44	Raman analysis of graphene transferred onto different substrates	39
45	Raman analysis of graphene transferred onto oxygen plasma-treated PDMS with cracks	41
46	AFM-measured 3D representation of type #3 sample with transferred graphene	41
47	AFM-measured plots of samples with transferred graphene	42
48	Cross-section profile over plots from figure 47.	42
49	Angular reflectance plot of a type #1 sample	43
50	Conductive silver ink contacts implementation and conductance test schematic	46
51	Conductive silver ink contacts implementation on graphene on glass.	46
52	Laser-inscribed PET mask layout	47
53	Samples with a shadow mask, tapped to a silicon wafer right after sputtering.	47
54	Contact distance of 1 <i>mm</i>	47
55	Contact distance of 200 μm	48
56	Contact distance of 200 μm perpendicular to the stretching direction	48
57	Electrical needle probes setup schematics	49
58	Electrical needle probes setup picture	49
59	Current–voltage characteristics of the final device	50
60	Elastomer base/curing agent kit	63

61	Conventional binder paper clamp	63
62	Cut PDMS strips on glass slides	63
63	First fastened clamp on each sample	63
64	<i>RS PRO™ Conductive Silver Ink</i>	66
65	Conductive Silver Ink contact implementation on a batch of samples	66
66	Test PET shadow mask with different inscribed layouts	66
67	PET shadow mask placed on top of samples.	66
68	Samples attached to a silicon wafer before sputtering.	66
69	Light diffraction enhancement of sputtered gold contacts	66
70	WB1.1 Spot 1, 40×	68
71	WB2.1 Spot 1, 40×	68
72	WB3.1 Spot 1, 40×	68
73	WB4.1 Spot 1, 40×	68
74	WD2.1 Spot 1, 40×	68
75	WD3.1 Spot 1, 40×	68
76	WD5.1 Spot 1, 40×	68
77	WD7.1 Spot 1, 40×	68
78	WD8.1 Spot 1, 40×	68
79	WD9.1 Spot 1, 40×	68
80	WD10.1 Spot 1, 40×	68
81	RB5.1 Spot 1, 40×	68
82	RB6.1 Spot 1, 40×	68
83	First calibration attempt of the oxygen plasma up time	69
84	Type #2 sample	72
85	Type #3 sample	72
86	Oxygen plasma-treated flat PDMS sample after acetone bath with 15m intervals	73
87	Oxygen plasma-treated flat PDMS sample treated after acetone bath with 30m intervals	73
88	Oxygen plasma-treated flat PDMS sample after acetone bath with 60m intervals	73
89	Type #1 wrinkled graphene sample overexposed with oxygen plasma	74
90	Type #2 wrinkled graphene sample overexposed with oxygen plasma	74
91	Gold contacts on wrinkled graphene	74
92	3D representation of type #1 sample of WD7	75
93	3D representation of type #3 sample of WD7	75
94	3D representation of type #1 sample of WD2	75
95	2D topographical plot of type #1 sample of WD2	75
96	3D representation of type #2 sample of WD2	75

LIST OF FIGURES

97	2D topographical plot of type #2 sample of WD2	75
98	3D representation of type #3 sample of WD2	76
99	2D topographical plot of type #3 sample of WD2	76
100	3D representation of type #1 sample of RB6	76
101	3D representation of type #2 sample of RB6	76
102	Theoretical normalized Raman's spectrum of pristine PDMS	77
103	Typical Raman's spectrum of fused silica	77
104	Raman's spectrum of monolayer graphene on a 2 mm SiO ₂ substrate. Retrieved from [94].	77
105	Measured section of flat pristine PMDS	77
106	Raman's spectra obtained on flat PDMS	77
107	Measured section of oxygen plasma-treated flat PDMS	77
108	Raman's spectra obtained on flat treated PDMS	77
109	Measured section of graphene on glass	78
110	Raman's spectra obtained on graphene on glass	78
111	Measured section of graphene on untreated PDMS	78
112	Raman's spectra obtained on graphene on untreated PDMS	78
113	Measured section of graphene on treated PDMS (no delay)	78
114	Raman's spectra obtained on graphene on treated PDMS (no delay)	78
115	Measured section of graphene on treated PDMS (72h delay)	79
116	Raman's spectra obtained on graphene on treated PDMS (72h delay)	79
117	WD7.1, 16 244×	80
118	WD7.1, 5 154×	80
119	WD7.2, 872×	80
120	WD7.2, 7 778×	80
121	WD7.2, 6 400×	80
122	WD7.2, 39 481×	80
123	WD7.3, 289×	81
124	WD7.3, 1 233×	81
125	WD7.3, 3 563×	81
126	WD7.3, 7 605×	81
127	ARS RB6.2 (no graphene)	82
128	ARS RB6.3 (no graphene)	82
129	ARS WD2.1	82
130	ARS WD9.1	82
131	ARS WD2.2	82

List of Tables

1	Noticeable experimental quantities of hexagonal TMDC monolayers	5
2	Representative transfer methods for 2DMs	13
3	Comparison between measured Λ at AFM and microscope inspection-based	30
4	Graphical analysis of G and 2D Raman band peaks of graphene transferred onto different types of substrates	40
5	Comparison between measured Λ of samples with graphene at AFM and microscope inspection-based	43
6	Graphene conduction test results on flat substrates	46
7	Λ values for fabricated batches with no delay time after plasma treatment	69
8	Statistical analysis of table 7.	70
9	Λ values for fabricated batches with varying delay time after plasma treatment and respective statistical analysis	70
10	Λ values for fabricated batches with varying delay time after plasma treatment	71
11	Statistical analysis of table 10.	71

Glossary

- allotrope** Allotropy is the property of some chemical elements to exist in two or more different forms in the same physical state. These forms are called allotropes and are caused by the way atoms of the structure are bonded with each other. Examples of carbon allotropes are fullerenes as a 0D, nanotubes as a 1D, and graphite and diamond as a 3D material. 5
- angiosperms** Angiosperms are vascular plants whose seeds are developed after eggs, i.e., feminine gametes are fertilized in an ovary, usually inside a flower. Angiosperms' flowers also have male reproductive organs producing pollen grains or tubes. These species require the crossing of gametes between different individuals for following fertilization [1]. 10, 51
- charge-coupled device** A charge-coupled device is an integrated circuit containing an array of linked or coupled capacitors linked with photodetectors. These capacitors at each light exposure can charge up by photovoltaic effect. The charges on each pixel of the first row are read by a read-out register, then receiving the charges from the second row and so on [2]. xx, 14
- Fast Fourier Transform** Fast Fourier Transform is an algorithm that quickly calculates the Discrete Fourier Transform or its inverse. Fourier analysis converts a signal from the original domain to a frequency domain representation and vice versa. The discrete Fourier transform is obtained by decomposing a sequence of values into components of different frequencies. 16

- low-pass filter** A low-pass filter passes signals with a frequency lower than a selected cutoff frequency and attenuates signals with higher frequencies. In optics it is also known as anti-aliasing or blur filter and smooths up the image since outline pixels are the ones with the higher frequencies, thus their intensity being attenuated [3]. 14
- optoelectronic** Optoelectronics is the field in charge of studying the process of transforming light into electrical energy or the other way around. It is usually considered a sub-field of photonics. Optoelectronic devices are electrical-to-optical or optical-to-electrical transducers, or systems that base their working principle on such transducers [4]. 2, 4, 20, 34, 45, 48, 51, 52
- polarized** Polarization is a spatial property of electromagnetic waves. These waves have an electric and a magnetic field orthogonally oscillating between an absolute maximum and minimum. When the light gets reflected on a flat surface, it follows a constant plane of incidence. P-polarized light comes from *parallel*, which means the light wave's electric field is parallel to this plane. On the other hand, s-polarized comes from *senkrecht*, German for perpendicular, meaning this electric field is orthogonal with that plane. 31
- spin coating** Spin coating is a method for evenly dispersing thin films over flat substrates. Typically, a little quantity of coating material is deposited to the substrate's center, which is either not spinning at all or spinning at a low speed. The coating material is subsequently disseminated by centrifugal force while the substrate is rotated at a speed of up to 10,000 rpm. Spin coaters, or simply spinners, are devices used for spin coating [5]. 34
- Young's modulus** A numerical constant that describes the elastic properties of a solid undergoing tension or compression in only one direction. This constant is a measure of the ability of a material to withstand changes in length when under lengthwise tension or compression. It is a specific form of Hooke's law of elasticity. The international unit of Young's modulus is newtons per square meter (Nm^{-2}) but it can be also measured in pascals (Pa). 5, 10, 11, 20, 23

Acronyms

2DM	two-dimensional material 4, 6, 7, 9, 11, 12, 13, 18, 19, 34, 35, 40, 49, 51
3D	three-dimensional xviii, 14, 18, 19, 20, 27, 28, 31, 41, 75, 76
AFM	Atomic Force Microscopy 14, 28, 29, 30, 41, 42, 43
BF	bright-field microscopy 27, 38, 68, 72, 73, 74
CCD	charge-coupled device 14, 16
CVD	Chemical Vapor Deposition 11, 34, 35
DC	direct current 49
DF	dark-field microscopy 38, 68, 73
LASER	light amplification by stimulated emission of radiation 7, 14, 46, 47
NIR	near-infrared 2, 6, 18, 31, 51
PDMS	poly(di-methylsiloxane) 20, 21, 22, 24, 27, 28, 35, 36, 37, 38, 39, 40, 41, 45, 46, 51, 52, 63, 73, 77, 78, 79
PMMA	poly(methyl methacrylate) 11, 12, 34, 35, 36, 37, 42, 52
SEM	Scanning Electron Microscopy 17, 30, 31, 80, 81
SSA	specific surface area 5, 34
TMDCm	Transition Metal Dichalcogenide monolayer 4, 5, 6, 34, 51

VIS visible 2, 6, 14, 16, 18, 20, 31, 34, 51

Symbols

- a lattice constant 5
- ϵ_M substrate pre-stretching percentage 10, 11, 23, 24
- M ratio of mixed materials to their mass 23
- π the numerical value of pi 10, 11
- A grating features' amplitude 11, 23, 29, 33, 38, 42
- Λ grating features' period 8, 9, 10, 11, 16, 19, 23, 25, 26, 27, 29, 30, 32, 33, 36, 38, 42, 43, 47, 69, 70, 71
- λ photon wavelength 2, 7, 8, 9, 32, 33, 43

Introduction

Brief framing and motivation of the dissertation project, theoretical introduction of the topics covered (State of the Art) and the measurement methods used.

In this introductory chapter, the current cons of the most studied light-harvesting materials and their problematics for light-matter interactions are defined. Optical diffraction gratings as suitable nanostructures to enhance such interactions are analyzed. Methodologies for the fabrication of devices based on these nano-architectures along with the integration of two-dimensional materials are discussed. Finally, measurement methods and setups used throughout this dissertation are presented.

1.1 Framing and Motivation

Capturing light is a phenomenon that has been on this planet for over 3400 million years [6]. In the attempt to survive, nature is continuously adapting every living species to the environment, as well as their fundamental processes and the structures behind them. Light-interacting processes among living beings were also tuned depending on each purpose [7]. Using nature as a guideline to manufacture new light-harvesting devices based on two-dimensional materials could lead to greater device efficiency in less space.

1.1.1 Natural Photonics Research

Natural photonics studies light-interacting processes in nature. This is a sub-field of the very broad field of photonics. Biomimetic photonic structures are artificial photonic structures mimicking existing natural ones. These natural structures can go from a simple *Diplazium tomentosum* leaf to a complex *Morpho rhetenor* wing, as shown in figure 1.

The wave-like behavior of light allows for constructive and destructive interference. Photonics uses this principle to manipulate, generate and detect light in a huge range of ways with multiple scientific

objectives in mind, making use of natural structures as blueprints for artificial bioinspired photonic structures. The motivation behind this research field matches the possibility of creating structures with more resilient optical properties (e.g., structural colors in contrast to dye-dependant colors) using a wide range of transparent materials provided by the correct nanostructuring of the layers in the system. Moreover, nanostructures found in nature are usually more robust to drawbacks relative to artificial designs.

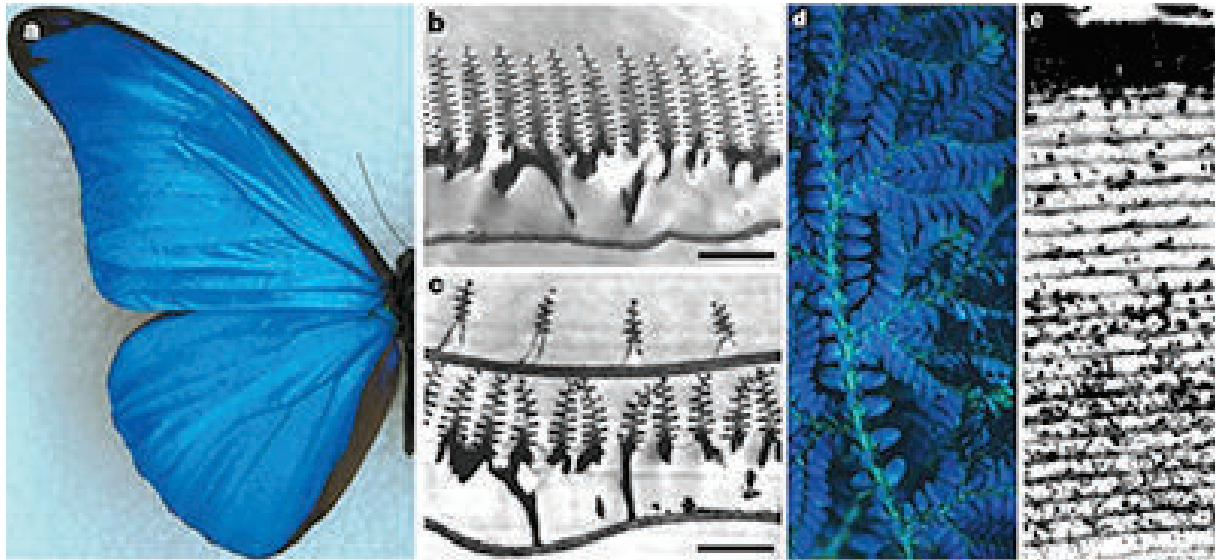


Figure 1: **a**, Real colour image of a *M. rhetenor* wing. **b**, Bar $1.8 \mu\text{m}$, TEM of wing's cross-section of *M. rhetenor*. **d**, Blue iridescence in *Selaginella*. **e**, TEM section of a leaf from *Diplazium tomentosum*. Adapted from [8].

In this case, natural photonic structures will be sought in order to produce diffractive effects in the visible (VIS)+near-infrared (NIR) spectrum of light, such as in optical diffraction gratings. The replication of this phenomenon is frequent in nature, motivated by the importance of color in mechanisms of survival or breeding of species.

1.1.2 Optoelectronic Devices

The main reason humanity adapted light-interacting processes from nature was to convert light into usable energy as electricity. Devices capable of producing such conversion processes are called **optoelectronic** devices. The manufacturing of these devices belongs to a large, thriving, and well-established industry in modern society with a vast number of applications such as solar energy, light detection, and digital photography.

The most common building blocks of conventional **optoelectronic** devices are semiconductor p-n junctions. When a sufficiently energetic beam of photons illuminates an insulated p-n junction, $\lambda \leq \frac{hc}{E_{gap}}$, with E_{gap} being the band gap between the top of the valence band and the bottom of the conduction band, the material suffers an internal photoelectric effect. Electrons transit from the valence band to the conduction

band, leaving an empty state – also called hole, in the former, thus generating electron-hole pairs¹ bound by the electrostatic attraction.

The electric field in the junction's depletion zone forces electrons and holes to move into different regions, preventing recombination. The charges created accumulate unevenly on either side, decreasing the junction's potential barrier height. Whenever this barrier disappears, the charge transition from one region to another comes to an end. With this, the electron-hole pairs separation stops and the junction reaches a flat band condition, shown as a constant potential – the photoelectromotive force V_0 (figure 2).

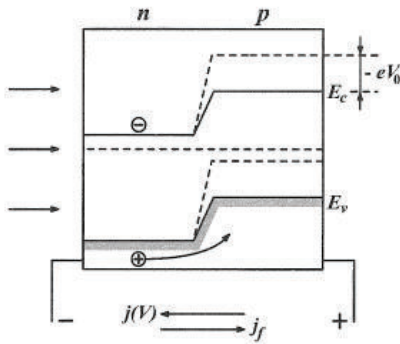


Figure 2: The origin of V_0 at a p-n junction. Dashed lines represent electronic bands in the dark. Lighting causes the barrier height to decrease. The arrows indicate the photocurrent and the current due to the decrease of the barrier. Adapted from [9].

When the depletion zone of the junction is short-circuited, a stationary current proportional to the intensity of the illumination is generated, called photocurrent,

$$j_f = e\bar{G}\beta \quad (1.1)$$

where \bar{G} is the electron-hole pair generation rate near the surface by area unit and β is the fraction of holes created that reach the depletion zone [9].

1.1.3 Improving Conventional Devices

As in every other conversion process, the aim is to maximize its efficiency. The largest source of losses in semiconductor junctions is related to photon absorption with energy much greater than the building material E_{gap} [10]. Charge carriers are created with enormous kinetic energy, which is then dissipated in several collisions, turning into heat, an unpleasant guest in every electronic device, especially in photovoltaic cells [11]. The bulk material selection and its level of purity largely influence the efficiency of the device. The way to maximize photovoltaic efficiency is to achieve the theoretical limit in which all light-generated electron-hole pairs created participate in the photocurrent j_f .

Notably, although the peak value of the spectral distribution of sunlight corresponds to photon energy similar to the E_{gap} of crystalline silicon (1.1 eV), there are currently no devices based on this material with efficiency greater than 27.6% (figure 3). Plus, the active region of any photovoltaic device is just a thin layer on the surface [9].

¹excitons

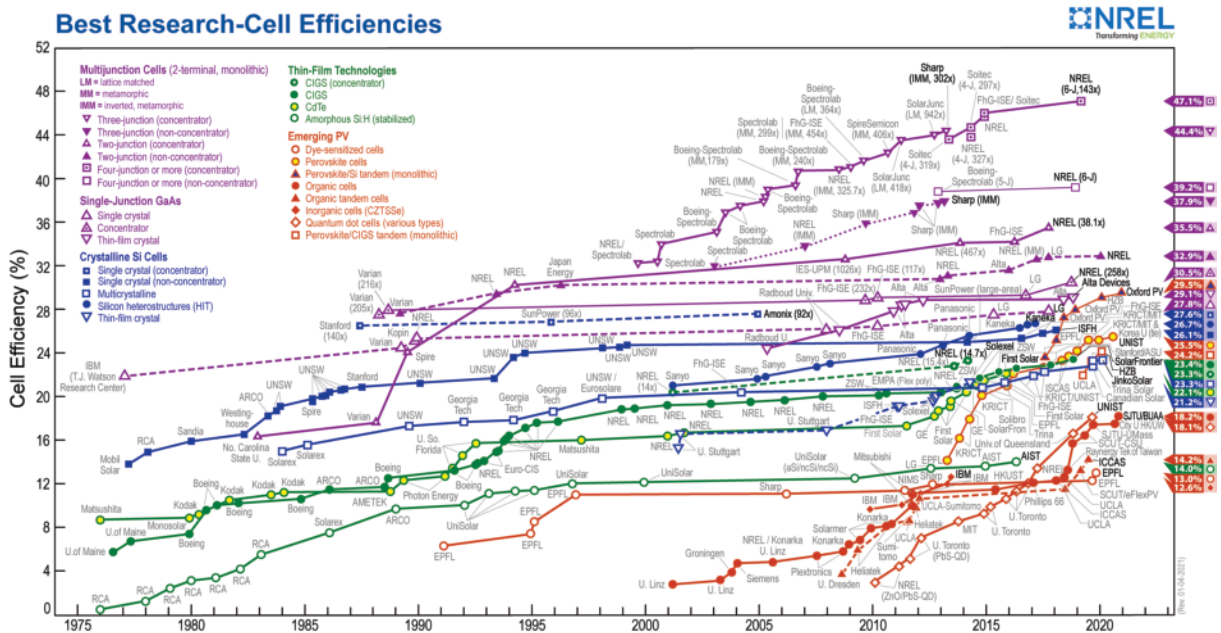


Figure 3: Reported timeline of research solar cell energy conversion efficiencies since 1976. Retrieved from [12].

Two-dimensional materials along with photonic structures can be a viable add-on to existent technology, as its dimensions will not affect the device's footprint, increasing the overall efficiency of the final device. Plus, their thermoelectric properties will not play a role in overheating effects [13]. In the middle term beyond the final scope of this project, it is intended to develop a two-dimensional material (2DM) integration in a cost-effective way into large areas of bioinspired nano-architecture to provide better photovoltaic effects on the 2DM.

1.2 State of The Art

The project in its entirety has extremely recent theoretical foundations. Despite being scientifically well established, all topics covered date back to investigations carried out in the past decade. The gathering of these topics leads to the vanguard in photonic and optoelectronic device development.

1.2.1 Two-dimensional Materials for Optoelectronic Applications

The use of 2DMs for optoelectronic applications, as mentioned above, is one of the most promising research fields at the moment. They have unique electronic and optical properties due to their quantum-mechanical confinement [14].

One strategy for developing a high-efficiency optoelectronic device is to increase the light absorption of these materials. For this purpose, the most investigated 2DMs are graphene and Transition Metal Dichalcogenide monolayer (TMDCm)s.

1.2.1.1 Graphene

Graphene is an *allotrope* of carbon (C) consisting of a single layer of sp^2 bonded atoms arranged in a two-dimensional honeycomb lattice with $a = 2.46 \text{ \AA}$. [15]. Its sp^2 -hybridization causes a trigonal planar molecular geometry [16]. Each carbon atom at the corners has four bonds: one σ -bond with each of the three neighbors and one π -bond oriented in the out-of-plane direction. The σ -bonds have the length of $\approx 1.42 \text{ \AA}$.

Graphene has one of the highest theoretical *specific surface area (SSA)* ($\approx 2630 \text{ m}^2/\text{g}$), leading to a huge area of interaction [17]. Monolayer graphene is a highly flexible material in the out-of-plane direction because of its dimensional shape. However, in the lattice plane it is reported to have a *Young's modulus* $E \approx 1 \text{ TPa}$ [18], almost as much as its *allotrope* diamond (1.22 TPa) [19], the stiffest material known. Moreover, graphene can reach a charge carrier mobility ν_e of $5 \times 10^4 \text{ cm}^2 \text{ V}^{-1} \text{ s}^{-1}$ [20], having higher electrical conductivity than room-temperature metals such as gold, silver, or copper [21]. Regarding this, graphene has a sheet resistance $R_{\square} \sim 10^2 \Omega$ [22]. Plus, its experimental thermal conductivity $k \in [4840, 5300] \text{ W m}^{-1} \text{ K}^{-1}$ [23], much higher than silver's ($429 \text{ W m}^{-1} \text{ K}^{-1}$) [24], the election material for heat dissipation in electronic applications.

1.2.1.2 Transition Metal Dichalcogenide monolayers

TMDCms with hexagonal allotropy are the semiconductor analogs of graphene. They are atomically thin semiconductors of the type MX_2 , with M being a transition-metal atom, e.g. molybdenum (Mo), tantalum (Ta), or tungsten (W), and X a chalcogen² atom such as sulfur (S), selenium (Se), or tellurium (Te). Although they are considered monolayers, structurally these materials consist of one layer of transition-metals in the middle of two layers of chalcogens [25].

In table 1 follows noticeable experimental quantities regarding mechanical, electronic and thermal properties of the most studied hexagonal TMDCms.

Table 1: Noticeable experimental quantities of hexagonal TMDCms.

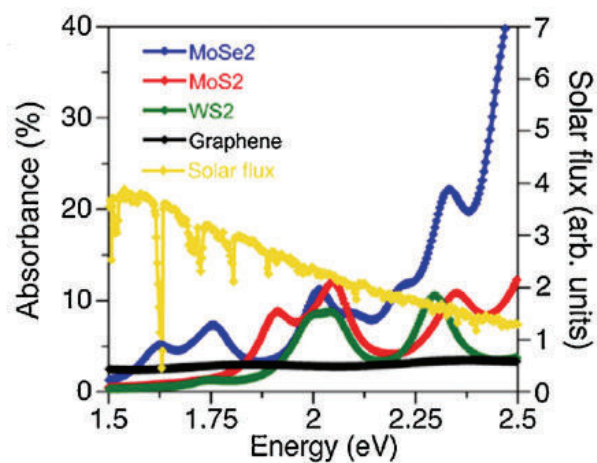
h-TMDCms	a, c (Å)	SSA ($\text{m}^2 \text{ g}^{-1}$)	E (GPa)	ν_e ($\text{cm}^2 \text{ V}^{-1} \text{ s}^{-1}$)	k ($\text{W m}^{-1} \text{ K}^{-1}$)
MoS2	3.17, 5.48 [26]	27.82 [27]	100.99 [28]	>200 [29]	34.5 [30]
MoSe2	3.29, 12.89 [31]	96.9 [32]	350 [33]	50 [29]	54 [30]
WS2	3.16, 12.35 [34]	160 [35]	302.4 [36]	0.2 [29]	32 [30]

²chemical element from group 16 of the periodic table

1.2.2 Light-Matter Interaction Enhancement on 2D Materials

TMDCs strong light-matter interactions can be contrasted with the low light absorption and photoresponsivity of graphene due to the absence of a band gap in the latter [14]. As shown in figure 4, graphene in its undoped state absorbs $\approx 2.3\%$ of the incident light within the VIS+NIR spectrum “as a result of direct electron–hole pair transitions between its lower occupied Dirac cones and the upper unoccupied cones (two inequivalent ones in every Brillouin zone)” [37].

Figure 4: Theoretical absorbance of three TMDC monolayers and graphene, overlapped with incident AM1.5G solar flux in the VIS spectrum. Adapted from [14].



Despite the low overall absorbance, a promising approach is doping these materials, as their band structures allow more electron transitions between bands, meaning a single incidence of a light beam would create more free charge carriers [38].

An alternative solution raises the absorption by increasing the region of the 2DM over which light interacts, for example by coupling the 2DM to an optical cavity of high-quality factor, i.e., by trapping a light beam for a long time near the material [37].

The use of optical cavities involves using metallic structures that influence the final device dimensions and optical properties. Regarding this, it was found that graphene inside a microcavity (figure 5) of two dielectric materials enclosed by two metallic mirrors with a spacing $L \approx \lambda_{cavity}/2 = \lambda/2$, with λ being the incident light wavelength, produces a maximum peak in photocurrent generation (figure 6). This is because the dielectric stack length defines the cavity’s resonating wavelength which corresponds to the transmission spectrum peak when white light is incident [39]. Light-matter interaction enhancement in TMDCs is also possible using similar optical nano-architectures [40].

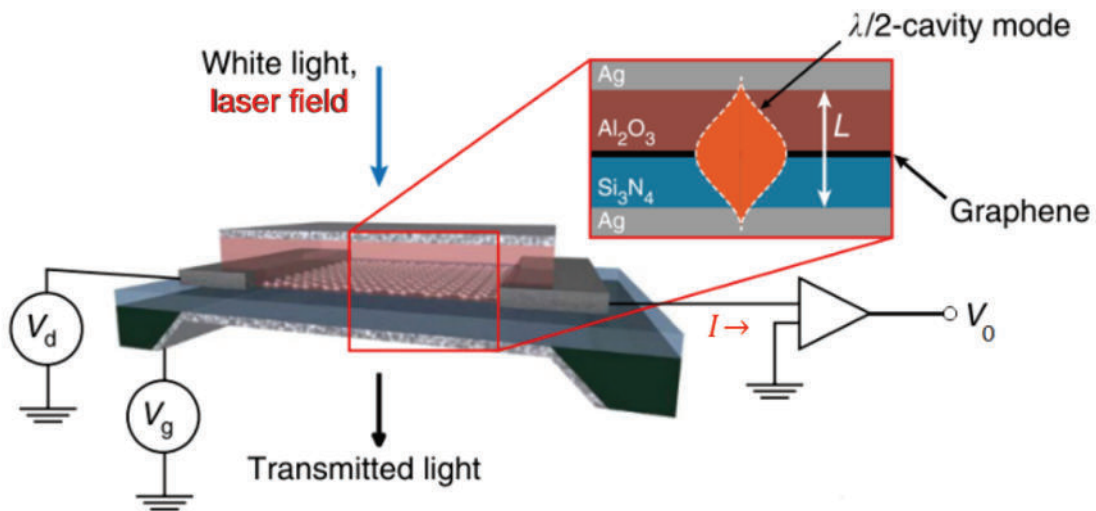


Figure 5: Electrical schematic of a microcavities device. The thickness L of the dielectric stack between the cavity mirrors determines the resonance wavelength λ_{cavity} of the optical microcavity. Adapted from [39].

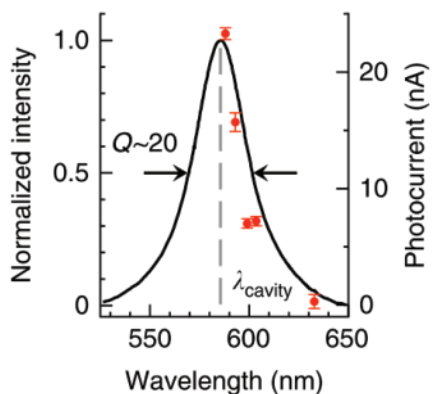


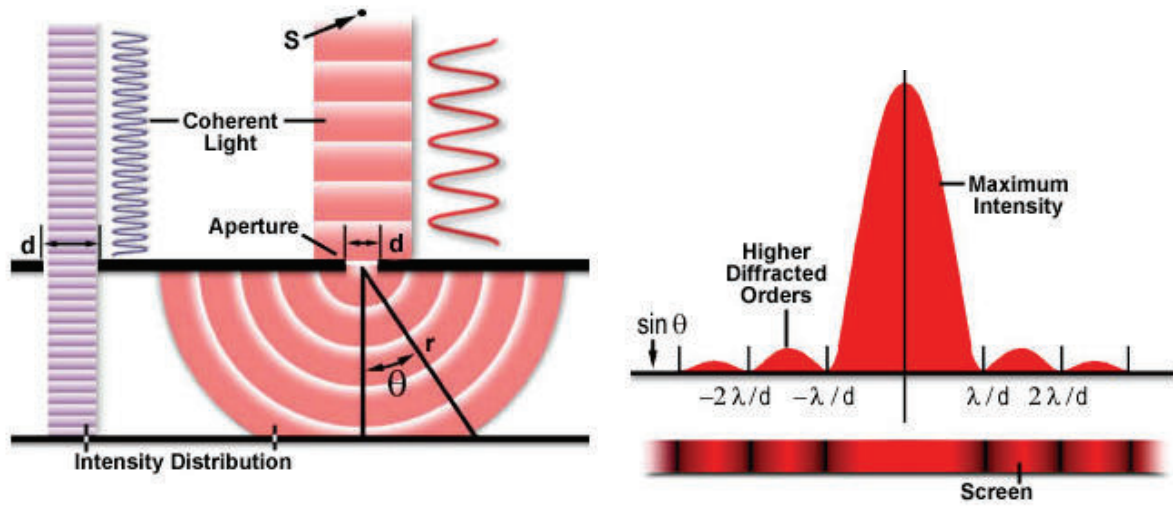
Figure 6: Device's transmission spectrum. Cavity resonance at $\lambda_{cavity} = 585\text{nm}$ with a quality factor of 20. The red dots mean the measured induced photocurrent amplitude by a light amplification by stimulated emission of radiation (LASER) field with variable wavelength. Adapted from [39].

1.2.3 Wood's Anomalies on Optical Diffraction Gratings

The photocurrent generation effect on graphene observed in figure 6 consists in increasing the region of the 2DM over which light interacts with. However, these devices are usually difficult to fabricate, requiring the use of metal layers that can be problematic if transparency is needed. Replicating a periodic superficial corrugation³, could cause a similar effect as the two-mirror cavity of figure 5 due to Wood's anomalies [41].

Classically, light is thought of as straight-traveling particles, but when it passes close to a physical barrier its wave properties are more noticeable, as it tends to curve around that barrier and spread out [42]. "The definition of diffraction is the scattering of waves as they pass through or around an obstacle" [43]. This effect happens when a light wave reflects or passes around a groove at an interface between materials of different refractive indices or through a slit with an approximate size or smaller than λ .

³also called diffraction grating



(a) Experiment schematic, first conducted by Augustin Fresnel (19th-century)

(b) Diffracted light intensity on transmission screen

Figure 7: Single-slit optical diffraction experiment. Retrieved from [43].

As shown in figure 7(a), a coherent light beam⁴ emitted from point source S will have consistent maxima and minima in space. After passing through the slit, light propagates radially into a screen, showing then the multiple diffracted orders with consequent decreasing intensities. As noticed in figure 7(b), the diffraction orders are periodically spaced by $\sin(\theta)$, with θ being the angle between normal incidence and the first diffraction minimum. Furthermore, when λ is much smaller than the aperture width d , the wave simply travels onward in a straight line, just as it would if no slit existed:

$$\sin(\theta) = \frac{\lambda}{d} \quad (1.2)$$

A diffraction grating is a multi-slit surface. The reflected/transmitted light wavefronts constructively interfere to produce a diffraction pattern with intensities peaked in certain directions, depending on both d^5 and λ and based on the angle light is focused into the grating [44]:

$$m\lambda = d(\sin(\theta_i) + \sin(\theta_d)) \quad (1.3)$$

where θ_i is the incident light's angle with the grating surface normal, θ_d the diffracted light's angle with the grating surface normal, and $m \in \mathbb{Z}$ being the number of the diffraction order. The signal convention associated with the grating theory is represented in figure 8. Macroscopically when diffracting white light, this phenomenon appears as a periodic repetition of the scatter effect of light.

⁴with all photons with identical frequency and waveform

⁵also referred to as Λ

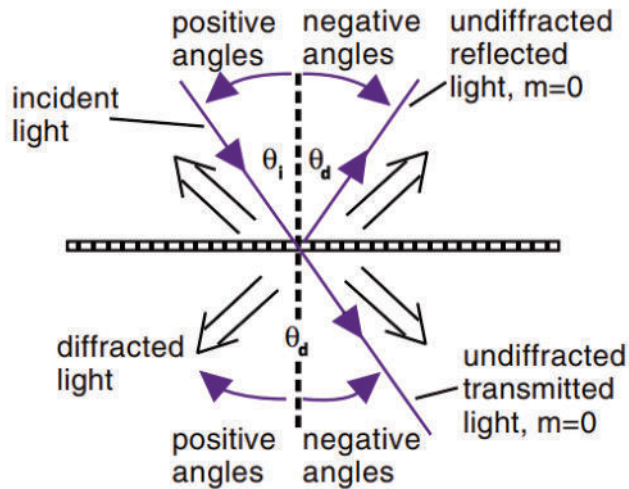


Figure 8: Optical diffraction grating signal convention. Adapted from [45].

When light is focused into the grating on normal incidence $\theta_i = 0^\circ$, thus $\sin(\theta_i) = 0$, which gives:

$$m\lambda = d \sin(\theta_d) \quad (1.4)$$

Wood's anomalies are observed in the light spectrum and resolved by optical diffraction gratings. "They manifest themselves as rapid variations [...] in the intensity of the various diffracted spectral orders in certain narrow frequency bands". This phenomenon was termed 'anomalies' by *R. W. Wood* (1902) since ordinary grating theory could not explain its appearance. Ordinary grating theory shows that incident light diffracted depending on the angle of incidence and on its features' dimensions, as shown in equation (1.3). In reality, a part of incident photons with $\lambda \approx \Lambda$ couples to the nanostructure. The coupled photons propagate and leave the nanostructure through other points. These photons promote variations in the intensity of the diffracted light measured at those points [46]. With this, it is possible to couple exiting photons with a 2DM above the grating, further increasing the region over which light interacts with it.

1.2.4 Reconfigurable and Programmable Nanostructures

The need for the fabrication of diffraction gratings capable of reproducing optical phenomena such as Wood's anomalies without excessive optical losses has become a challenge. Furthermore, it is essential to keep the possibility of controlling and setting up the period of these structures. This control over periodic features at the nano and micrometer scales is required in most research areas, but reconfigurable surface structures require complex lithographic processes with several masking and etching steps.

However, mechanical instabilities resulting from compressing a pre-stretched thin, rigid material film — often referred to as skin layer, over an elastomer-based substrate, a new, more straightforward way of creating variable scale surfaces with periodic corrugations has been discovered [47]. Growth-induced surface instabilities are very common in nature (e.g., pumpkin skin, cerebral cortex), making their replication a bioinspired process.

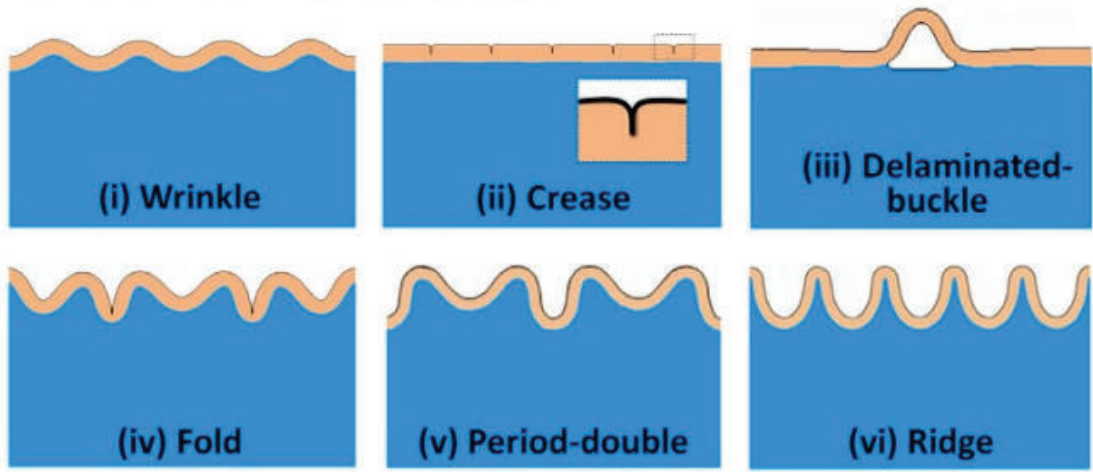
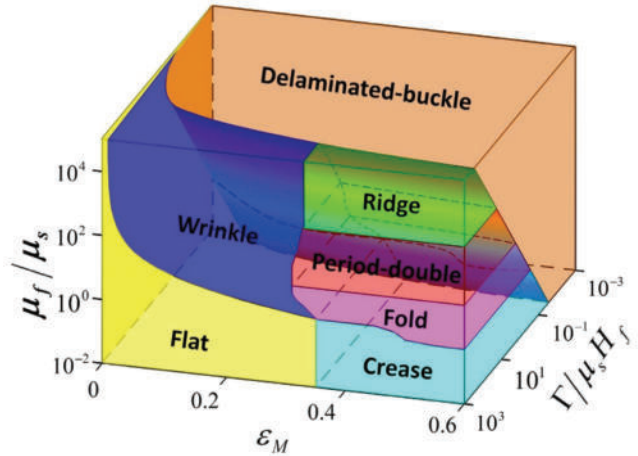


Figure 9: Cross-section schematics of growth-induced surface instabilities: **(i)** Wrinkle, **(ii)** Crease, **(iii)** Delaminated-buckle, **(iv)** Fold, **(v)** Period-double and **(vi)** Ridge. Adapted from [48].

The appearance of the specific structures from figure 9 through an exclusive dependence on the variation in the relationship between the materials' Young's modulus μ_f/μ_s is noticed for $\epsilon_M \geq 0.35$ (see equation (2.1)). The decreasing of this value below $\epsilon_M = 0.30$ promotes the appearance of periodic wrinkles logarithmic-dependant on that same relationship (figure 10). Furthermore, the normalized adhesion energy $\Gamma/(\mu_s H_f)$ of the interface between materials also plays a crucial role in creating these structures [48].

Figure 10: Theoretical 3D phase diagram of the various surface instability patterns induced by mismatch strains. Adapted from [48].



Sinusoidal wrinkled surfaces are found many times in nature, e.g., in the leaves of plants from the genus *Diplazium*, as shown in figure 1, or in angiosperms as floral grating-like structures for strong optical diffractive effects to enhance signaling to bees [49]. Both wavelength and amplitude can be designed based on the materials properties of the system and applied strain, where

$$\Lambda \sim 2\pi h \left(\frac{\mu_f}{3\mu_s} \right)^{1/3} \quad (1.5)$$

$$A \sim \frac{\Lambda}{\pi\sqrt{\epsilon_M}} \quad (1.6)$$

with h being the skin layer thickness, and μ_f and μ_s the Young's modulus of the skin layer and substrate respectively. *Nanowrinkles* behave as diffraction gratings and have the same optical mode of a resonator cavity as the one shown earlier (figure 5).

Fissures' appearance in the skin layer can be suppressed using softer polymer-based materials. Moreover, these structures can be mechanically oriented after being manufactured at room temperature. This adjustment consists in repeating the stretching process to force the texture to flatten and then stretch in another direction [47].

1.2.5 Large-Area 2D Material Transfer

Transferring large areas of a 2DM must be a surgical procedure, especially onto soft and non-flat target substrates such as periodic *nanowrinkles*. When synthesized by Chemical Vapor Deposition (CVD) on donor substrates these materials are prone to damage during the transfer process to a target sample with such dimensions. Material damage can be of various types, such as contamination, chemical doping, or tearing. All transfer processes are categorized into four main groups: wet, dry, mechanical, and electrochemical transfers, as summarized by table 2).

Wet transfers are assisted by a poly(methyl methacrylate) (PMMA) support thin film – also known as acrylic. This thin film is spin-coated on top of the 2DM protecting it from mechanical damage or abrasion. The transfer method consists in scooping these sets of thin layers onto a stiff flat material, later dipping it into another solution, and passing them from one container to another. After removing the donor substrate, the PMMA/2DM floats in deionized water for rinsing residual etchant, later being scooped by a target substrate. Then, the PMMA/2DM/target substrate is dipped in a solvent for removing the PMMA. Wet transfers are the most common since they offer the highest protection against mechanical damage and cover a wide range of different 2DMs.

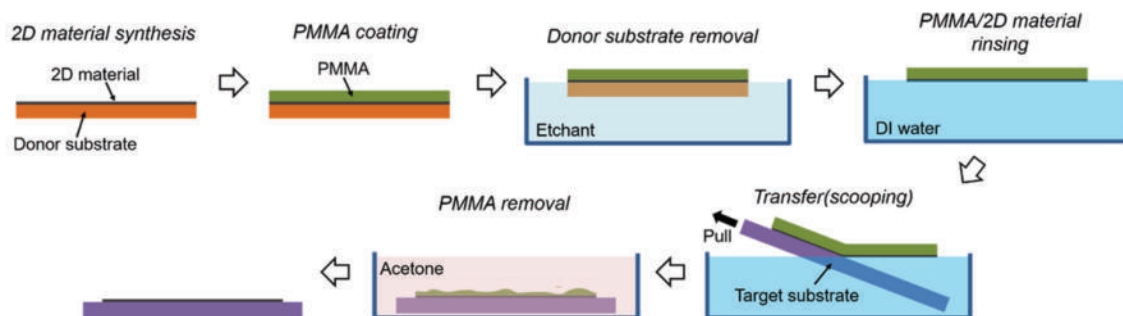


Figure 11: Schematic of conventional wet transfer process of 2DM using a PMMA support film. Retrieved from [50].

Dry transfers are based on the adhesion between the 2DM, a compliant layer, and the target substrate. These adhesions are a consequence of Van der Waals forces between materials. To simplify, 2DM is pressed onto a compliant layer coated on top of a supporting film. Then, the donor substrate should be etched and rinsed in deionized water. The adhesion between the compliant layer and the 2DM should be lower than the one between the target substrate and the latter. Pressing the supporting film/2DM into the target sample and peeling it off will leave the 2DM on top of the desired sample. This process is suited for large-scale transfers and offers the least polymer residue soiling. However, the 2DM is more prone to damage with this transfer method than the wet.

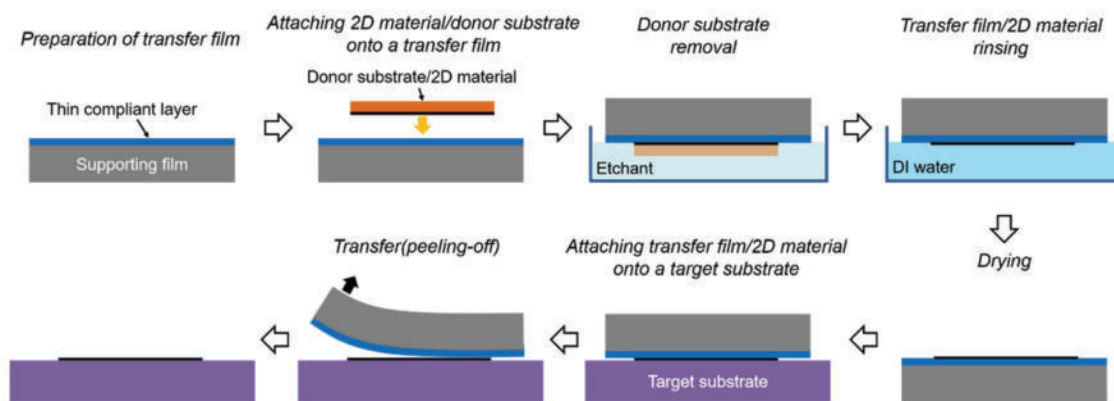


Figure 12: Schematic of the conventional dry transfer process of 2DM using a compliant layer coated onto a supporting film. Retrieved from [50].

Mechanical transfers work with active thermoplastic or thermosetting adhesive materials. Thermoplastics are coated onto the target sample and contact with the 2DM on the donor substrate at high temperature and pressure, later the target/adhesive/2DM is peeled-off from the donor substrate at room temperature. Thermosetting materials are coated onto the target sample and pressed into the 2DM on a donor substrate in a viscous state and thermally cured to firmly adhere to the 2DM. Then, the target/cured adhesive/2DM is delaminated from the donor substrate. Mechanical transfers have the limitation of depending on the target sample shape.

The electrochemical transfer process – also known as the bubbling transfer process, is very similar to the wet transfer. The significant difference is that the 2DM is delaminated from the donor substrate using hydrogen bubbles generated at its interface by a reduction reaction of an aqueous solution according to the voltage applied between an anode and the donor substrate (cathode). After this, the PMMA/2DM layer emerges in the aqueous solution, later being scooped in the same way that wet transfers. Electrochemical transfers are known for being the quickest, allowing the recycling of the donor substrate. However, during this transfer the 2DM have the most risk of mechanical damaging [50].

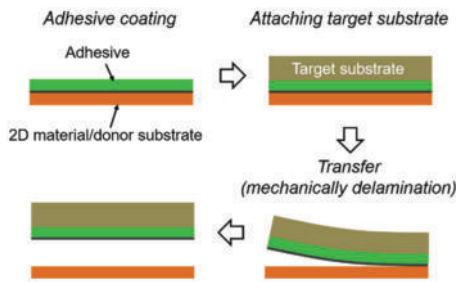


Figure 13: Schematic of the mechanical transfer process using an adhesive. Retrieved from [50].

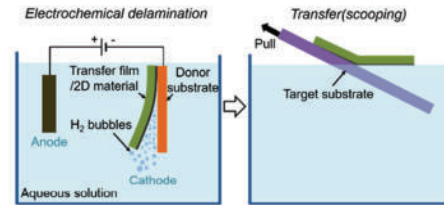


Figure 14: Schematic of the electrochemical transfer process with H_2 bubbles. Retrieved from [50].

Table 2: Representative transfer methods for 2DMs. Adapted from [50].

Method	Material	Advantages	Limitations
Wet Transfer	<i>Graphene</i>	Least mechanical damage	Difficult to scale up
	<i>MoS₂</i>	Wafer-size transfer	Support polymer residue
Dry Transfer	<i>Graphene</i>	Easy to scale up	Mechanical damage
	<i>MoS₂</i>	Less polymer residue	(more than wet transfer)
Mechanical Transfer	<i>Graphene</i>	Easy to scale up	Mechanical damages
	<i>MoS₂</i>	Recycle of donor substrate	Difficult to remove adhesive Dependant on sample shape
Electrochemical Transfer	<i>Graphene</i>	Recycle of donor substrate	Can't scale up
		Quicker method	Mechanical damage (more than dry transfer)
			Support polymer residues

Of all discussed processes, the most suitable to be used with the nanostructure fabrication technique mentioned in section 1.2.4 appears to be the wet transfer method. This is because it provides the lowest risk of mechanical damage to the 2DM at the expense of a smaller area.

1.3 Measurement Methods

Morphological analysis and optical characterization are critical steps to determine whether or not the state of the nanostructure will influence the light-matter interaction with the 2DM. Following are all the measurement methods and setups used during this dissertation, with a brief theoretical introduction.

1.3.1 Atomic Force Microscopy

Atomic Force Microscopy (AFM) is used to analyze the topography of samples at the micro and nanoscale. The interaction between two materials at the atomic level is based on forces such as Van der Waals, electrostatic, and magnetic, among others. When one of these materials is drawn in the form of a tip, with a radius in the order of magnitude of an atom, fixed in a cantilever, it will deviate depending on the attraction or repulsion between the tip and the sample. Traditionally, most AFM techniques use the deflection of a LASER beam reflected in the rear of the cantilever over a matrix of photodetectors to calculate the topography of the sample [51].

The equipment used was the *BRUKER Dimension Icon AFM on Tapping mode*, where “the sharp probe tip is not scanned across the sample surface while in constant contact. Instead, the cantilever is vibrated near its resonance frequency causing the tip to oscillate up and down. This means the probe only comes into close contact with the surface intermittently”, using the cantilever oscillation amplitude to detect tip-sample interaction changes [52]. All measurements are processed with the data visualization and analysis software *Gwyddion*.

1.3.2 Fourier Imaging Setup

The full Fourier setup used is shown in figure 15. The entire setup was designed to operate in the VIS spectrum. The lenses' focal lengths are represented as arrow traces except for objective lenses, as they are not considered thin lenses. The process starts by coupling light from a halogen lamp to a variable diameter optical fiber: 25, 50, 105, or 400 μm . The fiber diameter will influence the size of the focused spot on the sample. For this application the chosen size was 400 μm , covering as much area of the sample as possible, improving the grating diffraction effect. An objective lens is used to collimate light which is headed into the microscope cage – a *Nikon Eclipse Ti2*. In figure 15 the scheme is simplified, since the light operates in the normal direction, creating a 3D system. Through a 50/50 beam splitter, the light is normally focused into the sample and then headed into two irises. The first regulates real image size and the second acts as a low-pass filter in the real space, thus having the same purpose as the first, but in Fourier space. The polarizer is used to select the polarization of transmitted light. Through two more beam splitters, light is directed to four different detectors: three charge-coupled device (CCD) cameras (A, B, and C), a CCD camera (C) on a spectrograph inside a black box, and a spectrometer. Cameras A and B capture the image on the real and Fourier space respectively.

L_6 is used to translate the real plane to a $2f$ distance away to reach either one of the two last sensors mentioned. With the flip mirror on, light is focused onto an optical fiber connected to the spectrometer. Lowering the flip mirror, light is headed to the spectrograph, and thus to CCD camera (C), providing a 2D array of sensors for wavelength reflection measurements with angular resolution. The spectrograph used is the *Acton SpectraPro SP-1250*, the fiber-coupled spectrometer is the *USB2000+ Spectrometer*, and the CCD camera (C) is a *QImaging Retiga R6 USB3.0 Colour*.

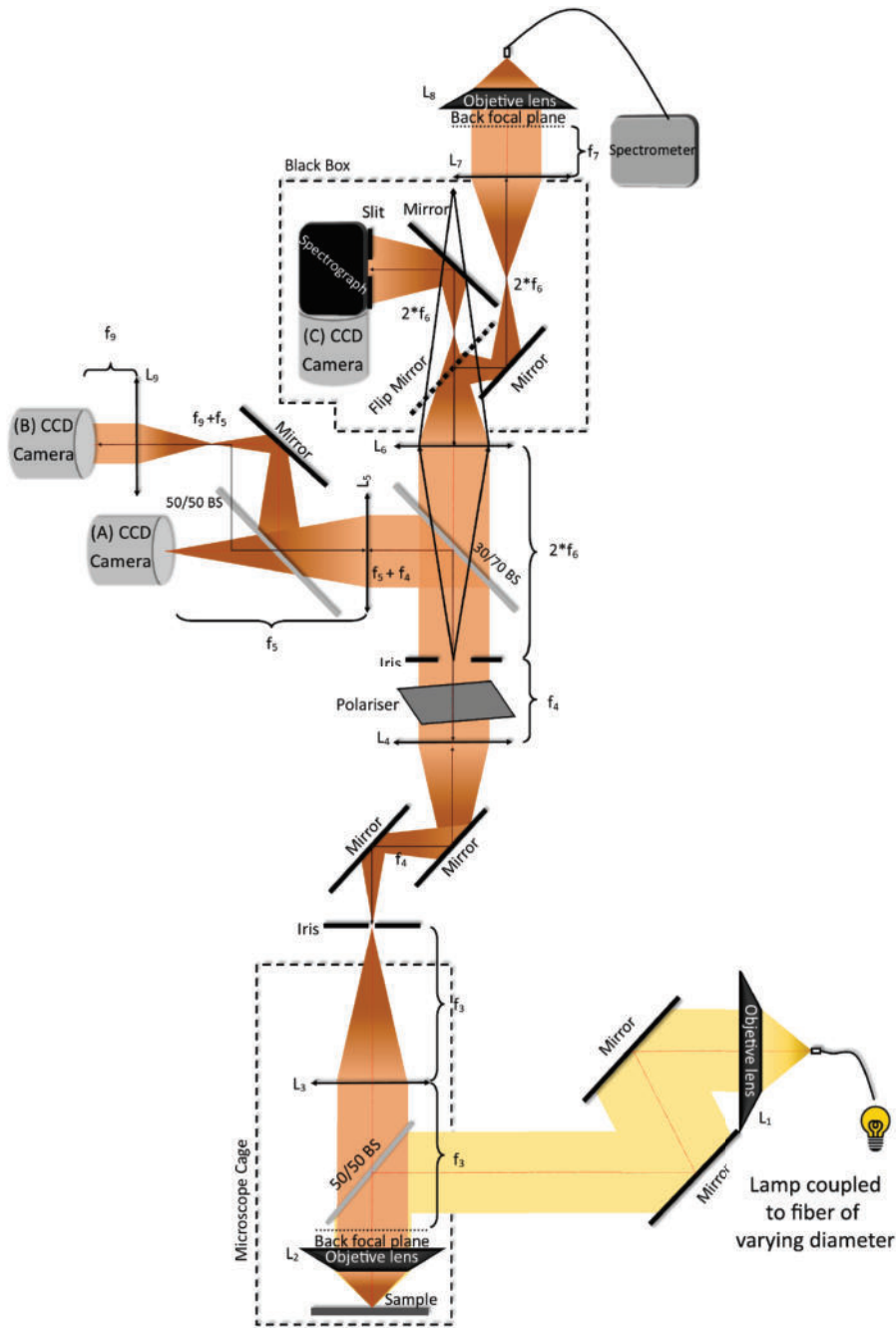


Figure 15: Schematic of the full Fourier microscope setup used throughout the dissertation.

1.3.2.1 Angular Reflection Spectrophotometry

Angular spectrophotometry is the selected experimental technique for optical diffraction grating testing. It consists of focusing a light beam on a sample's surface and sensing the angle and wavelength-dependent intensity of reflected light.

This measurement technique is only able to capture a wavelength range of $\sim 35 \text{ nm}$ at a time. For wide-range measurements, a *MATLAB* script was used to couple the data from each of the intervals. Note that the reflection measured (r_{sample}) on the sensor must be normalized by one reference (r_{ref}) to obtain

sample reflectance (R). As a reference, a silver mirror was used due to its unmatched reflective properties in VIS spectrum [53]. In addition, it is necessary to consider the measurement noise (δ), which is taken with the spectrograph's slit closed. Consequently, three measurements are required to obtain the result:

$$R = \frac{r_{sample} - \delta}{r_{ref} - \delta} \quad (1.7)$$

The measurement exposure time must be maximized to the point where the reference begins to saturate.

1.3.2.2 Reflection Microspectrometry

Microspectrometry eliminates from captured light any angular information but allows quick measurements with good resolution. A different configuration can also be used from the Fourier setup of figure 15, where the fiber connecting to the spectrometer is moved to L_7 's location to measure only the normal reflection. The optical fiber used has a diameter of $200 \mu m$, narrow enough for quasi-normal reflection measurements.

1.3.3 Optical Microscopy

Optical microscopy consists in focusing light onto a sample that, after being reflected or transmitted, penetrates a lens system, magnifying the image up to $200\times$ over the user's retina or on a CCD camera [54]. The equipment used was the optical microscope *Nikon ECLIPSE LV100*.

To measure Δ , the procedure developed in this dissertation consists in capturing an optical image at four distinct spots of each of the samples. Each image is processed by *ImageJ*, applying a **Fast Fourier Transform**. In textured images, the periodicity of the pattern is easily identifiable in Fourier space. Considering 60 nm/pixel as the obtained scale for the $40\times$ lens for the setup used and mentioned in 1.3.2.1, the points of greatest intensity in the Fourier space give the average period of the entire cropped section of the captured image.

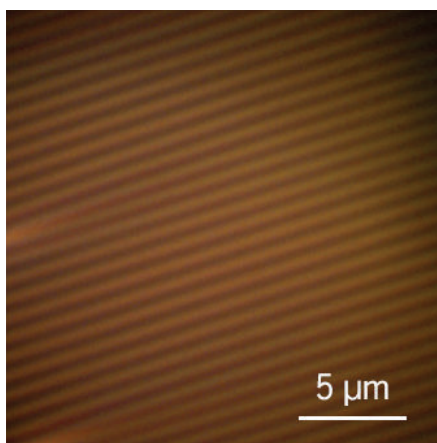


Figure 16: Cropped section from WD10.1 Spot1. See appendix B.2.

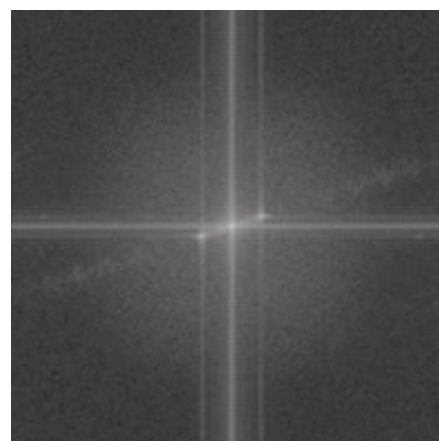


Figure 17: **Fast Fourier Transform** of figure 16. Pixel intensity as a function of frequency.

1.3.4 Raman's Spectroscopy

Raman's spectroscopy allows composition analysis in a non-destructive way, providing detailed information about the chemical structure, crystallinity, and molecular interactions with other materials. The incident light interacts with molecular vibrations, phonons, and other excitations from the system, dispersing elastic – Rayleigh's scattering, which is filtered by the spectroscopy system; and inelastic – Raman's scattering. This scattering changes the energy of the scattered photons [55]. This change, calculated in intensity related to the incident photon, is measured as light scattering in the diffraction grating where the confocal beam is focused after the sample reflection. This characterizes the system in terms of its vibrational modes [56]. By comparing the spectrum obtained with references, it is possible to determine the purity of the material, which will influence properties such as electronic or mechanical.

The equipment used was the *WITEC alpha300 R Confocal*, with an excitation line of 532 nm, at 1.5 mW of power, with a diffraction grating of 600 cm⁻¹.

1.3.5 Scanning Electron Microscopy

Scanning Electron Microscopy (SEM) is a non-invasive method of topographic and composition analysis, depending on the generated signal observed. SEM is capable of producing images with magnifications up to 200 000× by scanning a focused electron beam on a sample [57]. Incident electrons interact with sample atoms and various signals are produced, including secondary electrons, generated because of their ionization. These electrons have very low energies, limiting their average free path in solid matter. By this fact, they dissipate in the first nanometers above the sample's surface, being exclusively located at the focus spot of the e-beam, enabling images with resolutions below 1 nm [58].

The energy with which the e-beam is accelerated influences the amount and type of signal created. For topographic applications, low-voltage, with a working potential up to 4 kV, is the ideal mode, allowing greater surface detail at the expense of greater noise in the image obtained [59]. Samples made of dielectric materials accumulate charge when scanned by the e-beam, which can cause high noise and image processing failures. To avoid this, all samples are covered by 10 nm of gold, and electrically grounded with copper tape [60].

The equipment used was the *FEI Helios NanoLab 450S DualBeam*, in SEM - Secondary Electrons mode.

Photonic Nanostructure Fabrication

First step for the final device. Fabrication of the three-dimensional structure that will hold the two-dimensional material and behave with the desired photonic properties.

As mentioned in section 1.1.3, the device behind the whole project should be a combination of a 3D structure with a 2DM interacting by any means with a specific light spectrum. In addition, the nanostructure holding the 2DM must have periodic features in the order of magnitude of the light's wavelength and be transparent.

This chapter describes the fabrication process of the 3D structures that originate photonic properties on the final device, serving as a workstation for the 2DM.

2.1 Design

The main motivation of the device is to work within the solar spectrum. Sunlight, despite being filtered by successive layers of Earth's atmosphere, reaches the planet's surface at sea level with a wavelength between 300 and 2500 nm, with a maximum spectral irradiance of $1.3 \text{ W m}^{-2} \text{ nm}^{-1}$ at 468 nm, which corresponds to the central wavelength of blue-VIS light [61]. As evidenced by figure 18, from all this energy coming from sunlight that reaches our eyes, 91.7% refers to the range between violet-VIS (380 nm) and NIR (2500 nm) [62].

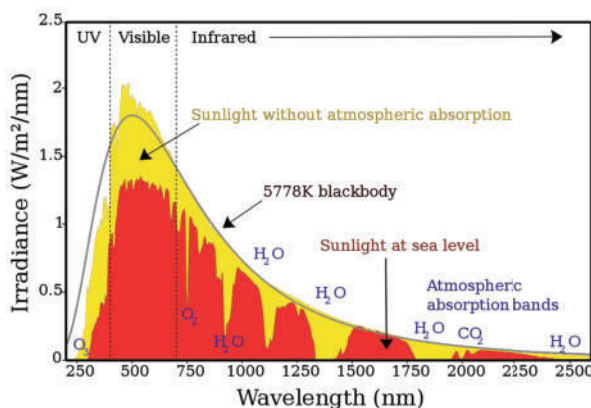


Figure 18: Solar irradiance spectrum above Earth's atmosphere and at sea level. Retrieved from [61].

The fabrication process must cause a texturing in the nanostructure with a constant period, with the order of magnitude within the typical spectrum of the incident light, therefore with periods of 380 to 2500 nm , as stated in 1.2.3.

The texturing of the substrate and skin layer, as described in 1.2.3, will be the cause of the light diffraction effect on the device, therefore improving the light-material interaction in the adjacent 2DM, e.g., via the excitation from Wood's anomalies. In other words, the 3D structure must behave as a diffraction grating. In addition to the structure's periodicity, its morphology is crucial to proper functioning. Characteristics such as the wavelength range affected, as well as its efficiency by diffraction order, i.e., the percentage of scattered photons within the typical wavelength range by the total incident, are properties defined by the periodic features shape [63]. These shapes can be of continuous morphologies such as sinusoidal, or discontinuous such as binary, sawtooth, or triangular.

Diffraction gratings with discontinuous morphologies provide maximum efficiencies above 80%, at the expense of a reduction of more than half the wavelength range for efficiencies above 40% [64]. However, these gratings require complex photolithography processes for their fabrication, often only possible in controlled cleanroom environments [65].

Taking advantage of surface instabilities phenomena in bilayer architectures resulting from compressing forces reported in 1.2.4, it is possible to manufacture continuous morphology diffraction gratings in a simple, fast and accurate way, avoiding all the inconvenience of time-consuming processes in a clean room environment. From all the continuous morphologies mentioned, due to its simplicity sinusoidal design provides the best conditions for further morphological analysis and optical characterization. Furthermore, the sinusoidal design allows larger room for maneuvering on control parameters, as shown in figure 10.

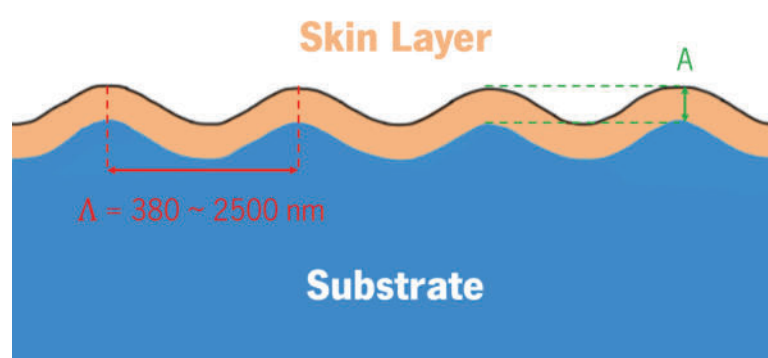


Figure 19: Cross-section sketch of the desired 3D nanostructure.

To sum up, the 3D nanostructure will have sinusoidal features¹ with Λ between 380 and 2500 nm , as can be seen in figure 19.

¹also referred to as *nanowrinkles*

2.1.1 Substrate Choice and Considerations

The substrate of the 3D structure is the device's bulk. One must be of an organic-based polymeric material. This material should be transparent, i.e., to have a low refractive index and despicable absorption in the operating spectrum. Plus, that material must have high elasticity, since it should resist high compressive or tensile strains. To finalize, its *Young's modulus* should be higher than the skin layer. The material chosen for the substrate was *poly(di-methylsiloxane)* (PDMS). In addition, this material shows high thermal and chemical stability, allowing the deposition of materials and surface treatments with too little structural damage [66].

PDMS is a polymer chain that belongs to the organosilicon group, traditionally called silicones. The monomer's molecular structure corresponds to a central silicon (Si) atom, strongly bound to another oxygen (O) with two weak bonds to two methyl groups (CH₃), as observed in figure 20.

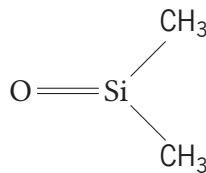


Figure 20: Chemical structure of di-methylsiloxane.

In its fundamental state, this material is known to be viscoelastic, that is, it flows between the state of a viscous liquid and an elastic solid depending on the temperature [67]. In addition, PDMS has a refractive index $n = 1.41$, close enough to air, which provides low reflectance in the VIS spectrum [68], and its surface is hydrophobic. Regarding health and safety hazards at work, PDMS does not provide any risk of inflammation or toxicity, thus having high chemical stability. Furthermore, this material offers weak intermolecular forces making it an elastomer, known to have reduced *Young's modulus*, and high shear stress.

PDMS is rarely used in its fundamental state and is usually subjected to cross-linking processes. Cross-linking is the addition of thermally activated resins that stiffen when absorbing heat. This addition strengthens the weak bonds between polymer chains of the material, making it more rigid and cohesive, but also improving its durability [69].

2.1.2 Skin Layer Definition and Tailoring

As shown in section 1.2.4, the skin layer is the rigid and thin layer on top of an elastic substrate that generates surface instabilities. Since the device operates with *optoelectronic* phenomena, this material, as in the case of the substrate, must be transparent in the region of interest, but also a good electrical insulator. In addition, as mentioned above, its *Young's modulus* should be substantially lower than PDMS's. The material chosen was the result of prolonged treatment of the PDMS's surface by oxygen plasma, which is one of the most common techniques to achieve surface instabilities with this type of polymer [47].

This material is not a simple compound, since it is the result of the chemical treatment of a polymer chain. Still, this closely resembles silicon dioxide due to the Si—O bonds formed on the surface. Oxygen plasma acts by oxidizing the methyl groups and removing carbon, chemically altering the di-methylsiloxane monomer ($\text{SiO}(\text{CH}_3)_2$) into silanol ($\text{SiO}(\text{OH})_2$) groups, leaving the polymer surface covered by hydroxyl (OH) groups, as observed in figure 21, providing an extremely hydrophilic state [70]. This reaction leaves the structure chemically unstable.

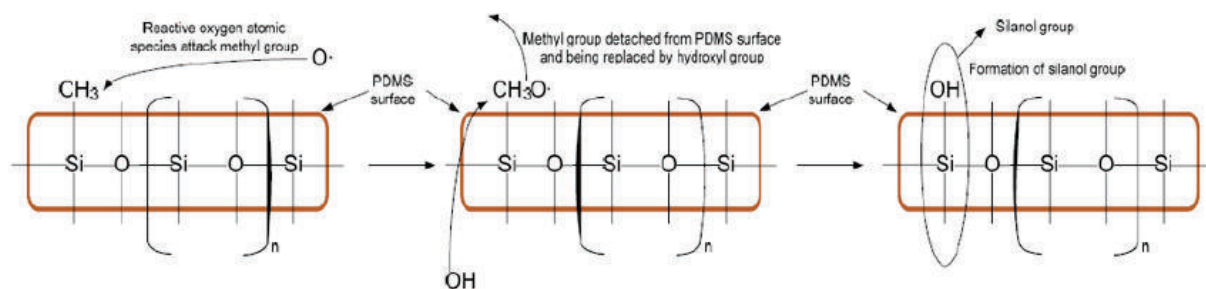


Figure 21: Effect of the oxygen plasma treatment on PDMS's surface. Retrieved from [71].

Since one of the main steps of the project is the transfer of materials onto the surface of the PDMS treated by oxygen plasma, it is worth understanding its chemical properties after the treatment. Skin layer aging triggers a reversible chemical reaction called *silanol condensation*, where unstable hydroxyl groups react with each other, condensing in the form of water molecules (H_2O), resulting in an inorganic silica-like surface (SiO_x), as evidenced by figure 22. The new surface is much more chemically stable [72]. As in every condensation process, this reaction is catalyzed by low-pressure environments [73].



Figure 22: Condensation (from left to right) and hydrolysis (from right to left) reactions of silanol groups.

According to the intensity and duration of the plasma, the treatment will act on deeper layers of the polymer, but due to hydrophilic hydroxyl, silanol groups will suffer consequent chemical migration to the material interface, accelerating the condensation reaction. This reaction directly influences the hydrophobicity of the skin layer's surface, which has a logarithmic evolution from the moment of plasma treatment with an inflection point close to 48 hours of exposure [74], as shown in figure 23. Surface hydrophobicity does not completely characterize the skin layer, since the chemical migration of silanol groups is not an immediate process.

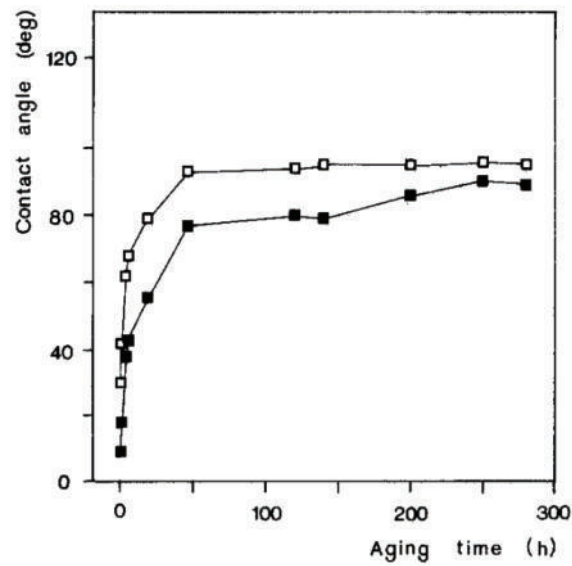


Figure 23: Advancing (■) and receding (□) water-in-air contact angles as a function of aging time at 293 K. Retrieved from [74].

Figure 24 represents the process discussed above. The chemical structure of PDMS treated by the oxygen plasma changes according to the samples' resting time.

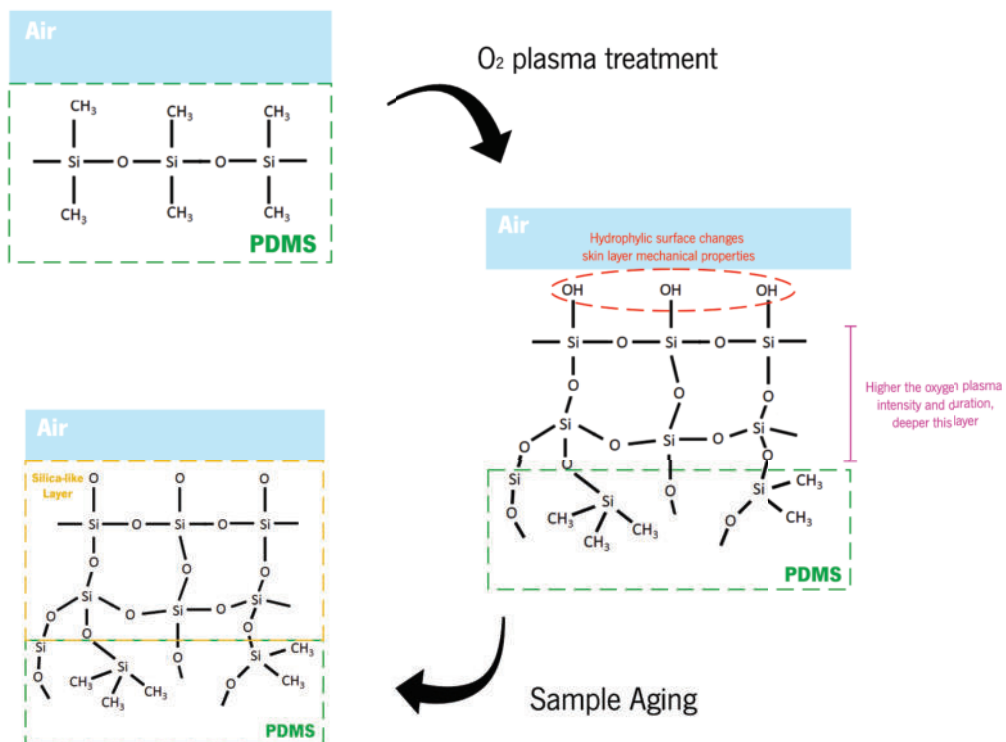


Figure 24: Chemical changes on PDMS's samples after oxygen plasma treatment and after resting time.

2.2 Conditions and Parameters

To avoid unnecessary propagation of experimental errors and keep accurate results it is necessary keeping constant manufacturing conditions. These conditions directly influence the parameters represented generically in equations (1.5) and (1.6), which characterize the nanostructure's morphology, as discussed in section 1.2.1.

The skin layer's thickness h is the most easily controllable parameter, depending exclusively on the plasma treatment chamber conditions, including oxygen pressure, the number of purge cycles, plasma exposure time, and, in some cases, samples' position inside the chamber. Since measuring the thickness of the skin layer after plasma treatment is an impractical task and often produces inaccurate results, the best strategy is to keep all conditions constant and adjust only the exposure time if needed.

The Young's modulus of the skin layer is affected by the chemistry associated with the oxygen plasma treatment as described in 2.1.2. In the case of the substrate the cross-linking ratio is the main element to affect this property (see section 2.1.1). Particularly, the most usual cross-linking is made by a mixing ratio between the elastomer base and the curing agent of 10:1 (M), offering stiffness but maintaining enough elasticity for ϵ_M up to 40% [75]. These parameters are tuneable through the choice of materials used in the manufacturing process.

As for ϵ_M it was used 20%, matching the point that generates wrinkles with maximum amplitude without the appearance of fissures in the skin layer that could jeopardize the final device [47]. This is another parameter not easily controllable considering the method used in 2.3. In addition, this parameter would only influence A , which plays a role in the maximum efficiency of the diffraction grating, but not in its wavelength range. For the latter, the main responsible is Λ .

2.3 Fabrication Method

Following is a list of the material and equipment used for the method discussed in this section:

- SYLGARD™ 184 Silicone Elastomer Kit (Base + Curing Agent);
- 1 *cm* conventional² binder paper clamps;
- 12 *cm*² plastic Petri box;
- 7.5 × 2.5 *mm* glass slides.
- HARRICK PLASMA™ High Power Plasma Cleaner.

A portion of elastomer base and curing agent was poured into a goblet in the ratio of 10:1 (M). The mixture was stirred with a glass rod for about 5 minutes. The mixture was then taken to the desiccator, making

²metallic

purge cycles in order to remove air bubbles. It was dosed with 18 *mL* of mixture per Petri box so that the substrate remained with a fixed thickness. The mixture was carefully deposited onto the box's center, leaving it to level on a flat surface. Subsequently, the boxes were taken to the oven 65 °C for 2 hours, thus cross-linking the PDMS.

The next step was to cut the substrate inside each box in such a way that, using the length of the glass slide as a guide, the pre-strain corresponds to the desired value, as shown in figure 25. Note that the end of the substrate fastened by the first clamp should not be considered. Therefore, the percentage of pre-stretch is given by:

$$\epsilon_M = \frac{L'_f - L'_i}{L'_i} \Rightarrow L_s = \frac{L'_f + \epsilon_M \times c}{1 + \epsilon_M} \quad (2.1)$$

where $L_i = L'_i + c$ corresponds to the initial length of the substrate and $L_f = L'_f + c$ to the final one, with L'_f being the length of the glass blade and the c length of the first spring.

Assuming $L'_f = 7.5$ *cm*, $c = 1$ *cm* and $\epsilon_M = 0.2$, this gives $L_s \approx 6.4$ *cm*. Cutting the substrate with the glass slide width for easy stretching, the substrate strips will have the dimensions of 6.4×2.5 *cm*.

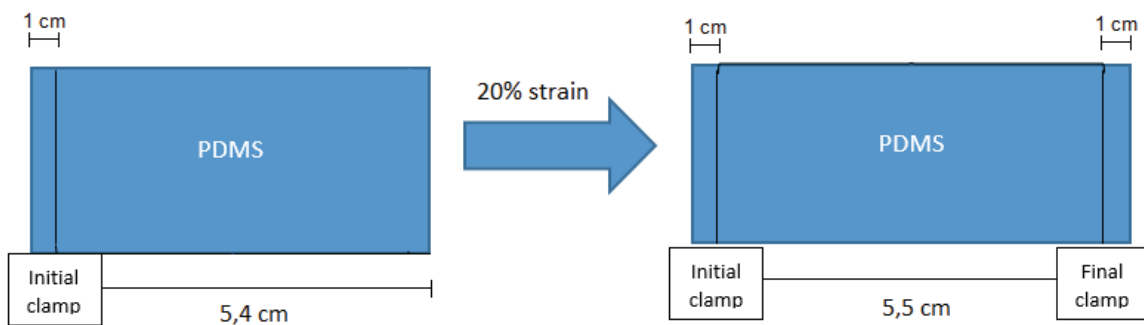


Figure 25: Substrate stretching diagram of the method used in section 2.3.

The substrate strip is placed on one end of the glass slide and fastened by a clamp. Then the strip is stretched to the full length of the slide and fastened immediately by the second clamp. The batch is then inserted into the plasma treatment chamber in oxygen mode.

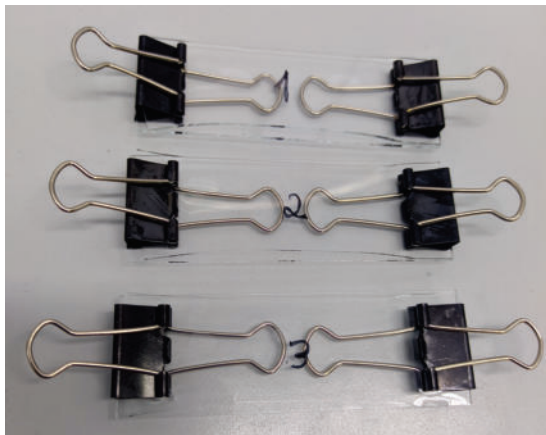


Figure 26: Batch of 3 samples with fastened clamps on both sides after PDMS pre-stretching. Each glass slide was numbered from 1 to 3, meaning the placing position inside the oxygen plasma chamber according to figure 28.

The oxygen plasma treatment conditions should be kept constant. These conditions are the injected oxygen pressure: $P_{O_2} = 5 \Psi$; the number of purge cycles: 3 oxygen cycles; the intensity of the RF signal: HIGH; and the plasma up-time: 20 minutes. The choice of these parameters was made during the calibration of the camera which can be consulted in figure 83. Batches of 3 sample types each are manufactured. Plasma treatment is carried out simultaneously in the 3 samples, which are inserted into the vacuum chamber in the same way as shown in figure 28.

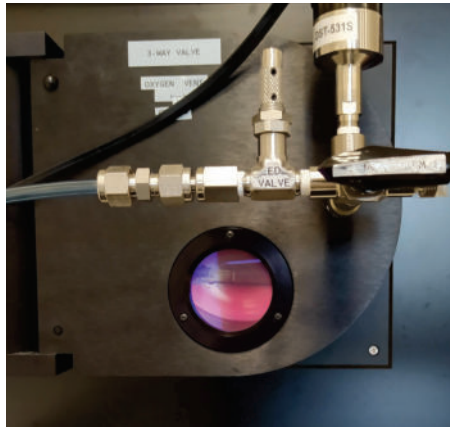


Figure 27: HARRICK PLASMA™ high power plasma cleaner used in this section's fabrication method. The red color is a plasma of atmospheric air.

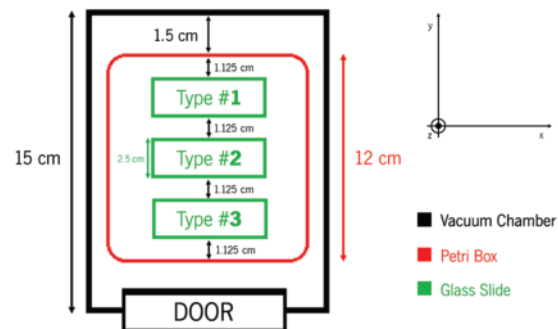


Figure 28: Aerial view of the plasma cleaner chamber of figure 27 and sample type placement diagram. These types will be used throughout this project.

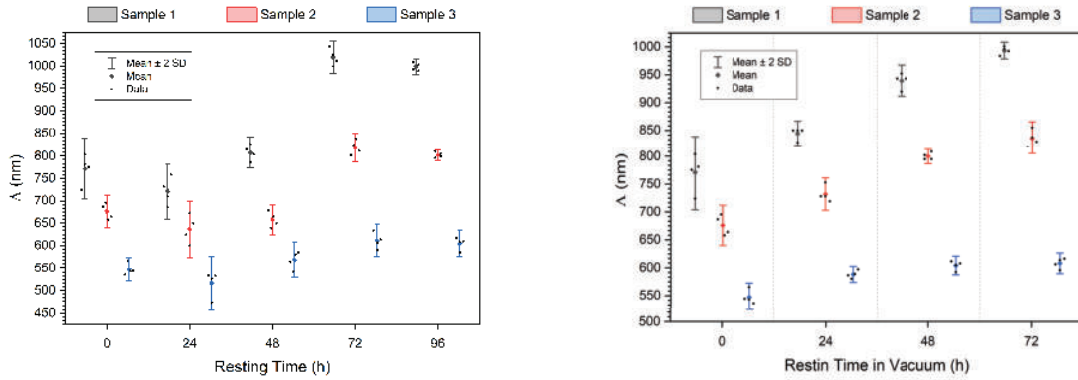
After treatment, the batch is left at rest in low vacuum for 72 hours, following the removal of the second clamp fastened and gently retracting the substrate. The samples are cut at the edges where stretch forces do not exist or are not well distributed. The resting time was selected after the analysis carried out in section 2.3.1. Procedure and material pictures can be viewed in appendix A.1.

2.3.1 Calibration of Conditions

As in any process where reproducibility is desirable, the calibration of its respective conditions and parameters is necessary. The sample fabrication should consider the skin layer's aging process discussed in section 2.1.2 since it influences the result of the wrinkles created. The stabilization of Δ is important in reducing the disparity between measured points, as it's noticeable in 29(a) for higher resting times the lower the standard deviation.

Batches of samples fabricated by the method described in section 2.3 were measured with the statistical procedure mentioned in 1.3.3, varying the resting time after plasma treatment, as well as their pressure environment before the substrate unstretching. Resting in low-pressure environments (figure 29(b)) behaved as a catalyst for the condensation reaction mentioned in 2.1.2, reducing the time required for that. These results are consistent with the data shown in figure 23, as the surface's hydrophobicity

increases and stabilizes over time. Experimentally, as shown in 29(a) the inflection point of the chemical composition of the surface is perceptible after 72 hours. The vacuum is set to overextend this effect.



(a) Λ depending on samples' resting time

(b) Λ depending on samples' resting time in vacuum

Figure 29: Statistical analysis of fabrication method mentioned in section 2.3 with varying resting time after oxygen plasma treatment. Samples 1, 2, and 3 correspond to the different sample position types as shown in figure 28.

As shown in figure 29, consistency can be achieved for each sample position inside the chamber using consistent fabrication parameters. $\Lambda \approx 1000, 800$ and 600 nm for type #1, #2, and #3 were obtained respectively for the fabrication method mentioned in 2.3, with relative standard deviation of measured spots $\%_{\sigma}$ of 1.57%, 1.62%, and 2.54% respectively, as shown in appendix B.3. The general outcome was a lack of overall strength in the oxygen plasma. This is because the plasma chamber used does not have the finesse required for thin film growth processes, as it is used for the preparation of hydrophobic surfaces in polymeric materials.

Moreover, the oxygen plasma intensity distribution within the chamber was not uniform, with a vertical gradient (y -direction) with decreasing intensities for positions further to the chamber door. This is expected to produce a variation in the periodicity obtained as shown in figure 30 between sample types #1, #2, and #3. Despite this variation, it is possible to obtain consistent results by selecting the same position within the chamber systematically and varying the time of exposure, keeping the uniformity of the silica-like thickness constant from sample to sample.

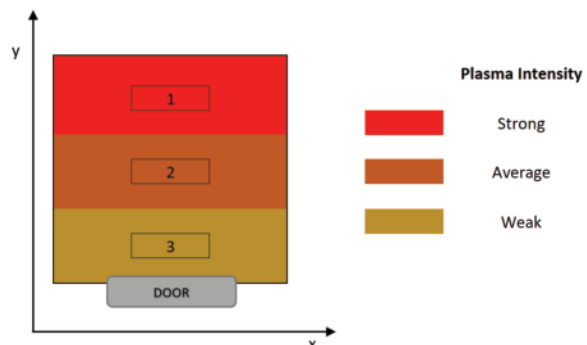


Figure 30: Prediction of oxygen plasma intensity distribution inside the vacuum chamber. Rectangles are the three sample types of one batch properly numbered.

It's also predictable the existence of a calibration curve for this fabrication method. Since the continuous relation between the exposure time and the wrinkles period is not necessary for the current project, it is possible to work only within a limited range of values, so the exposure time was kept at 20 minutes, thus obtaining the three distinct Λ mentioned above.

2.4 Morphological Analysis

As discussed, the 3D nanostructure features' dimensions and shape will influence the diffraction grating's performance. Morphological analysis is a crucial step in establishing the sample manufacturing process, allowing to check the state of the features and, therefore, calibrating the fabrication conditions.

Following are optical microscope images of samples manufactured by the method described in section 2.3.

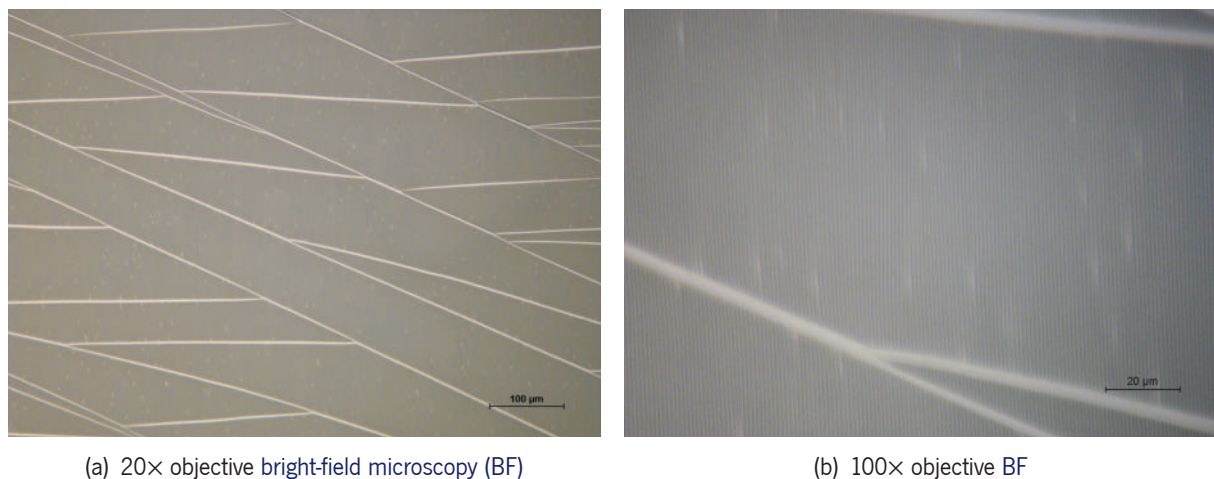


Figure 31: Optical microscope images of a type #1 sample (larger Λ).

The oblique and perpendicular stripes to the *nanowrinkles'* orientation are fissures³ in the skin layer. They are substrate stretching-direction oriented due to the high shear stress created during the clamp release due to forces applied in other directions than the unstretching movement. Crack appearance is more frequent on skin layers with brittle materials such as silica, as mentioned in section 1.2.4. For objective magnifications of 20 \times (figures 31(a), 84(a), and 85(a)), larger Λ were barely visible. For 100 \times magnifications (figures 31(b), 84(b), and 85(b)) all samples had visible *nanowrinkles*.

The Raman spectrum from a flat PDMS sample was compared with one treated with oxygen plasma with the conditions mentioned in 2.3 to investigate the influence of each of the fabrication steps on the chemical composition of the material. All measurements obtained are present in appendix C.3.

³also called cracks

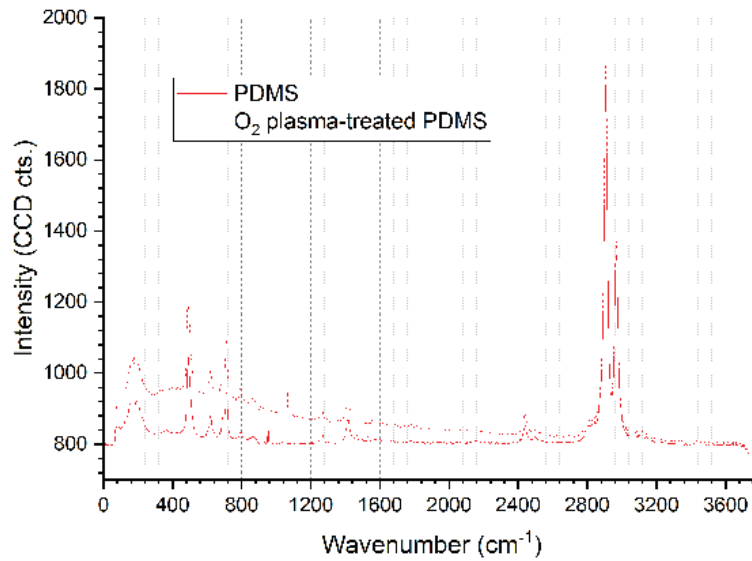


Figure 32: Raman spectra of oxygen plasma-treated and untreated PDMS. The integration time used was 2 s, with 10 acquisitions.

In figure 32 is noticed that all Raman peaks from untreated PDMS match the theoretical spectrum of figure 102. Moreover, all peaks have the same intensity and wavenumber as in treated samples, showing a slight broadband increase in intensity with a maximum value near 400 cm^{-1} , corresponding to the addition of a low-intensity silica Raman spectrum to the plot. Fused silica's Raman reference spectrum is shown in figure 104.

Two batches of samples manufactured by the method described in 2.3 were measured at the AFM to understand the state of the periodic features of the nanostructures in terms of their amplitude and periodicity. All obtained results are present in appendix C.2.

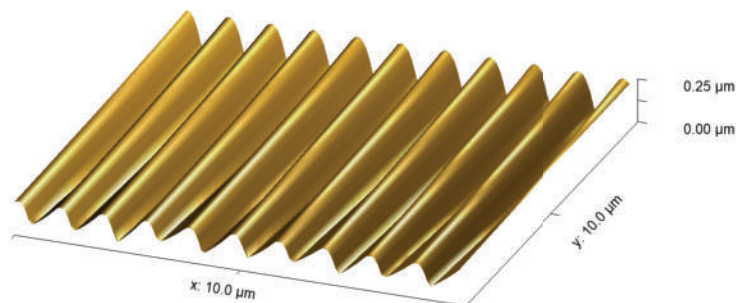


Figure 33: AFM-measured 3D representation of a type #2 sample.

As shown in figure 33, AFM allows the visualization of 3D features with a high level of detail in an orthographic projection.

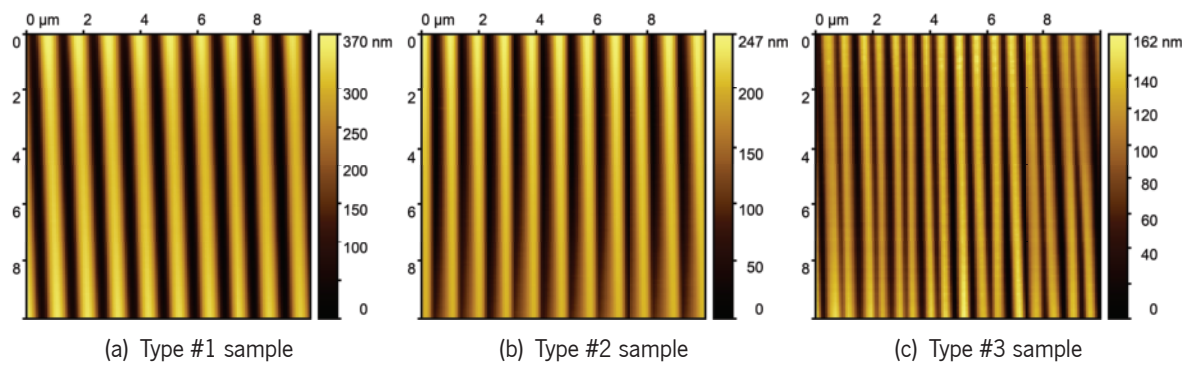


Figure 34: AFM-measured plots of samples of different types.

Type #3 sample shows reduced A , confirming its direct dependence on Λ , which is relatively lower, as stated in equation (1.6). These data also explain the increased difficulty in measuring the period under optical microscopy to values below 700 nm .

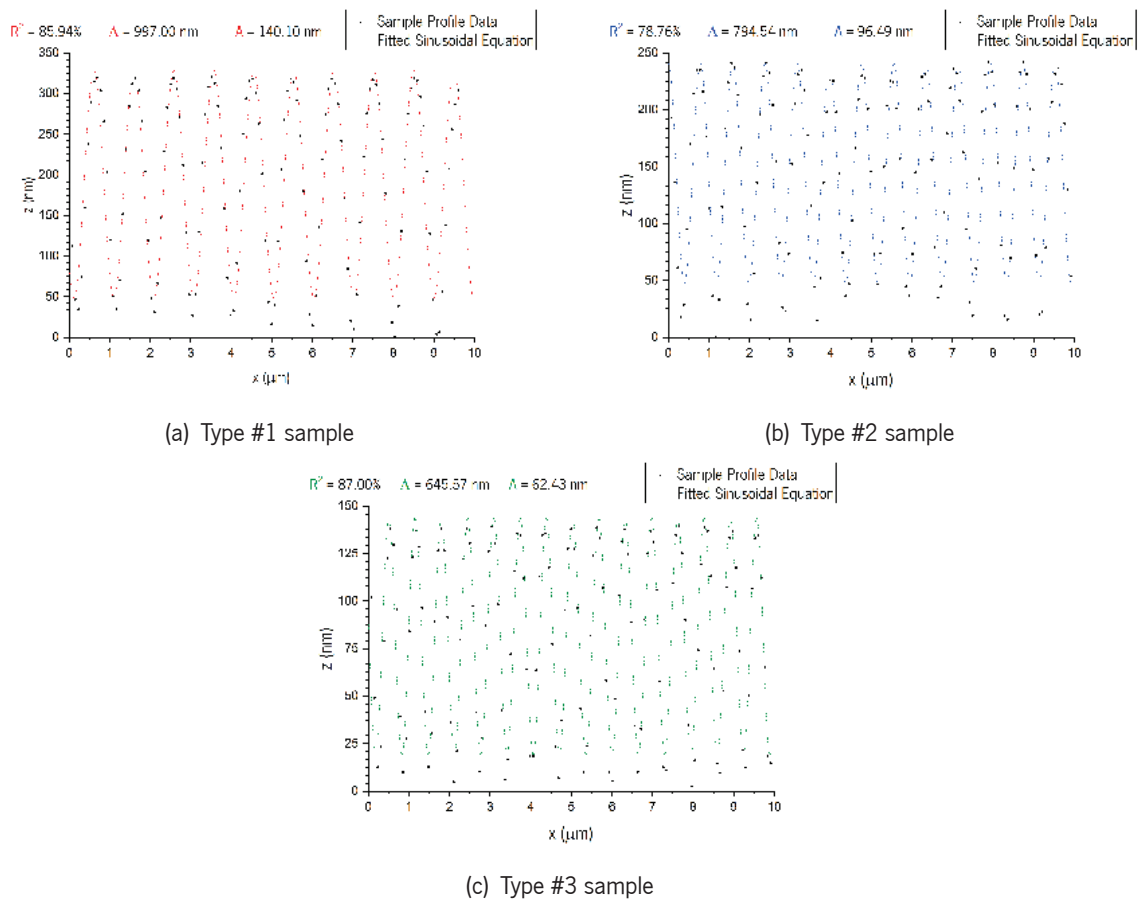


Figure 35: Cross-section profile over plots from figure 34.

Figure 35 shows the cross-section profile measured on type #1 (35(a)), type #2 (35(b)), and type #3 (35(c)) samples, showing successfully fitted sinusoidal regressions with R^2 (equation (B.4)) of 85.94%, 78.76%, and 97.00% respectively. Profile lines used were 1 pixel wide.

Table 3: Comparison between measured Λ at AFM and obtained microscope inspection-based average Λ .

Sample	Λ at AFM	Mic. based Λ	Relative error δ_x
WD7 type #1	997.00	1019.60	2.27%
WD7 type #2	794.54	818.14	2.97%
WD7 type #3	645.57	610.03	5.51%
WD2 type #1	754.03	721.11	4.37%
WD2 type #2	699.45	636.39	9.01%
WD2 type #3	480.77	516.49	7.42%

Furthermore, as evidenced in table 3, values obtained by statistical analysis for the two measured batches have relative errors below 10% regarding the ones measured at AFM, showing the reliability of the statistical processing of the measurements performed. WD is an arbitrary label, not sample properties-related referring to batches fabricated by the method mentioned in 2.3, with varying resting time, and the number of its fabrication.

SEM images of one batch manufactured by the method described in 2.3 were obtained to confirm the morphological status of the materials. All results obtained are present in appendix C.4.

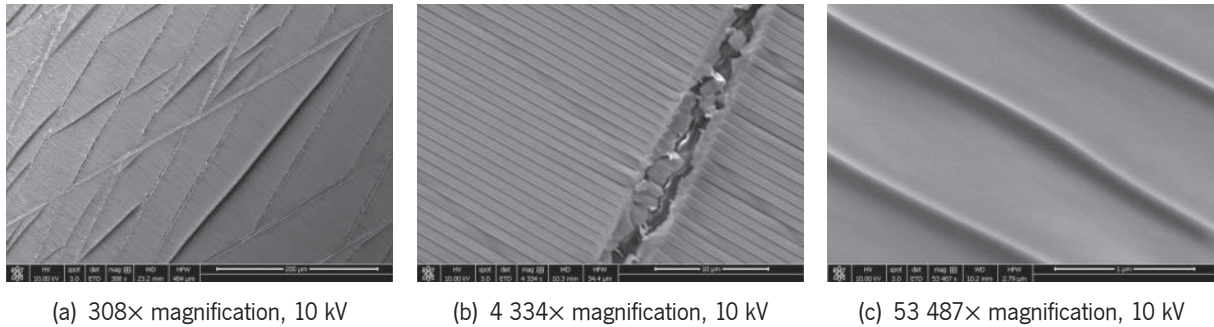


Figure 36: SEM images of type #1 sample from WD7. Directional sputtered gold coating.

Through figure 36 one observes the uniformity of the sinusoidal features of the fabricated nanostructures, both in terms of amplitude and period. It is noticed in 36(b) that cracks on the surface are due exclusively to the skin layer since it is possible to observe the substrate inside the valley. The frequency of their appearance will be greater the smaller the skin layer's thickness. Since the gold coating applied to the batch from figure 36 was carried out by a directional sputtering, gold was mostly deposited in the depressions of the sinusoidal surface, giving the appearance of a flat surface with small periodic reliefs. This in any way compromises the functioning of the nanostructure as a diffraction grating, since Λ is kept constant.

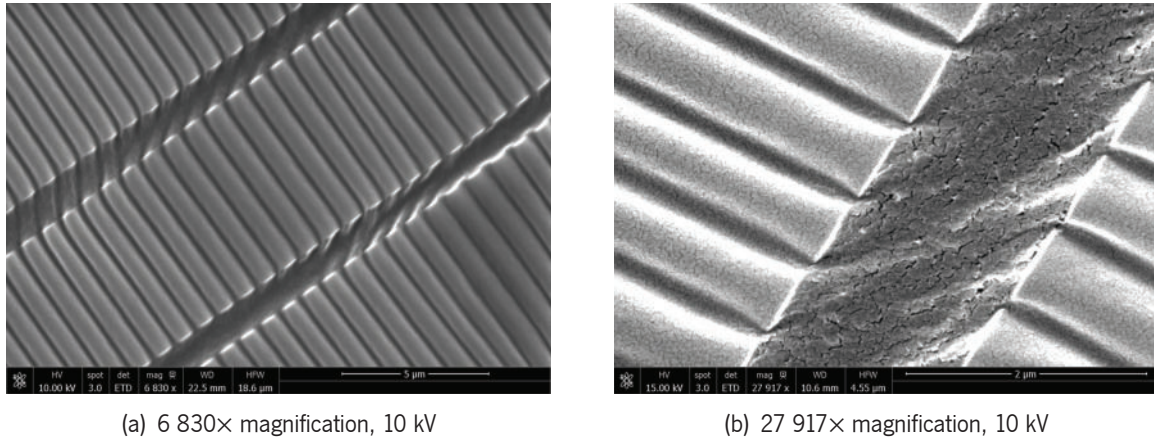


Figure 37: SEM images of type #1 sample from RB8 (without transferred graphene). Diffuse sputtered gold coating.

In the case of figure 37, the gold coating was performed by a diffusive sputtering, meaning a more conformal particle deposition. In 37(a) and 37(b), the surface's sinusoidal profile is more noticeable compared to figure 36. Furthermore, in 37(b), a dry-terrain texture is noticeable on the surface of the *nanowrinkles'* peaks and on the crack's valley, which combines with the fragility of the skin layer's silica-like material.

2.5 Optical Characterization

The optical characterization of the 3D nanostructure is as important as its morphological analysis. While morphological analysis indicates the state of the features of the diffraction grating, optical characterization confirms experimentally the results of the incidence or passage of light through the device.

The chosen materials in section 2.1 have very low reflectance in the VIS+NIR spectrum. Since the goal is to confirm that the nanostructure behaves as an optical diffraction grating, measured samples were coated with a 20 nm thin film of gold by sputter, thus improving the surface reflection in the light spectrum of interest [76]. In this regard, measured samples in 2.4 were reused. All measurements were performed with non-polarized light. Samples fabricated by the method mentioned in 2.3 were measured in the spectrograph path of the Fourier setup (see section 1.3.2), hence by angular reflection spectrophotometry. All results obtained are present in appendix C.5.

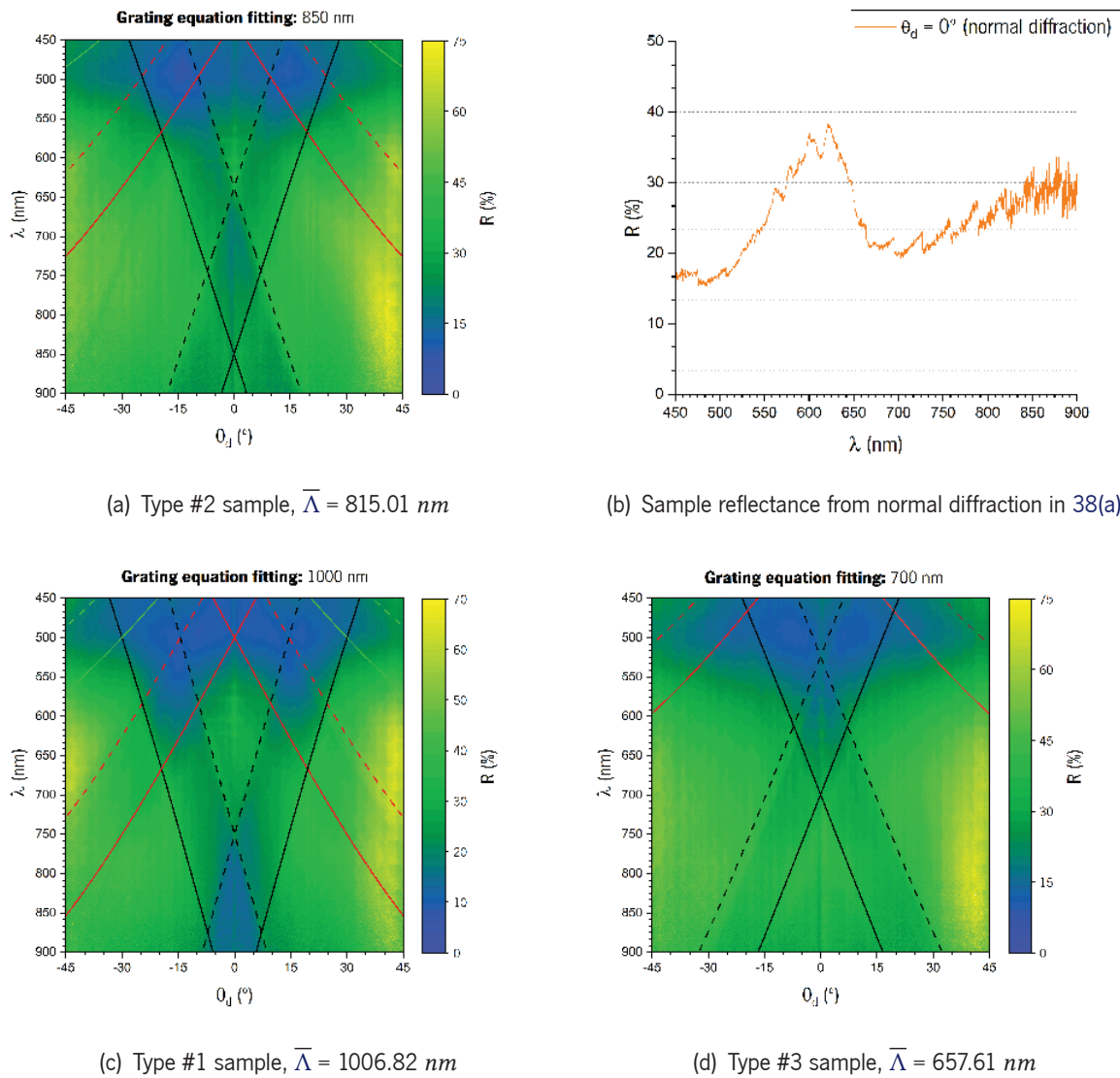


Figure 38: Angular reflectance plots of samples fabricated by the method described in 2.3. Reflectance color map (from blue to yellow) as a function of angle of reflection and λ . The black, red, and green solid lines correspond to the arranged diffraction orders $m = 1$, $m = 2$, and $m = 3$ respectively, plotted using equation (1.4). The dashed lines match the reentry of light.

Measurements show a dip in reflectance corresponding to the grating's first order of diffraction. This gap is due to the performed measurement, which measures the light reflected from the sample's surface, corresponding to the amount of diffracted light from the incident beam, according to the equation (1.3). If the measurement analyzed transmission instead, the angular reference would change according to the convention from figure 8. The result would be an angle-independent reflectance increase centered on the normal axis ($\theta_d = 0^\circ$) with maximum intensity, coincident with the transmitted light through the device. Reflectance gaps matching the dips in figure 38 of high intensity would also appear, corresponding to the respective orders of the light diffracted by the *nanowrinkles*.

Up to 3 orders of diffraction are expected from the theoretical plotting due to the *nanowrinkles*' larger

Λ . The existence of a second diffraction order is barely perceptible due to a slight color gradient inside the first diffraction order band on samples 38(a) and 38(c). This effect is complemented by the surface irregularity discussed in section 2.4. 38(b) shows the reflectance dependence on incident light's λ from normal diffraction (θ_d) for the measured sample on 38(a). The dip in reflectance on sample 38(d) is barely noticeable even for the first order due to its reduced A , which influences the diffraction grating efficiency, as discussed in section 2.1. All measurements have a general decrease in reflectance at $\lambda \leq 500 \text{ nm}$. This phenomenon is due to the increase in light absorption of gold for this wavelength range [76].

Integration of the Two-dimensional Material

Last step for the final device. Transfer methodology of the two-dimensional material onto the photonic nanostructure and further characterization.

This chapter describes the transfer process of the 2DM to the surface of the photonic nanostructure, whose manufacturing process was developed in chapter 2, briefly analyzing the morphological and optical properties of the set.

3.1 Graphene as an Optoelectronic Material

As described in 1.2.1, there are several options for two-dimensional materials with optoelectronic properties consonant for the device. Graphene is the 2DM with the best electronic properties, comparing table (TMDCms) quantities with those referred to in 1.2.1.1. In addition, it provides a high thermal dissipation that avoids unnecessary overheating effects and has the largest SSA – a relevant factor in the device's working principle, as mentioned in section 1.2.2. Figure 4 shows the lower light absorption in the VIS spectrum of graphene relative to the most studied TMDCms. This is not a disadvantage since one of the main motivations of the device is to be transparent in this range. Furthermore, its growth processes are currently better established and well-developed, providing better reproducibility, and allowing leeway for any transfer plan change with minimal impact [77].

Particularly, the graphene used will be synthesized through a process based on CVD. This method emerged as one of the most promising for implementing this material in organic photovoltaic cells as transparent and flexible conductors, promoting unique properties in optical and electronic terms due to its high-quality synthesis on a large-scale with good uniformity [78]. Graphene is deposited through the reaction of reactor gases at low-pressure and high-temperature environments. Catalytic metallic substrates such as copper (Cu) are used to help decompose the precursor molecule, usually methane (CH₄), and assist the 2D growth. Then the graphene is coated with PMMA by spin coating, making it strong enough to be transferred to another substrate without damaging the material [79].

3.2 Graphene Integration Methodology

The type of transfer performed influences the final quality of the 2DM, from electronic to optical properties, and should be chosen depending on its type of manufacturing process, dimensions, and shape. In this case, the transfer process should avoid damage to the photonic nanostructure projected in chapter 2. The transfer should allow the use of graphene on the device, providing the least mechanical damage possible, since maximum surface continuity is desired, considering the operating principle mentioned in 1.2.2.

Wet transfers offer the lowest risk of mechanical damage to the 2DM at the expense of higher surface residual dirtiness due to PMMA support layers. This type of transfer is limited to not extensive areas, being difficult to scale up, as indicated in table 2 with a 95% chance of transferring a perfect monolayer [80]. Due to the samples' voluminous shape during the stretching step in the standard process developed in chapter 2, the wet transfer of graphene grown by CVD in a copper substrate is the most fitting procedure.

“Maintaining conformal contact between graphene and polymer substrates is advantageous for controlling the feature size and orientation of textured graphene in spatially defined regions” [81]. For this, graphene must be transferred to the substrate before making the *nanowrinkles*, i.e., in the unclamping step of the PDMS substrate. In summary, the experimental method is based on stretching a PDMS substrate, followed by an oxygen-plasma treatment of its surface, thus creating a thin silica-like layer on top, as discussed in section 2.3. The graphene is then transferred onto the surface by a wet method, and finally, the sample is released, producing the intended nanostructure with corrugated graphene, as shown in figure 39.

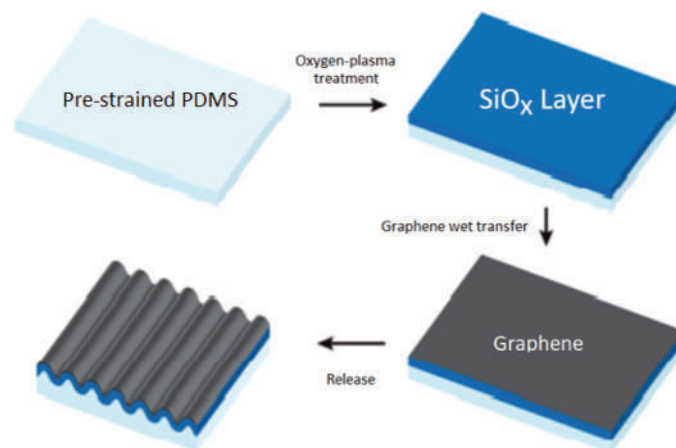


Figure 39: Summary diagram of the complete fabrication procedure of the device. Adapted from [81].

The graphene transfer method, as well as the material and used equipment, is described step by step in appendix A.2, duly illustrated.

Batches of samples fabricated by this method were measured in zones with transferred graphene with the procedure mentioned in 1.3.3.

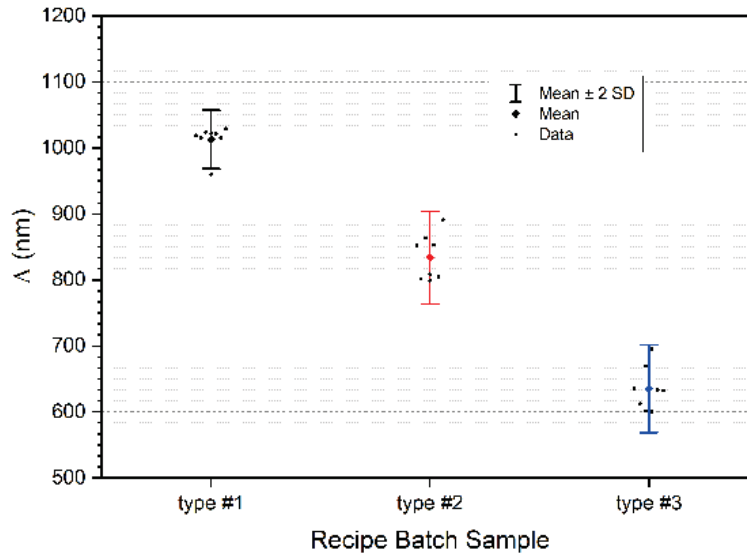


Figure 40: Statistical analysis of fabrication method mentioned in the current section.

Figure 40 shows measured Λ on different spots by the method mentioned in section 1.3.3 by sample type. The achieved Λ are similar to those obtained for samples without graphene (≈ 600 , 800 , and 1000 nm) with an error within the range of 2 standard deviations, which guarantees 95.44% statistical confidence.

3.3 Surface Quality Control

As mentioned in appendix A.2, etching the PMMA support layer requires total immersion of the sample in pure acetone is required for an overextended time of 2 straight hours. Acetone (C_3H_6O) is a weak PDMS solvent as it has a swelling ratio of $\log_{10}S < 0.05$. This is due to the weak polar contributions of both PDMS as solute and acetone as solvent (dot 22 on figure 41), contrasting for example with methylene chloride (CH_2Cl_2) (dot 16 on figure 41), whose polar contributions are strong, despite having the same solubility parameter¹ $\delta_{solv} = 10 \text{ cal}^{1/2} \text{ cm}^{-3/2}$ [82].

¹numerical value that indicates the relative solvency behavior of a specific solvent

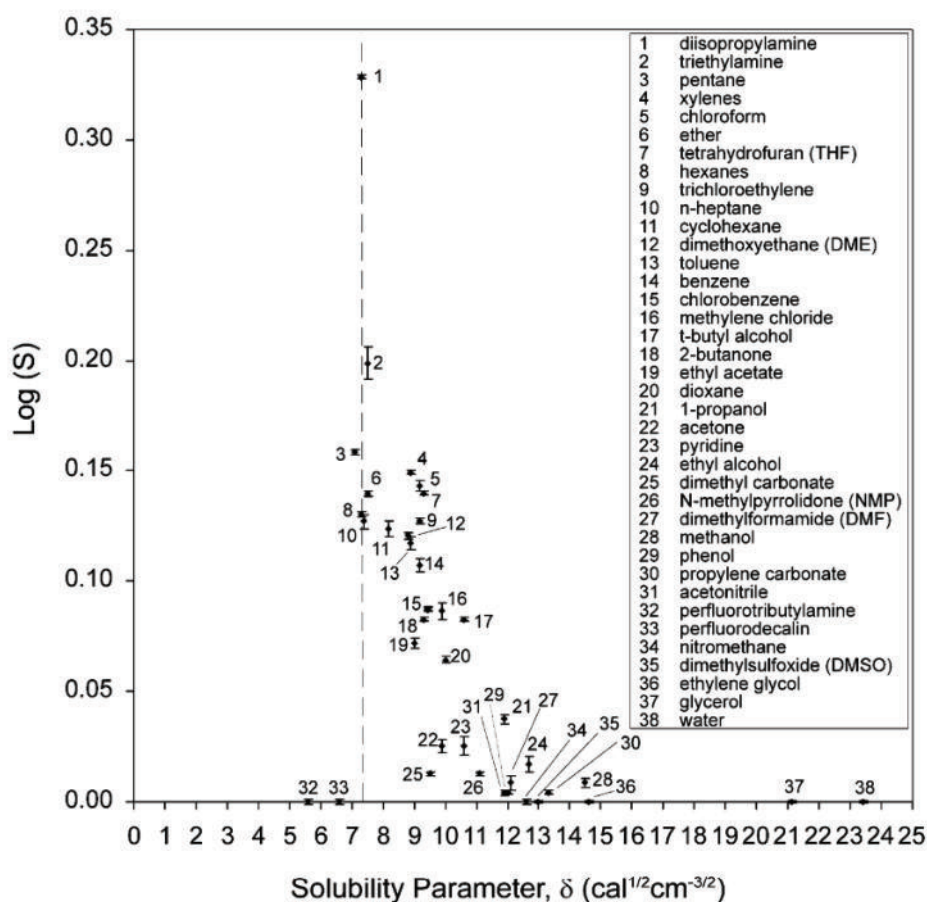


Figure 41: Relationship between swelling ratio (S) (shown as $\log S$) of PDMS in various solvents and the solubility parameter (δ) for these solvents. The solvents are numbered in order of decreasing swelling ability (e.g., 1 has the most swelling ability and 38 has the least swelling ability). The dashed line indicates the solubility parameter of PDMS ($\delta_{solu} = 7.3 \text{ cal}^{1/2} \text{ cm}^{-3/2}$). Retrieved from [82].

PMMA, like PDMS, is a solute with weak polar contributions [83] Its solvent compatibility is quite similar to the latter, having so the same set of solvents.

Despite low solubility, exposure of PDMS in acetone for long intervals, such as the 2 hours required to remove the PMMA support film, promotes reversible damage² to the lower interface and edges of the substrate. The low dissolution rate causes a slight shrinkage of the substrate, breaking the fragile and thin skin layer. This phenomenon causes cracks and tensile strains that generate surface instabilities, giving rise to uncontrollable nanostructures by the same process referred to in section 1.2.4, which could compromise the quality of graphene transferred at the top of the device.

To test the robustness of the appearance of surface disorders or fissures due to the transfer procedure, three flat samples of PDMS treated by oxygen plasma under the conditions mentioned in 2.3 were submitted to a pure acetone bath, at intervals of 15, 30, and 60 minutes until they totaled 2 hours, interspersed by isopropyl alcohol ($\text{C}_3\text{H}_8\text{O}$) and deionized water rinsing and drying of 1 hour to investigate the effect of the time of continuous exposure on the PDMS substrate.

²it returns to the initial state after long periods at rest

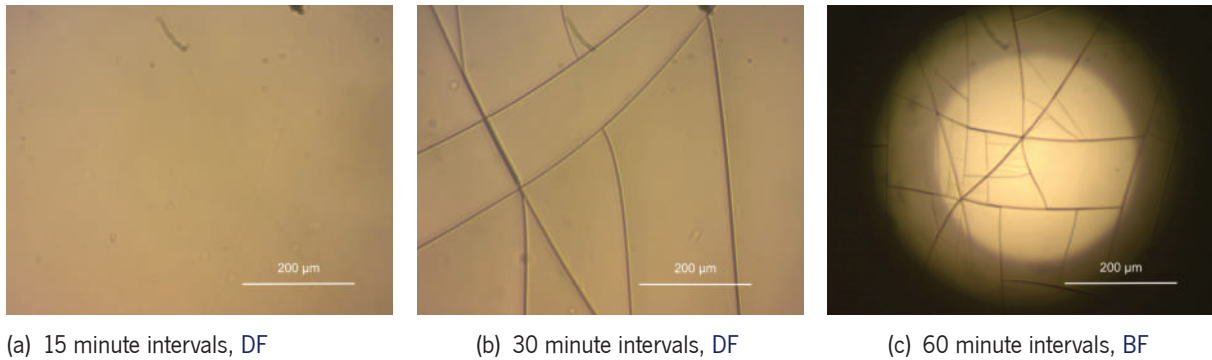


Figure 42: 4× objective images of flat PDMS treated by oxygen plasma after pure acetone bath with different duration. All images taken are shown in appendix C.1.

As shown in figure 42(b) and figure 42(c), the shrinkage effect of the substrate is visible for 30 and 60 minutes intervals respectively. Besides this deep cracks and uncontrolled surface instabilities appear at the microscopic scale. For 15 minutes intervals, the substrate remained stable, exhibiting shallow cracks with the absence of uncontrolled surface instabilities.

3.4 Morphological Analysis

Following are images from samples manufactured by the process mentioned in section 3.2 in spots with and without transferred graphene. These samples were overexposed to oxygen plasma during their manufacture, thus giving higher Δ to ease the analysis under an optical microscope. All taken images are in the appendix C.1.

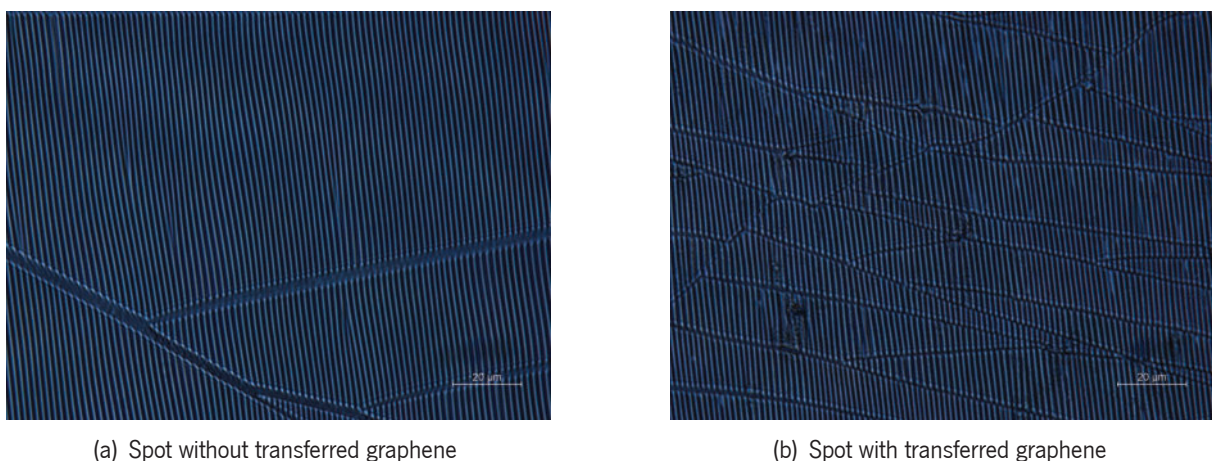


Figure 43: Type #2 sample fabricated by the process mentioned in the section 3.2, with 30 minutes of oxygen-plasma treatment.

A higher number of cracks is noticeable in spots with graphene, maintaining consistency in terms of Δ and A , after comparing figures 43(a) and 43(b).

The Raman spectrum was collected from four different flat samples: graphene on glass, graphene on untreated PDMS, graphene on oxygen plasma-treated PDMS without resting time³, and graphene on oxygen plasma-treated PDMS with 72 hours of resting time to verify the impact of each substrate type on the quality of the transfer. All results obtained are present in appendix C.3.

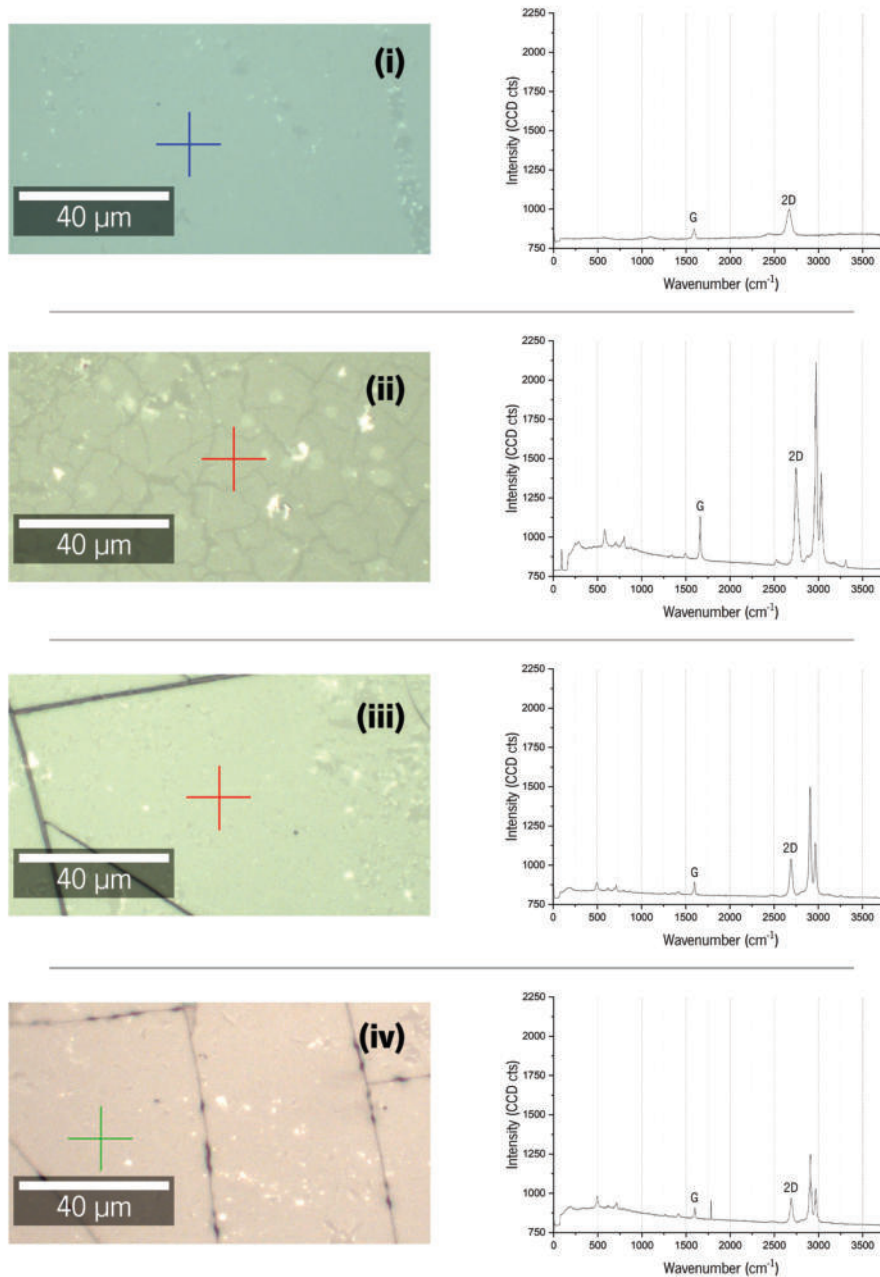


Figure 44: Raman analysis of graphene transferred onto different substrates. **(i)** the substrate is glass (SiO₂). **(ii)** the substrate is untreated PDMS. **(iii)** the substrate is oxygen plasma-treated PDMS with no resting time afterwards. **(iv)** the substrate is oxygen plasma-treated PDMS with 72h resting time. The Raman spectrum was collected on each colored cross. The integration time used was 1 s, with 10 acquisitions.

³time interval counting right after oxygen plasma treatment

Graphene was successfully transferred onto any kind of substrate from figure 44 since it does not show structural damage, as every Raman spectrum collected at zones identified as graphene exhibits well-defined G and 2D peaks.

In addition, a graphical analysis of G and 2D Raman graphene bands was performed to evaluate graphene quality. The ratio between 2D and G band peaks, I_{2D}/I_G , as well as the G band peak center wavenumber κ_G are the main characterizing elements. The first element should be equal to 2 for graphene monolayers [84]. The latter approximates the number of graphene layers through the following equation [85]:

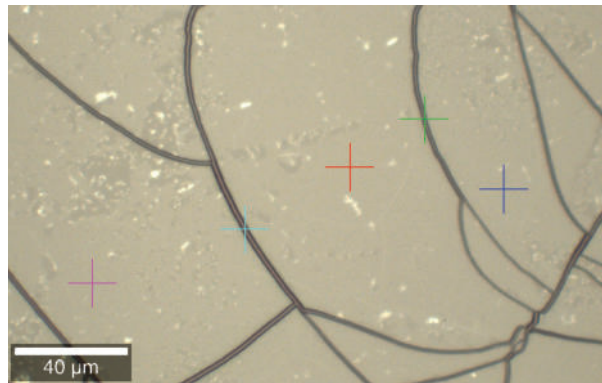
$$\kappa_G = 1581.6 + \frac{11}{(1 + n^{1.6})} \quad (3.1)$$

Table 4: Graphical analysis of G and 2D Raman band peaks of graphene transferred onto different types of substrates. **(i)**, substrate is glass (SiO₂). **(ii)**, substrate is untreated PDMS. **(iii)**, substrate is oxygen plasma-treated PDMS with no resting time afterwards. **(iv)**, substrate is oxygen plasma-treated PDMS with 72h of resting time.

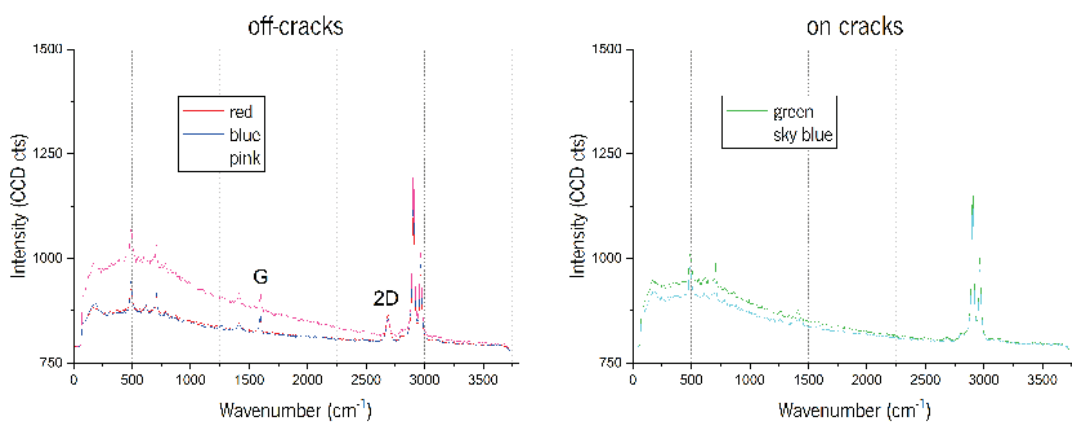
Substrate	I_{2D}/I_G	$\kappa_G (cm^{-1})$	n : eq. (3.1)
(i)	2.60	1592.55	1
(ii)	2.25	1660.60	1
(iii)	2.71	1600.59	1
(iv)	2.49	1600.59	1

Table 4 shows the mentioned values nearly expected for a graphene monolayer in all substrate types.

However, for PDMS substrates treated either with or without resting time, high 2DM shattering is noticed due to the phenomenon triggered by the acetone dissolution of PDMS discussed in section 3.3 and by substrate unstretching procedure. This skin layer's shattering causes graphene rupture, as the absence of typical G and 2D Raman bands is noticed in measurements carried out on spots within cracks, as shown in figure 45. A similar effect is observed on untreated PDMS substrates. Furthermore, the skin layer chemical structure discussed in section 2.1.2 does not seem to influence graphene's quality, as no difference is noticed in Raman spectra measured between substrates **(iii)** and **(iv)**.



(a) Raman's spectrum collected spots (colored crosses).



(b) Collected Raman's spectra. Integration time of 1s, 10 acquisitions.

Figure 45: Raman analysis of graphene transferred onto **(iii)** oxygen plasma-treated PDMS with no resting time afterwards. Red, blue, and pink crosses are collected spectra on spots off-cracks. Green and sky blue crosses are collected spectra on cracks. Cracks are $\approx 1 \mu\text{m}$ wide.

One batch of samples manufactured by the method described in 3.2 was measured at AFM to understand the state of the *nanowrinkles'* periodic features concerning their amplitude and periodicity on spots with and without graphene. All obtained results are present in appendix C.2.

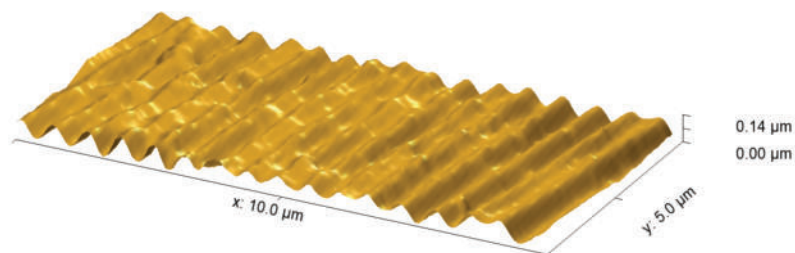


Figure 46: AFM-measured 3D representation of a type #3 sample with transferred graphene.

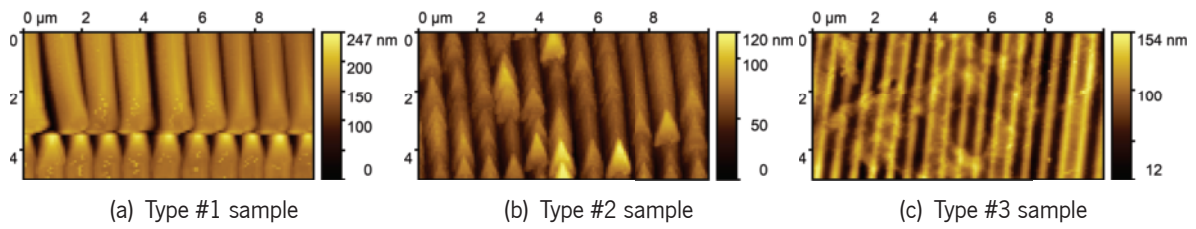


Figure 47: AFM-measured plots of samples with transferred graphene.

Figure 47 shows that consistency in Λ remains in zones with transferred graphene. Moreover, a decrease in A is noticed when compared to samples without transferred graphene (figure 34). This decrease is due to polymeric residues from the PMMA etching step and lack of adhesion from graphene onto the skin layer surface.

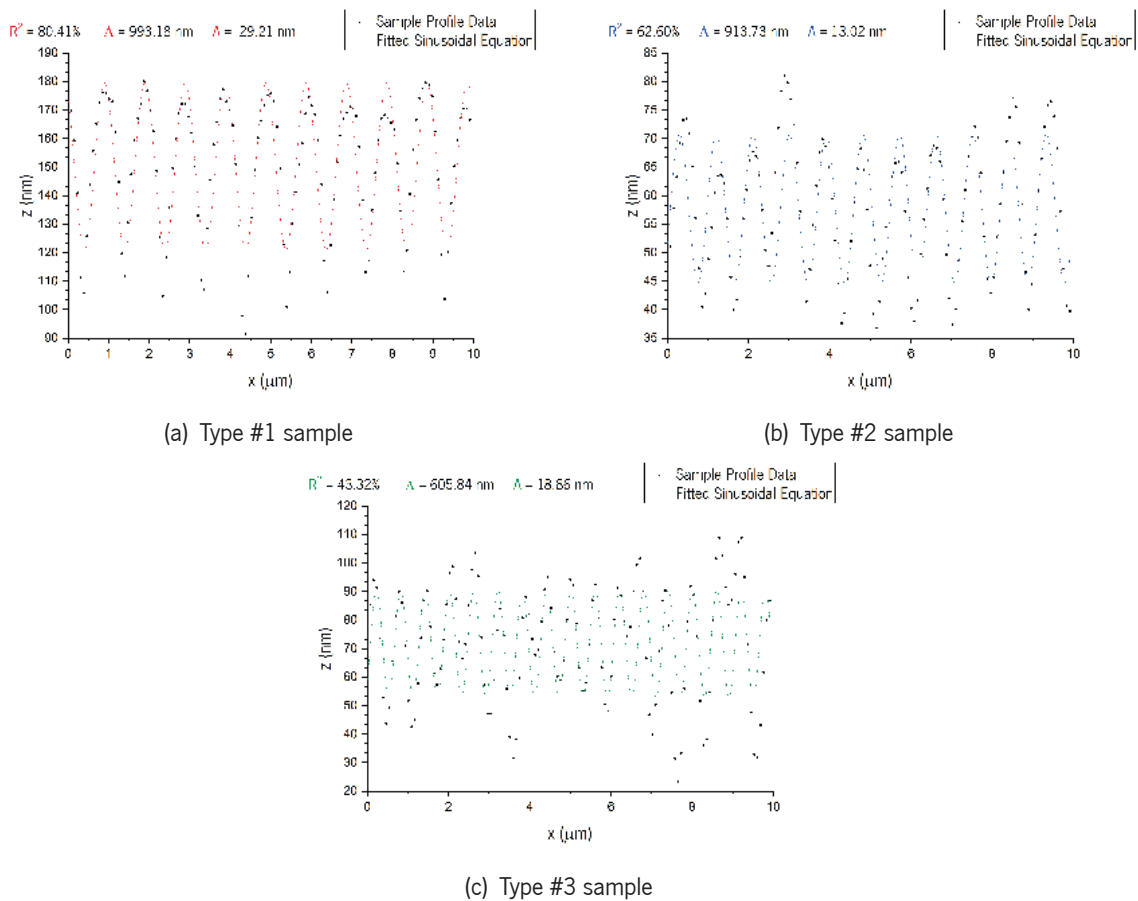


Figure 48: Cross-section profile over plots from figure 47.

Figure 48 shows the cross-section profile measured on type #1 (48(a)), type #2 (48(b)), and type #3 samples (48(c)), showing successfully fitted sinusoidal regressions with R^2 (equation (B.4)) of 80.41%, 62.60%, and 43.32% respectively. Profile lines used were 1 pixel wide. These values show the increased difficulty in corrugating graphene with a good sinusoidal trace, after comparing with the results obtained in section 2.4 in the same type of analysis.

Table 5: Comparison between measured Λ of samples with graphene at AFM and obtained microscope inspection-based average Λ .

Sample	Λ at AFM	Mic. based Λ	Relative error δ_x
RB6 type #1	993.18	1013.06	2.00%
RB6 type #2	913.73	833.99	8.73%
RB6 type #3	605.84	634.94	4.80%

As shown in table 5, values obtained by statistical analysis for the measured batch still have relative errors below 10% regarding the ones measured at AFM. RB is an arbitrary label, not sample properties-related referring to batches fabricated by the method mentioned in 3.2 and the number of its fabrication.

3.5 Optical Characterization

A type #1 sample fabricated by the method mentioned in 3.2 was measured in the spectrograph path of the Fourier setup (see section 1.3.2), hence by angular reflection spectrophotometry.

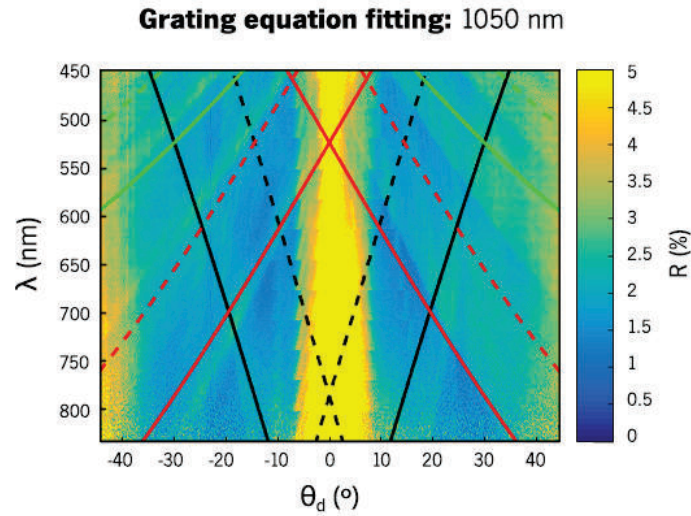


Figure 49: Angular reflectance plot of a type # 1 sample, $\bar{\Lambda} = 980.32 \text{ nm}$. Reflectance color map (from blue to yellow) as a function of angle of reflection and λ . The black, red, and green solid lines correspond to the arranged diffraction orders $m = 1$, $m = 2$, and $m = 3$ respectively, plotted using equation (1.4). The dashed lines match the reentry of light.

After saturating the reflectance color map⁴ from figure 49, the borders between dips in the reflectance show the presence of the first (black), second (red), and third (green) orders of diffraction of the grating. The broad intensity band in reflectance centered at normal reflection ($\theta_d = 0^\circ$) is due to the saturation of the color map but also to the back reflectance inherent to the used lens (40 \times). Therefore, this could not

⁴achieved by reducing the maximum value on the color scale to very low values

have been removed. Furthermore, it was shown the possibility of obtaining wrinkled surfaces with optical grade quality even after integrating graphene by a wet transfer method.

Optoelectronic Wrinkled Graphene

Device preparation for electric current induction and optoelectronic tuning according to nanostructure's features.

Finally, electrical contacts are added to the system. This chapter characterizes the device developed in the previous in terms of its **optoelectronic** properties, as suggested in section 1.2.1. First, the hurdles to obtain conductivity over large-area graphene on wrinkled **PDMS** treated by oxygen plasma are described. Then, possible solutions will be identified, presenting successful results of conductance on the system.

4.1 Electrical Contacts

The integration of electrical contacts is crucial in the final device's development, allowing the flow of current to the device from a power supply or battery, an important step in any process of electronic analysis of systems. The electronic performance of graphene will influence the result of the measurements made in this chapter. With this, it is important to take into account the effect of nanostructuring on this material. Particularly, wrinkled monolayers are known to cause an increase in graphene conductivity [86].

4.1.1 Conductive Silver Ink

The first attempt at implementing electrical contacts was using conductive silver ink. This technique allows the creation of contact zones for electrical probes with graphene without mechanical damage. Nevertheless, the distance between contacts has a resolution limit that doesn't go lower than the order of magnitude of one millimeter, depending on the user, since it is a manual procedure.

RS PRO™ Conductive Silver Ink was used. Conductive ink was gradually deposited, using a volumetric pipette, at a volume of 50 μL at each pipetting. The layout of the deposit is presented in figure 50. The sample was then left to dry out at room temperature for 24 hours, avoiding the use of ovens at high temperatures. The low thermal conductivity of **PDMS** prevents the rapid dissipation of heat, creating a high thermal gradient, which leads to faster drying of the silver paint at its ends, causing its separation

from graphene. However, when using higher thermal conductivity substrates such as glass (SiO_2) the same does not happen, and ovens can speed up the process. Appendix A.3 shows images of the method and some results in samples manufactured by the process described in section 3.2.

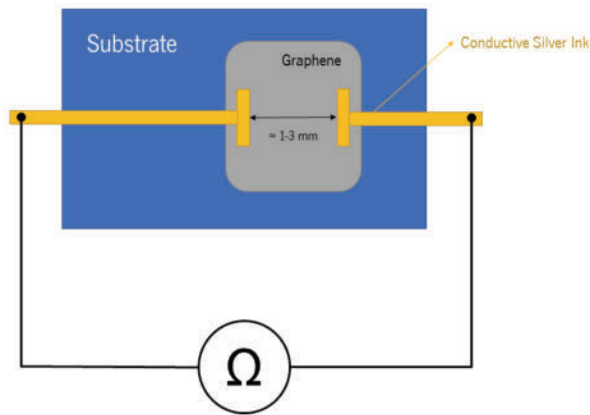


Figure 50: Conductive silver ink contacts implementation and conductance test schematic



Figure 51: Conductive silver ink contacts implementation on graphene on glass.

Flat samples of different substrates were tested to verify their influence on transferred graphene quality. Table 6 shows the influence of the appearance of cracks in the substrate on graphene conductance. The consequent breakage of the transferred graphene, as shown in figure 45, prevents electric current from flowing, which is noticed in the infinite resistance measured by the implementation of electrical contacts in figure 50. In conclusion, the graphene rupture makes macroscopic-scale contacts impracticable, as it is necessary to implement them in a more localized way.

Table 6: Table of graphene conduction test results on flat substrates. The experiment schematic is shown in figure 50.

Substrate Type	Cracks Appearance	R_{graphene}
Glass (SiO_2)	✗	$\sim 1 \text{ k}\Omega$
Untreated PDMS	✓	—
Treated PDMS (no delay)	✓	—
Treated PDMS (72h delay)	✓	—

4.1.2 Gold Sputtering

Since conductive silver ink did not deliver the needed performance, more accurate methodologies for implementing contacts were chased. Following was the implementation of gold contacts through a sputtering chamber, using a LASER-inscribed poly(ethylene) terephthalate shadow mask with the layout shown in figure 52.

Gold is a metal with weak interactions with non-metallic surfaces [87]. The insertion of electric needles in simple contacts of pure gold would cause detachment and graphene's mechanical damage. In sputtering applications, it is common to grow an additional thin adhesion layer made of a robust gold-bonding metal at the interface between these materials, such as palladium (Pd), copper (Cu), nickel (Ni), or chromium (Cr). The adhesion layer strengthens electronic bonds between the substrate and the contacts [88]. Copper (Cu) and nickel (Ni), also used as native substrate metals for graphene growth processes, are ideal candidates for this end [89].

Two masks of different contact distances were fixated onto each sample, sputtering a 5 nm-thick copper adhesion layer followed by a 15 nm-thick thin film of gold. Since the position of the cracks is random and mostly with orientation perpendicular to the wrinkles' orientation and distanced by values in the order of one micrometer, this method consists in implementing contact distance with equal or lesser resolution limit, allowing current to flow in continuous areas of graphene in the samples. The contact distances in figure 52 were chosen according to measured areas in images shown in chapter 2.

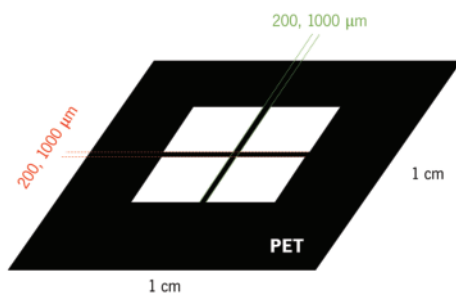


Figure 52: LASER-inscribed poly(ethylene) terephthalate shadow mask layout.

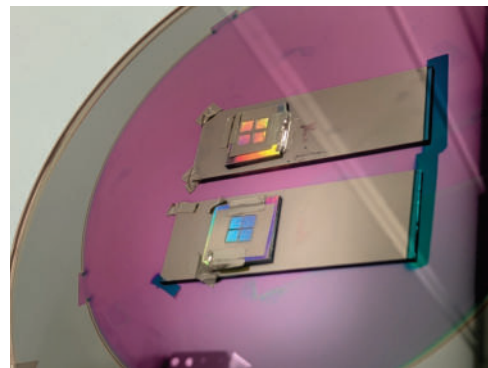


Figure 53: Samples with a shadow mask, tapped to a silicon wafer right after sputtering.

Two samples manufactured by the method mentioned in section 3.2 were analyzed under an optical microscope to check if continuous areas were obtained between deposited contacts. These samples were overexposed to oxygen plasma during manufacture, thus giving higher Δ to ease the analysis under the optical microscope. Additional images from these samples follow in appendix C.1.

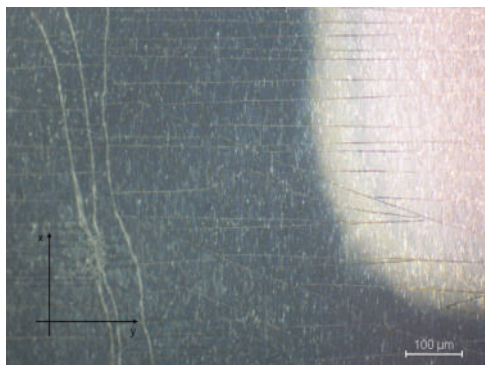


Figure 54: 20× objective image of sample fabricated by the method mentioned in section 3.2 with contact distance of 1 mm. The bright zone is a corner of one sputtered gold contact. The coordinate system is the same as figure 28.

Figure 54 shows that for distances between contacts of 1 mm , graphene continuity between contacts is not achievable. As mentioned in section 2.4, cracks appear mostly with perpendicular orientation to the stretching direction, and the continuous graphene areas merge before reaching the second contact anywhere. Furthermore, the sputtered layers, specifically the copper adhesion layer, and the gold layer, are noticeable through a slight gradient at the edges of the electrical contact. This effect is due to the greater diffusion of copper relative to gold as a sputtered material.

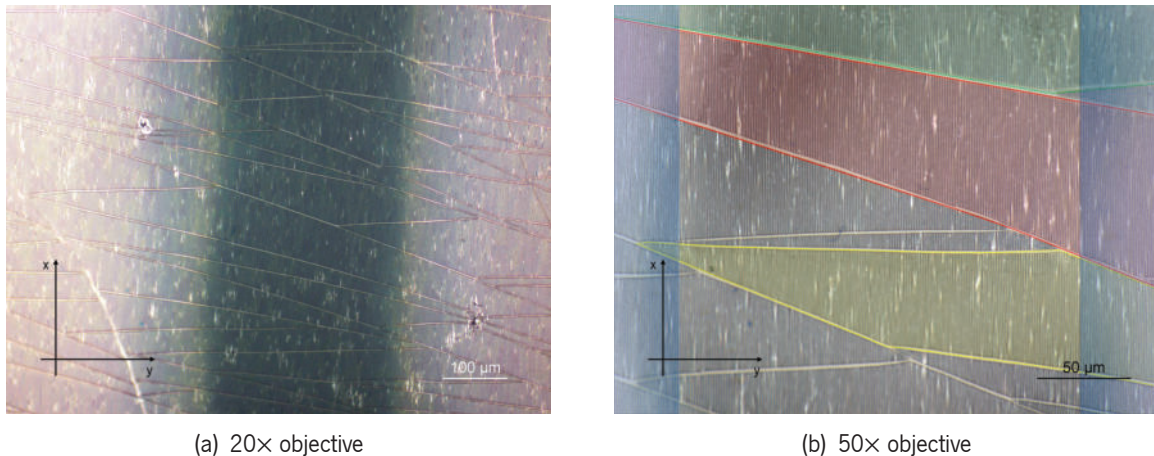
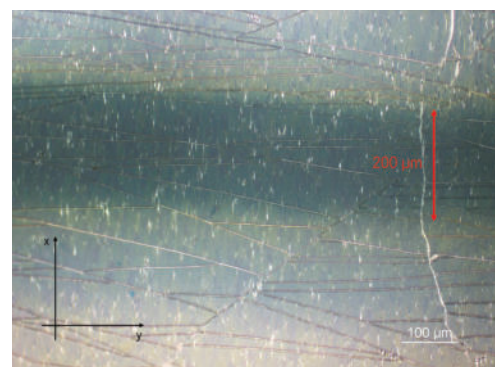


Figure 55: Images of a sample fabricated by the method mentioned in section 3.2 with contact distance of $200\ \mu\text{m}$ in the stretching direction. Bright zones are sputtered gold contacts. Green, red, and yellow highlighted zones are continuous graphene areas from one contact to another (blue zones). The coordinate system is the same from figure 28.

In contact distances of $200\ \mu\text{m}$ continuous areas between contacts were obtained, as shown in figure 55. Even so, despite being conductive and frequent throughout the sample, these areas do not have the necessary shape and size to form a graphene square, therefore maintaining the resistance value mentioned in section 1.2.1.1. Furthermore, continuous graphene areas longer than a few tens of micrometers between electrical contacts only appear in the substrate's stretching direction, since cracks appear similarly. In figure 56 it is noticed the absence of these areas from one contact to another.

Figure 56: $20\times$ objective image of a sample fabricated by the method mentioned in section 3.2 with contact distance of $200\ \mu\text{m}$ perpendicular to the stretching direction. Bright zones are sputtered gold contacts. Arrow represents the distance between gold-sputtered contacts. The coordinate system is the same as figure 28.



In between uniform areas, the device should behave as expected, and therefore with contacts with the right orientation optoelectronic properties could be properly inspected.

4.2 Electronic Inspection

The best way to confirm the proper functioning of the final device is to test the **direct current (DC)** conductivity of the **2DM** between implemented contacts. For the device to be efficient and stable, its intrinsic properties must remain constant, independently from the flowing current. Ohm's law shows that the resistance R is exclusively dependent on physical properties associated with the device, such that there is a direct dependence defined by this quantity between the applied voltage V and the injected current I [90]:

$$R = \frac{V}{I} \quad (4.1)$$

This experiment searches for linear variations of the induced current as a function of the applied voltage and defines the value of graphene's resistance R between contacts through equation (4.1).

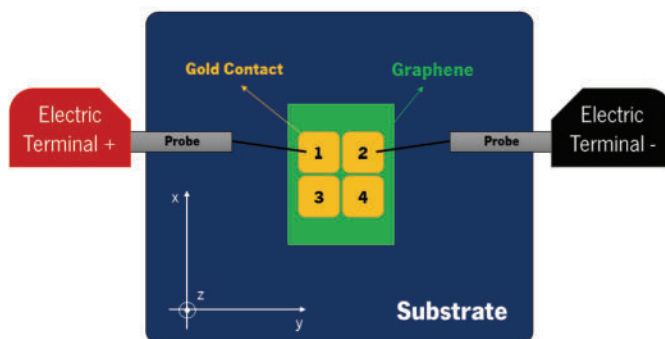


Figure 57: Electrical needle probes for 2DMs setup schematic. The coordinate system is the same as figure 28. Skin layer cracks preventing graphene performance are expected along the y -direction.

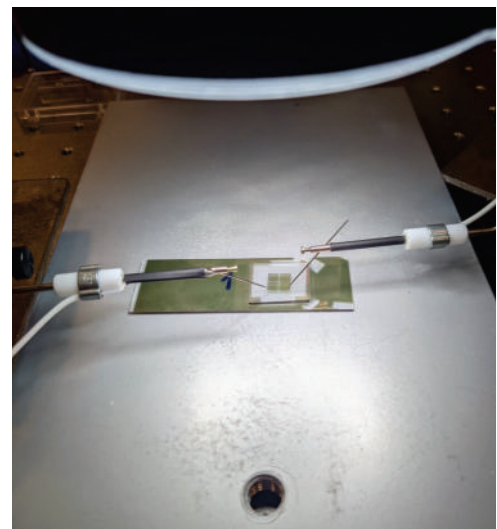


Figure 58: Picture of the electrical needle probes setup, represented by the schematic of figure 57.

Figure 57 shows the schematic of the experiment, where a voltage is applied between two terminals through metallic needles that gently touch the gold surface of each electrical contact. The voltage was symmetrically swept to test both directions of conduction, measuring the current flowing from one contact to another.

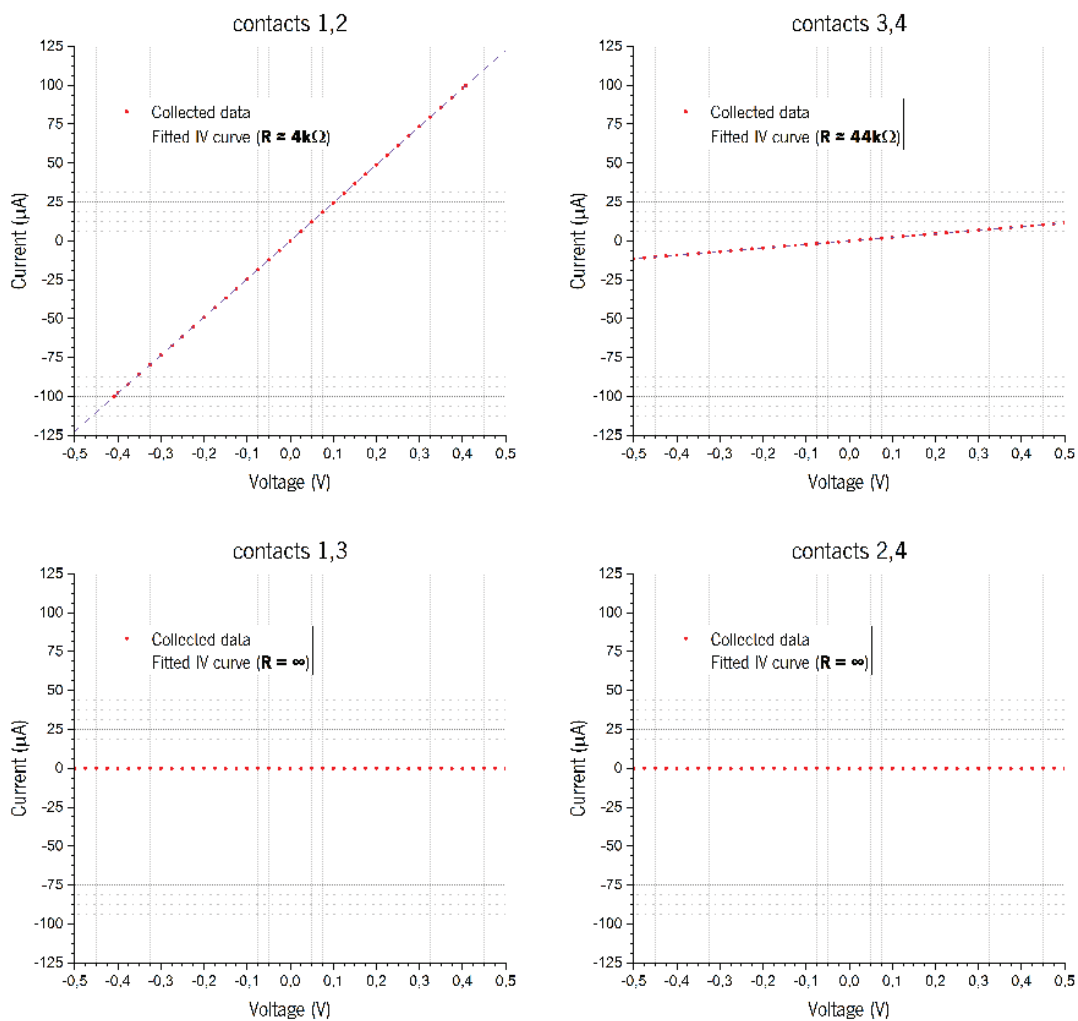


Figure 59: Current–voltage characteristics of a sample fabricated by the method mentioned in 3.2 on each pair of contacts numbered, according to figure 57.

As shown in figure 59, the characteristic curves between side-by-side contacts in the substrate stretching direction (1,2 and 2,4) have perfect linearity, as $R^2 = 1$ (equation (B.4)). Between contacts 1 and 2, $R = 4 k\Omega$ was calculated, an order of magnitude above the value mentioned in 1.2.1.1. Between contacts 3 and 4, $R = 44 k\Omega$, two orders of magnitude above this value. These deviations depend on the state of the measured graphene monolayer. In this case, higher graphene shattering raises the measured value, as less area through which the electrons can circulate is available. The current flowing between vertically oriented contacts (1,3 and 2,4) remained residual for any applied voltage due to the lack of connection between contacts with continuous graphene areas, as explained by the phenomenon reported in figure 56.

General Conclusions

Artificially synthesized 2DMs are one of the building blocks of future optoelectronic devices due to their unique optical, electronic, and mechanical properties. Plus, they can be introduced in devices without affecting their final footprint. On the other hand, nature shows numerous forms and types of mechanisms for obtaining and converting energy with high efficiency. In the research and development of novel optoelectronic devices, one promising strategy is to focus on bioinspired phenomena, i.e., using nature as a blueprint to obtain higher efficiency devices with quick and simple manufacturing processes.

In this project, a literature review was carried out to understand how it would be possible to use 2DMs as precursors of the increase in efficiency of conventional optoelectronic devices and what role had inspiration in biological processes in the manufacture of nanostructures that would support this material. In this case, the reproduction of *nanowrinkles* bioinspired in leaves of the genus *Diplazium*, or in epidermal cells' walls of *angiosperms* was studied, whose optical mode replicates devices based on microcavities to improve light-matter interactions of an adjacent 2DM, specifically graphene.

The use of PDMS treated by oxygen plasma proved to be a simple and speedy strategy in the fabrication of surface corrugations with sinusoidal geometry, capable of reproducing the optical mode of a diffraction grating with the same design. This strategy provided an acceptable reproducibility, evidenced by the relative standard deviation $\%_{\sigma}$ of 1.57%, 1.62%, and 2.54% in the three types of manufactured samples respectively. The appearance of cracks in the skin layer was a phenomenon difficult to control after the chosen material.

The use of graphene proved to be the best alternative due to the better-established synthesis process relative to the most studied TMDCs. Its low absorption in the VIS+NIR spectrum was another reason for its preference over alternatives. The transfer method performed on the target substrate showed good reproducibility and reliability since the grating's periodicity in areas with transferred graphene matched those indicated for *nanowrinkles* without graphene. Furthermore, Raman spectral analysis in areas with transferred graphene showed G and 2D bands consonant with monolayers in good condition. In all samples, cracks in the skin layer caused the rupture of transferred graphene.

This rupture inhibited electrical conduction on a macroscopic scale. On the other hand, cracks created continuous zones in transferred graphene. The implementation of sputtered gold contacts with a distance

between each other of $200\ \mu\text{m}$ allowed the flow of electrical current, as these continuous zones, not thicker than $100\ \mu\text{m}$, connected side-by-side contacts within the substrate stretching direction. The resistance measured in contacts between conductive zones of graphene showed values $R \sim 10^1 - 10^2\ \text{k}\Omega$. These results are in line with the value reported in 1.2.1.1.

5.1 Future Perspectives

The future of this project involves demonstrating *optoelectronic* properties of the final device. Photocurrent generation coincident with the optical mode of the device could be analyzed by electronic gating or through local doping. Another important step is to maximize this phenomenon for a known incident light wavelength. The device manufacturing methodology and the contact implementation process could be tweaked to achieve this with higher precision.

Regarding the first point, the fabrication method of the nanostructure could be improved regarding the stretching mechanism of the substrate. This is the main responsible for the appearance of cracks in the skin layer that compromise the final device's functioning. The stretching and release of the substrate must have a high level of precision, particularly in applied strains perpendicular to the substrate's stretching direction. Even so, the mechanism would have to be nonconflicting with oxygen plasma and with graphene transfer by a wet process. One promising strategy to prevent crack generation in the skin layer is to avoid exposing the pre-stretched PDMS to acetone. Through an unconventional *in-situ* transfer technique, it is possible to integrate graphene without the aid of a PMMA support layer, taking advantage of the dissolution of the copper foil in sodium persulfate ($\text{Na}_2\text{S}_2\text{O}_8$) [91]. The choice of the skin layer material is also a crucial factor in creating surface instabilities and in the appearance of cracks. The use of a stiff enough material relative to the substrate but with greater elasticity than silica (SiO_x), such as carbon fluorides (CF_x) [81], would be a viable alternative in the manufacture without total or partial crack appearance.

Regarding the last point, electrical conduction could be achievable in more precise areas with contact implementation with smaller distances than the ones used in section 4.1.2. More precisely, through lift-off lithographic processes carried out in controlled cleanroom environments, despite being time-consuming, metallic contacts distanced by less than $100\ \mu\text{m}$ and highly located in continuous areas would be easily reachable.

Bibliography

- [1] N. H. PBS and S. L. N. S. Center. *Angiosperms - NatureWorks*. nhpbs.org, 2022. url: <https://nhpbs.org/natureworks/nwep14f.htm> (visited on 10/27/2022) (cit. on p. xviii).
- [2] B. Barnett. "Basic Concepts and Techniques of Video Coding and the H.261 Standard". In: *Handbook of Image and Video Processing* (2005), pp. 777–797. doi: 10.1016/b978-012119792-6/50109-1. url: <https://www.sciencedirect.com/topics/engineering/charge-coupled-device> (visited on 08/25/2022) (cit. on p. xviii).
- [3] N. Mansurov. *What is a Low-Pass Filter?* Photography Life, Jan. 2012. url: <https://photographylife.com/what-is-low-pass-filter> (visited on 08/25/2022) (cit. on p. xix).
- [4] N. Koch, ed. *Supramolecular Materials for Opto-Electronics*. Smart Materials Series. The Royal Society of Chemistry, 2015, P001–369. isbn: 978-1-84973-826-2. doi: 10.1039/9781782626947. url: <http://dx.doi.org/10.1039/9781782626947> (cit. on p. xix).
- [5] E. Cohen and E. J. Lightfoot. "Coating Processes". In: *Kirk-Othmer Encyclopedia of Chemical Technology*. John Wiley & Sons, Ltd, 2011, pp. 1–68. isbn: 9780471238966. doi: <https://doi.org/10.1002/0471238961.1921182203150805.a01.pub3>. eprint: <https://onlinelibrary.wiley.com/doi/pdf/10.1002/0471238961.1921182203150805.a01.pub3>. url: <https://onlinelibrary.wiley.com/doi/abs/10.1002/0471238961.1921182203150805.a01.pub3> (cit. on p. xix).
- [6] R. E. Blankenship. "Origin and early evolution of photosynthesis". In: *Photosynthesis Research* 33.2 (1992), pp. 91–111. issn: 01668595. doi: 10.1007/BF00039173 (cit. on p. 1).
- [7] A. R. Grossman et al. "LIGHT-HARVESTING COMPLEXES IN OXYGENIC PHOTOSYNTHESIS: Diversity, Control, and Evolution". In: *Annual Review of Genetics* 29.1 (1995). PMID: 8825475, pp. 231–288. doi: 10.1146/annurev.ge.29.120195.001311. eprint: <https://doi.org/10.1146/annurev.ge.29.120195.001311>. url: <https://doi.org/10.1146/annurev.ge.29.120195.001311> (cit. on p. 1).

- [8] P. Vukusic and J. R. Sambles. “Photonic structures in biology”. In: *Nature* 424 (6950 2003), pp. 852–855. issn: 00280836. doi: [10.1038/nature01941](https://doi.org/10.1038/nature01941) (cit. on p. 2).
- [9] M. I. Vasilevskiy and I. C. Ferreira. *Física dos Semicondutores. Fundamentos, Aplicações e Nanoestruturas*. Almedina, 2006, pp. 224–226. isbn: 978-9724026541 (cit. on p. 3).
- [10] G. Jarosz, R. Marczyński, and R. Signerski. “Effect of band gap on power conversion efficiency of single-junction semiconductor photovoltaic cells under white light phosphor-based LED illumination”. In: *Materials Science in Semiconductor Processing* 107 (2020), p. 104812. issn: 1369-8001. doi: [10.1016/j.mssp.2019.104812](https://doi.org/10.1016/j.mssp.2019.104812). url: <https://www.sciencedirect.com/science/article/pii/S1369800119318475> (cit. on p. 3).
- [11] L. Ghabuzyan et al. “Thermal Effects on Photovoltaic Array Performance: Experimentation, Modeling, and Simulation”. In: *Applied Sciences* 11.4 (2021). issn: 2076-3417. doi: [10.3390/app11041460](https://doi.org/10.3390/app11041460). url: <https://www.mdpi.com/2076-3417/11/4/1460> (cit. on p. 3).
- [12] N. Kopidakis. *File:CellPVeff(rev210104).png* — *Wikimedia Commons, the free media repository*. [Online; accessed 26-December-2021]. 2021. url: [https://commons.wikimedia.org/w/index.php?title=File:CellPVeff\(rev210104\).png&oldid=608031018](https://commons.wikimedia.org/w/index.php?title=File:CellPVeff(rev210104).png&oldid=608031018) (cit. on p. 4).
- [13] J. Wu et al. “Perspectives on Thermoelectricity in Layered and 2D Materials”. In: *Advanced Electronic Materials* 4.12 (2018), p. 1800248. doi: [10.1002/aelm.201800248](https://doi.org/10.1002/aelm.201800248). eprint: <https://onlinelibrary.wiley.com/doi/pdf/10.1002/aelm.201800248>. url: <https://onlinelibrary.wiley.com/doi/abs/10.1002/aelm.201800248> (cit. on p. 4).
- [14] B. Peng, P. K. Ang, and K. P. Loh. “Two-dimensional dichalcogenides for light-harvesting applications”. In: *Nano Today* 10.2 (2015), pp. 128–137. issn: 1878044X. doi: [10.1016/j.nantod.2015.01.007](https://doi.org/10.1016/j.nantod.2015.01.007). url: <http://dx.doi.org/10.1016/j.nantod.2015.01.007> (cit. on pp. 4, 6).
- [15] Wikipedia contributors. *Graphene* — *Wikipedia, The Free Encyclopedia*. [Online; accessed 22-December-2021]. 2021. url: <https://en.wikipedia.org/w/index.php?title=Graphene%5C&oldid=1061006036> (cit. on p. 5).
- [16] J. Siqueira and O. N. Oliveira. “Carbon-Based Nanomaterials”. In: *Nanostructures* (2017), pp. 233–249. doi: [10.1016/b978-0-323-49782-4.00009-7](https://doi.org/10.1016/b978-0-323-49782-4.00009-7). url: <https://www.sciencedirect.com/topics/chemistry/graphene> (visited on 08/26/2022) (cit. on p. 5).
- [17] S. Zhang et al. “Measuring the specific surface area of monolayer graphene oxide in water”. In: *Materials Letters* 261 (Feb. 2020), p. 127098. doi: [10.1016/j.matlet.2019.127098](https://doi.org/10.1016/j.matlet.2019.127098). url: <https://www.sciencedirect.com/science/article/abs/pii/S0167577X19317306> (visited on 08/26/2022) (cit. on p. 5).

- [18] C. Lee et al. "Measurement of the Elastic Properties and Intrinsic Strength of Monolayer Graphene". In: *Science* 321 (July 2008), pp. 385–388. doi: 10.1126/science.1157996. url: <https://www.science.org/doi/10.1126/science.1157996> (visited on 08/26/2022) (cit. on p. 5).
- [19] K. E. Spear and J. P. Dismukes. *Synthetic diamond : emerging CVD science and technology*. Wiley, Apr. 1994. url: <https://www.wiley.com/en-us/Synthetic+Diamond%5C%3A+Emerging+CVD+Science+and+Technology-p-9780471535898> (visited on 08/26/2022) (cit. on p. 5).
- [20] D. Li et al. "Intrinsic carrier mobility of a single-layer graphene covalently bonded with single-walled carbon nanotubes". In: *Journal of Applied Physics* 115 (June 2014), p. 233701. doi: 10.1063/1.4883759. url: <https://aip.scitation.org/doi/10.1063/1.4883759> (visited on 08/26/2022) (cit. on p. 5).
- [21] W. Contributors. *Electron mobility*. Wikipedia, Aug. 2022. url: https://en.wikipedia.org/wiki/Electron_mobility (visited on 08/26/2022) (cit. on p. 5).
- [22] M. J. Allen, V. C. Tung, and R. B. Kaner. "Honeycomb carbon: A review of graphene". In: *Chemical Reviews* 110 (1 Jan. 2010), pp. 132–145. issn: 00092665. doi: 10.1021/cr900070d (cit. on p. 5).
- [23] A. A. Balandin et al. "Superior Thermal Conductivity of Single-Layer Graphene". In: *Nano Letters* 8 (Mar. 2008), pp. 902–907. doi: 10.1021/nl0731872 (cit. on p. 5).
- [24] Thermtest. *Top 10 Thermally Conductive Materials*. Thermtest Inc., June 2021. url: <https://thermtest.com/thermal-resources/top-10-resources/top-10-thermally-conductive-materials> (visited on 08/26/2022) (cit. on p. 5).
- [25] W. Contributors. *Transition metal dichalcogenide monolayers*. Wikipedia, Aug. 2022. url: https://en.wikipedia.org/wiki/Transition_metal_dichalcogenide_monolayers (visited on 08/26/2022) (cit. on p. 5).
- [26] M. Li et al. *Lattice constants of MoS₂*. Experimental study, modeling of atomic-scale friction in zigzag, and armchair lattice orientations of MoS₂, Apr. 2016. url: https://www.researchgate.net/publication/301645841_Experimental_study_and_modeling_of_atomic-scale_friction_in_zigzag_and_armchair_lattice_orientations_of_MoS_2 (visited on 08/26/2022) (cit. on p. 5).
- [27] Y. Li et al. *MoS₂ with structure tuned photocatalytic ability for degradation of methylene blue*. ResearchGate, Aug. 2019. url: https://www.researchgate.net/publication/335081923_MoS_2_with_structure_tuned_photocatalytic_ability_for_degradation_of_methylene_blue (visited on 08/26/2022) (cit. on p. 5).

- [28] A. Castellanos-Gomez et al. "Elastic Properties of Freely Suspended MoS₂ Nanosheets". In: *Advanced Materials* 24 (Jan. 2012), pp. 772–775. doi: 10.1002/adma.201103965. url: <https://onlinelibrary.wiley.com/doi/full/10.1002/adma.201103965> (visited on 08/26/2022) (cit. on p. 5).
- [29] M. Velicky and P. Toth. "From two-dimensional materials to their heterostructures: An electrochemist's perspective". In: *Applied Materials Today* 8 (Sept. 2017), pp. 68–103. doi: 10.1016/j.apmt.2017.05.003 (cit. on p. 5).
- [30] M. Zulfiqar et al. "Intrinsic Thermal conductivities of monolayer transition metal dichalcogenides MX₂ (M = Mo, W; X = S, Se, Te)". In: *Scientific Reports* 9 (Mar. 2019). doi: 10.1038/s41598-019-40882-2. url: <https://www.nature.com/articles/s41598-019-40882-2> (visited on 08/26/2022) (cit. on p. 5).
- [31] D. Concepts. *MoSe2 - Molybdenum Diselenide*. Hqgraphene.com, 2017. url: <http://www.hqgraphene.com/MoSe2.php> (visited on 08/26/2022) (cit. on p. 5).
- [32] A. Eftekhari. "Molybdenum diselenide (MoSe₂) for energy storage, catalysis, and optoelectronics". In: *Applied Materials Today* 8 (Sept. 2017), pp. 1–17. doi: 10.1016/j.apmt.2017.01.006. url: <https://www.sciencedirect.com/science/article/pii/S2352940716302475> (visited on 08/26/2022) (cit. on p. 5).
- [33] X. Wang et al. "Mechanical properties of molybdenum diselenide revealed by molecular dynamics simulation and support vector machine". In: *Physical Chemistry Chemical Physics* 21 (2019), pp. 9159–9167. doi: 10.1039/c8cp07881e. url: <https://pubmed.ncbi.nlm.nih.gov/30801579/> (visited on 08/26/2022) (cit. on p. 5).
- [34] J. Shang et al. "The electronic and optical properties of Tungsten Disulfide under high pressure". In: *Chemical Physics Letters* 651 (May 2016), pp. 257–260. doi: 10.1016/j.cplett.2016.03.053. url: <https://www.sciencedirect.com/science/article/pii/S0009261416301762> (visited on 08/26/2022) (cit. on p. 5).
- [35] A. Sobczynski et al. "Tungsten disulfide: a novel hydrogen evolution catalyst for water decomposition". In: *The Journal of Physical Chemistry* 92 (Apr. 1988), pp. 2311–2315. doi: 10.1021/j100319a042. (Visited on 08/26/2022) (cit. on p. 5).
- [36] A. Falin et al. "Mechanical Properties of Atomically Thin Tungsten Dichalcogenides: WS₂, WSe₂, and WTe₂". In: *ACS Nano* 15 (Jan. 2021), pp. 2600–2610. doi: 10.1021/acsnano.0c07430. (Visited on 08/26/2022) (cit. on p. 5).
- [37] R. Yu, V. Pruneri, and F. J. García de Abajo. "Resonant Visible Light Modulation with Graphene". In: *ACS Photonics* 2.4 (2015), pp. 550–558. doi: 10.1021/ph5004829 (cit. on p. 6).

- [38] B. Guo et al. “Graphene Doping: A Review”. In: *Insciences J.* 1 (2013), pp. 80–89. url: <https://journal.insciences.org/1664-171x-1-2-80/> (visited on 08/26/2022) (cit. on p. 6).
- [39] M. Engel et al. “Light–matter interaction in a microcavity-controlled graphene transistor”. In: *Nature Communications* 3.1 (2012). doi: 10.1038/ncomms1911 (cit. on pp. 6, 7).
- [40] P. Jia, F. Pan, and T. Chen. “Effect of oxygen plasma etching on graphene’s mechanical and electrical properties”. In: *IOP Conference Series: Materials Science and Engineering* 182 (Mar. 2017), p. 012030. doi: 10.1088/1757-899x/182/1/012030. url: <https://doi.org/10.1088/1757-899x/182/1/012030> (cit. on p. 6).
- [41] N. M. Tran et al. “Observation of the nonlinear Wood’s anomaly on periodic arrays of nickel nanodimers”. In: *Physical Review B* 98 (Nov. 2018) (cit. on p. 7).
- [42] D. Marcuse. *Light transmission optics /2nd edition/*. 1982 (cit. on p. 7).
- [43] M. Abramowitz and M. W. Davidson. *Diffraction of Light*. Olympus-lifescience.com, 2020. url: <https://www.olympus-lifescience.com/en/microscope-resource/primer/lightandcolor/diffraction/> (visited on 08/28/2022) (cit. on pp. 7, 8).
- [44] Newport. *Diffraction Grating Physics*. Newport - Photonic Solutions, 2020. url: <https://www.newport.com/n/diffraction-grating-physics> (visited on 08/28/2022) (cit. on p. 8).
- [45] E. Udd and W. B. Spillman Jr. “Diffraction Grating Theory”. In: *Field Guide to Fiber Optic Sensors*. SPIE, 2014, p. 40. doi: 10.1117/3.1002803.ch40. url: <https://www.spiedigitallibrary.org/ebooks/FG/Field-Guide-to-Fiber-Optic-Sensors/Diffraction-Grating-Theory/Diffraction-Grating-Theory/10.1117/3.1002803.ch40?SSO=1> (visited on 08/28/2022) (cit. on p. 9).
- [46] A. Hessel and A. A. Oliner. “A New Theory of Wood’s Anomalies on Optical Gratings”. In: *Appl. Opt.* 4.10 (Oct. 1965), pp. 1275–1297. doi: 10.1364/AO.4.001275. url: <http://www.osapublishing.org/ao/abstract.cfm?URI=ao-4-10-1275> (cit. on p. 9).
- [47] D. Rhee, S. Deng, and T. W. Odom. “Soft skin layers for reconfigurable and programmable nanowrinkles”. In: *Nanoscale* 12 (47 Dec. 2020), pp. 23920–23928. issn: 20403372. doi: 10.1039/d0nr07054h (cit. on pp. 9, 11, 20, 23).
- [48] Q. Wang and X. Zhao. “A three-dimensional phase diagram of growth-induced surface instabilities”. In: *Scientific Reports* 5.iv (2015), pp. 1–10. issn: 20452322. doi: 10.1038/srep08887 (cit. on p. 10).
- [49] E. Moyroud et al. “Disorder in convergent floral nanostructures enhances signalling to bees”. In: *Nature* 550 (Oct. 2017), pp. 469–474. doi: 10.1038/nature24285. url: <https://www.nature.com/articles/nature24285#citeas> (visited on 10/27/2022) (cit. on p. 10).

- [50] C. Kim et al. *Tribology and Lubricants A Review on Transfer Process of Two-dimensional Materials*. 2020. url: [10.9725/ks.2020.36.1.1](https://doi.org/10.9725/ks.2020.36.1.1) (cit. on pp. 11–13).
- [51] N. Instruments. *Atomic Force Microscopy*. Nanoscience Instruments, July 2022. url: <https://www.nanoscience.com/techniques/atomic-force-microscopy/> (visited on 08/25/2022) (cit. on p. 14).
- [52] O. Instruments. *AFM: Exploring Tapping Mode and AM-FM*. Oxford Instruments, 2022. url: <https://afm.oxinst.com/outreach/tapping-mode-for-afm-am-fm> (visited on 08/25/2022) (cit. on p. 14).
- [53] B. Zheng et al. “Identifying Key Factors towards Highly Reflective Silver Coatings”. In: *Advances in Materials Science and Engineering 2017* (2017), pp. 1–12. doi: [10.1155/2017/7686983](https://doi.org/10.1155/2017/7686983). url: <https://www.hindawi.com/journals/amse/2017/7686983/> (visited on 08/25/2022) (cit. on p. 16).
- [54] G. Silveira. *Microscopia Óptica: O que é e quais as informações obtidas neste ensaio?* Afinko, Sept. 2020. url: <https://afinkopolimeros.com.br/ensaio-de-microscopia-optica/> (visited on 08/25/2022) (cit. on p. 16).
- [55] O. I. Olubiyi et al. “Advances in Molecular Imaging for Surgery”. In: *Image-Guided Neurosurgery* (2015), pp. 407–439. doi: [10.1016/b978-0-12-800870-6.00017-0](https://doi.org/10.1016/b978-0-12-800870-6.00017-0). url: <https://www.sciencedirect.com/topics/neuroscience/raman-spectroscopy> (visited on 08/25/2022) (cit. on p. 17).
- [56] G. Giridhar, R. Manepalli, and G. Apparao. “Confocal Raman Spectroscopy”. In: *Spectroscopic Methods for Nanomaterials Characterization* (2017), pp. 141–161. doi: [10.1016/b978-0-323-46140-5.00007-8](https://doi.org/10.1016/b978-0-323-46140-5.00007-8). url: <https://www.sciencedirect.com/science/article/pii/B9780323461405000078> (visited on 08/25/2022) (cit. on p. 17).
- [57] C. E. Lyman et al. *Scanning Electron Microscopy, X-Ray Microanalysis, and Analytical Electron Microscopy*. Springer US, 1990, p. 244. doi: [10.1007-978-1-4613-0635-1](https://doi.org/10.1007-978-1-4613-0635-1). url: <https://link.springer.com/book/10.1007/978-1-4613-0635-1> (visited on 08/25/2022) (cit. on p. 17).
- [58] E. Suzuki. “High-resolution scanning electron microscopy of immunogold-labelled cells by the use of thin plasma coating of osmium”. In: *Journal of Microscopy* 208 (Dec. 2002), pp. 153–157. doi: [10.1046/j.1365-2818.2002.01082.x](https://doi.org/10.1046/j.1365-2818.2002.01082.x). url: <https://onlinelibrary.wiley.com/doi/abs/10.1046/j.1365-2818.2002.01082.x> (visited on 08/25/2022) (cit. on p. 17).
- [59] V. Dusevich, J. Purk, and J. Eick. “Choosing the Right Accelerating Voltage for SEM (An Introduction for Beginners)”. In: *Microscopy Today* 18 (Jan. 2010), pp. 48–52. doi: [10.1017/s1551929510991190](https://doi.org/10.1017/s1551929510991190). url: <https://www.cambridge.org/core/services/aop-cambridge-core/content/view/C62A3149CA4AF541EB1FBCD681CBE79A/S15519>

- 29510991190a.pdf/choosing-the-right-accelerating-voltage-for-sem-an-introduction-for-beginners.pdf (cit. on p. 17).
- [60] C. E. Lyman et al. *Scanning Electron Microscopy, X-Ray Microanalysis, and Analytical Electron Microscopy*. Springer US, 1990, p. 5. doi: 10.1007-978-1-4613-0635-1. url: <https://link.springer.com/book/10.1007/978-1-4613-0635-1> (visited on 08/25/2022) (cit. on p. 17).
- [61] W. Contributors. *Solar irradiance*. Wikipedia, Aug. 2022. url: https://en.wikipedia.org/wiki/Solar_irradiance#/media/File:Solar_spectrum_en.svg (visited on 08/23/2022) (cit. on p. 18).
- [62] F. Environmental. *Solar Radiation & Photosynthetically Active Radiation - Environmental Measurement Systems*. Environmental Measurement Systems, Jan. 2021. url: <https://www.fondriest.com/environmental-measurements/parameters/weather/photosynthetically-active-radiation/> (visited on 08/23/2022) (cit. on p. 18).
- [63] S. Scientific. *Blazed Holographic Grating | Spectrum Scientific*. Spectrum Scientific, Inc., Sept. 2019. url: <https://ssioptics.com/Blazed-Holographic-Grating/> (visited on 08/23/2022) (cit. on p. 19).
- [64] D. O'Shea et al. "Scalar Diffraction Theory". In: *Diffraction Optics: Design, Fabrication, and Test*. SPIE, 2003, pp. 17–35. doi: 10.1117/3.527861.ch2. url: <https://www.spiedigitallibrary.org/ebooks/TT/Diffraction-Optics-Design-Fabrication-and-Test/2/Design-of-Diffraction-Gratings/10.1117/3.527861.ch2?SSO=1&tab=ChapterArticleLink> (visited on 08/23/2022) (cit. on p. 19).
- [65] D. O'Shea et al. "Diffraction Lens Design". In: *Diffraction Optics*. SPIE, 2003, pp. 57–82. doi: 10.1117/3.527861.ch4. url: <https://www.spiedigitallibrary.org/ebooks/TT/Diffraction-Optics-Design-Fabrication-and-Test/4/Design-of-Diffraction-Gratings/10.1117/3.527861.ch4?SSO=1&tab=ChapterArticleLink> (visited on 08/23/2022) (cit. on p. 19).
- [66] S. Scientific. *Sinusoidal Holographic Grating | Spectrum Scientific*. Spectrum Scientific, Inc., Sept. 2019. url: <https://ssioptics.com/Sinusoidal-Holographic-Grating/> (visited on 08/23/2022) (cit. on p. 20).
- [67] W. Contributors. *Polydimethylsiloxane*. Wikipedia, Aug. 2022. url: https://en.wikipedia.org/wiki/Polydimethylsiloxane#cite_note-4 (visited on 08/23/2022) (cit. on p. 20).
- [68] S. Verlag. *Absorption spectra of PDMDPS (LS6943) and PDMS (Sylgard 184) elastomer...* ResearchGate, Apr. 2018. url: https://www.researchgate.net/figure/Absorption-spectra-of-PDMDPS-LS6943-and-PDMS-Sylgard-184-elastomer-AB-101-100-C_fig2_322467340 (visited on 08/23/2022) (cit. on p. 20).

- [69] K. Bush and A. A. Gertzman. "Process Development and Manufacturing of Human and Animal Acellular Dermal Matrices". In: *Skin Tissue Engineering and Regenerative Medicine*. Elsevier Inc., 2016, pp. 83–108. doi: 10.1016/b978-0-12-801654-1.00005-x. url: <https://www.sciencedirect.com/book/9780128016541/skin-tissue-engineering-and-regenerative-medicine#book-info> (visited on 08/23/2022) (cit. on p. 20).
- [70] S. H. Tan et al. "Oxygen plasma treatment for reducing hydrophobicity of a sealed polydimethylsiloxane microchannel". In: *Biomicrofluidics* 4 (Sept. 2010), p. 032204. doi: 10.1063/1.3466882. url: <https://www.ncbi.nlm.nih.gov/pmc/articles/PMC2967237/> (visited on 08/23/2022) (cit. on p. 21).
- [71] K. KaiSeng. *Methyl group in a polydimethylsiloxane (PDMS) network replaced by a silanol group*. ResearchGate, Apr. 2012. url: https://www.researchgate.net/figure/Methyl-group-in-a-Polydimethyl-Siloxane-PDMS-network-replaced-by-a-Silanol-group-a_fig1_224934859 (visited on 08/23/2022) (cit. on p. 21).
- [72] C. Brinker. "HYDROLYSIS AND CONDENSATION OF SILICATES: EFFECTS ON STRUCTURE". In: *Journal of Non-Crystalline Solids* 100 (1988), pp. 31–50. url: <https://brinkerlab.unm.edu/assets/publications/1985-1989-publications/brinkerhydrolysis1988.pdf> (visited on 08/23/2022) (cit. on p. 21).
- [73] H. Grave. "Condensation under Vacuum". In: ed. by W. Jorisch. *Vacuum Technology in the Chemical Industry*. John Wiley & Sons, Nov. 2014, pp. 15–34. doi: 10.1002/9783527653898.ch2. url: <https://onlinelibrary.wiley.com/doi/book/10.1002/9783527653898> (visited on 08/23/2022) (cit. on p. 21).
- [74] M. Morra et al. "On the aging of oxygen plasma-treated polydimethylsiloxane surfaces". In: *Journal of Colloid and Interface Science* 137 (June 1990), pp. 11–24. doi: 10.1016/0021-9797(90)90038-p. url: <https://www.sciencedirect.com/science/article/abs/pii/002197979090038P> (visited on 08/23/2022) (cit. on pp. 21, 22).
- [75] Z. Wang, A. A. Volinsky, and N. D. Gallant. "Crosslinking effect on polydimethylsiloxane elastic modulus measured by custom-built compression instrument". In: *Journal of Applied Polymer Science* 131 (June 2014), n/a–n/a. doi: 10.1002/app.41050. url: <https://onlinelibrary.wiley.com/doi/pdf/10.1002/app.41050> (visited on 08/24/2022) (cit. on p. 23).
- [76] Elsevier. *Fig. 1. Reflectance vs wavelength for gold [32]*. ResearchGate, Aug. 2011. url: https://www.researchgate.net/figure/Reflectance-vs-wavelength-for-gold-32_fig1_220251371 (visited on 08/24/2022) (cit. on pp. 31, 33).
- [77] L. Tang et al. "Chemical Vapor Deposition Growth of Two-Dimensional Compound Materials: Controllability, Material Quality, and Growth Mechanism". In: *Accounts of Materials Research* 2 (Dec. 2020), pp. 36–47. doi: 10.1021/accountsmr.0c00063. (Visited on 09/09/2022) (cit. on p. 34).

- [78] Y. Zhang, L. Zhang, and C. Zhou. "Review of Chemical Vapor Deposition of Graphene and Related Applications". In: *Accounts of Chemical Research* 46 (Mar. 2013), pp. 2329–2339. doi: 10.1021/ar300203n (cit. on p. 34).
- [79] J. de La Fuente. *Creating Graphene Via Chemical Vapour Deposition*. Graphenea, 2022. url: <https://www.graphenea.com/pages/cvd-graphene#.Yx8IZKHMJPY> (visited on 09/12/2022) (cit. on p. 34).
- [80] Y. Chen, X.-L. Gong, and J.-G. Gai. "Progress and Challenges in Transfer of Large-Area Graphene Films". In: *Advanced Science* 3 (Feb. 2016), p. 1500343. doi: 10.1002/advs.201500343. url: <https://onlinelibrary.wiley.com/doi/full/10.1002/advs.201500343> (visited on 09/16/2022) (cit. on p. 35).
- [81] D. Rhee et al. "Soft Skin Layers Enable Area-Specific, Multiscale Graphene Wrinkles with Switchable Orientations". In: *ACS Nano* 14 (1 Jan. 2020), pp. 166–174. issn: 1936086X. doi: 10.1021/acsnano.9b06325 (cit. on pp. 35, 52).
- [82] J. N. Lee, C. Park, and G. M. Whitesides. "Solvent Compatibility of Poly(dimethylsiloxane)-Based Microfluidic Devices". In: *Analytical Chemistry* 75 (Dec. 2003), pp. 6544–6554. doi: 10.1021/ac0346712. (Visited on 07/13/2019) (cit. on pp. 36, 37).
- [83] J. Liu, T. Liu, and S. Kumar. "Effect of solvent solubility parameter on SWNT dispersion in PMMA". In: *Polymer* 46 (Apr. 2005), pp. 3419–3424. doi: 10.1016/j.polymer.2005.02.086. url: <https://www.sciencedirect.com/science/article/pii/S0032386105002557> (visited on 09/09/2022) (cit. on p. 37).
- [84] I. Childres et al. "Raman Spectroscopy of Graphene and Related Materials". In: *New Developments in Photon and Materials Research*. Nova Science, June 2013. url: https://www.physics.purdue.edu/quantum/files/Raman_Spectroscopy_of_Graphene_NOVA_Childres.pdf (visited on 09/20/2022) (cit. on p. 40).
- [85] M. Wall. *The Raman Spectroscopy of Graphene and the Determination of Layer Thickness*. Thermo Fisher Scientific Inc., 2011. url: https://tools.thermofisher.com/content/sfs/brochures/AN52252_E%201111%20LayerThkns_H_1.pdf (visited on 09/20/2022) (cit. on p. 40).
- [86] R.-S. Ma et al. "Wrinkle-induced highly conductive channels in graphene on SiO₂/Si substrates". In: *Nanoscale* 12 (2020), pp. 12038–12045. doi: 10.1039/d0nr01406k. (Visited on 01/20/2021) (cit. on p. 45).
- [87] M. Barquins and J. Cognard. "Adhesion characteristics of gold surfaces". In: *Gold Bulletin* 19 (Sept. 1986), pp. 82–86. doi: 10.1007/bf03214647. url: <https://link.springer.com/article/10.1007/BF03214647> (visited on 09/28/2022) (cit. on p. 47).

- [88] D. H. Buckley. *Adhesion of Gold to Various Planes of Copper Studied With Leed*. ntrs.nasa.gov, June 1969. url: <https://ntrs.nasa.gov/api/citations/19690020029/downloads/19690020029.pdf> (visited on 10/04/2022) (cit. on p. 47).
- [89] T. Cusati et al. "Electrical properties of graphene-metal contacts". In: *Scientific Reports* 7 (July 2017). doi: 10.1038/s41598-017-05069-7. url: <https://www.nature.com/articles/s41598-017-05069-7> (visited on 09/28/2022) (cit. on p. 47).
- [90] R. Millikan and E. Bishop. *Elements of Electricity*. American Technical Society, 1917, p. 54. url: <https://archive.org/details/elementselectri00bishgoog/page/n67/mode/2up> (visited on 10/19/2022) (cit. on p. 49).
- [91] J. Leem et al. "Crack-assisted, localized deformation of van der Waals materials for enhanced strain confinement". In: *2D Materials* 6.4 (July 2019), p. 044001. doi: 10.1088/2053-1583/ab2eef. url: <https://dx.doi.org/10.1088/2053-1583/ab2eef> (cit. on p. 52).
- [92] RamanForLife. *PDMS raman spectrum*. Ramanlife.com, 2022. url: <https://ramanlife.com/library/pdms-raman/> (visited on 08/31/2022) (cit. on p. 77).
- [93] J. M. Dawes. *A typical Raman spectrum of fused silica*. Femtosecond Laser Modification of Fused Silica: The Effect of Writing Polarization on Si-O Ring Structure, 2022. doi: 10.1364/OE.16.020029. url: https://www.researchgate.net/publication/23493987_Femtosecond_Laser_Modification_of_Fused_Silica_The_Effect_of_Writing_Polarization_on_Si-O_Ring_Structure/figures?lo=1 (visited on 08/31/2022) (cit. on p. 77).
- [94] L. Lv. *Raman spectrum of monolayer graphene on a 2-mm SiO₂ substrate*. Monolayer graphene based organic optical terahertz modulator, Jan. 2017. url: https://www.researchgate.net/figure/Raman-spectrum-of-monolayer-graphene-on-a-2-mm-SiO2-substrate_fig1_312259788 (visited on 09/16/2022) (cit. on p. 77).

Pictures and Protocols

This appendix shows images of material and equipment used or protocols performed extraordinarily on the manufacturing and transfer methods covered throughout the dissertation.

A.1 Nanowrinkles' Fabrication



Figure 60: Elastomer base/curing agent kit



Figure 61: Conventional binder paper clamp



Figure 62: Cut PDMS strips on glass slides

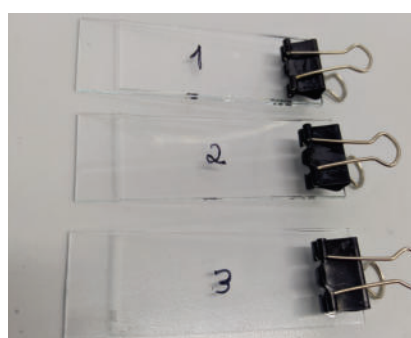


Figure 63: First fastened clamp on each sample

A.2 Graphene on Copper Wet Transfer Protocol

Attached is the protocol carried out to support laboratory users of the NAPS research group of the International Iberian Nanotechnology Laboratory on graphene transfers onto large-area samples by a wet method basis.

GRAPHENE WET TRANSFER

International Iberian Nanotechnology Laboratory

Created by José Gama (✉ jose.gama@inl.int) on November 29th, 2021
Edited by José Gama (✉ jose.gama@inl.int) on October 26th, 2022

Last edit October 26, 2022

PROTOCOL

Step A [Time required 65 minutes]

Copper substrate removal

- Cut a piece of the supply material with the desired dimension. It's fine to touch the material without a tweezer. Just make sure it stays the most flat possible. [1] [2]
- Fill an aquarium with FeCl_3 . [3]
- Put the cut piece into a FeCl_3 bath making sure it stays afloat with the PMMA surface faced-up for 1 straight hour. [4]

Step B [Time required 35 minutes]

Distilled Water Surface Cleaning

- Fill another aquarium with distilled water.
- Scoop the graphene over a stiff flat material. It was used $\text{Si}+\text{SiO}_2$ due to its high resistance to FeCl_3 and HCl corrosion and low reflectance (dark), which leads to a better positioning when catching the sample. [5]
- Gently dive the stiff material with the sample adhered onto distilled water expecting the sample to stay afloat. Let it rest for at least 30 minutes. [6]

Step C [Time required 15 minutes]

Graphene Acid Purifying

- Fill the lab tub with a 2% HCl solution. The tub makes it easier to dispose the acid.
- Repeat the previous step but from the distilled water to a HCl 2% (V) bath for a 10 minutes basis. The amount of exposure time depends on the desired properties of the graphene. [7] (View in Notes)

Step D [Time required 5 minutes]

Transfer into the sample

- Once again, using the same catch and release technique of the previous steps, pass the graphene from the HCl bath to a renewed distilled water bath.
- Now, repeat the scooping technique but with the target sample instead of the stiff flat material. [8]
- Let the sample naturally dry overnight tilted into lab paper. [9]

Step E [Time required 95 minutes]

PMMA removal

- Take the dried sample into an acetone bath for 90 minutes. That will depend on the PMMA film thickness of the supply. The sample can now sink in freely, the graphene should stay adhered to its surface.
- Take the sample out and rinse it with Isopropyl Alcohol and lastly with distilled water. Let it dry out. [10]

Protocol purpose:

This protocol aims to guide the user in the wet transfer process of Graphene grown on copper (Cu) with acrylic support film (PMMA) to sample surfaces of different dimensions.

EQUIPMENT

2 Aquariums 1 Lab Tub 1 Goblet

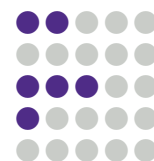
Scissors Tweezer Lab Paper

CHEMICALS

FeCl_3 H_2O 2% HCl
 $\text{C}_3\text{H}_6\text{O}$ (Acetone) $\text{C}_3\text{H}_8\text{O}$ (IPA)

DANGERS

Chemical Exposure
Physical Injury
Environmental Harm
Fire Hazards
Electrical Hazards



PROTECTIVE GEAR

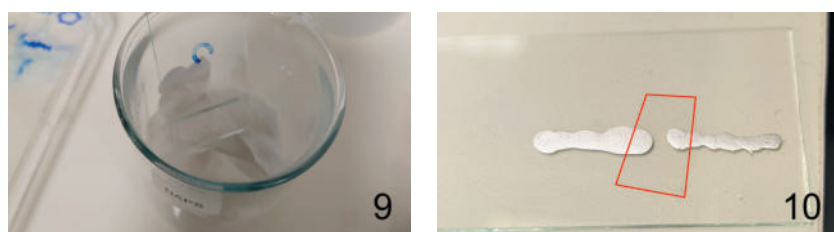
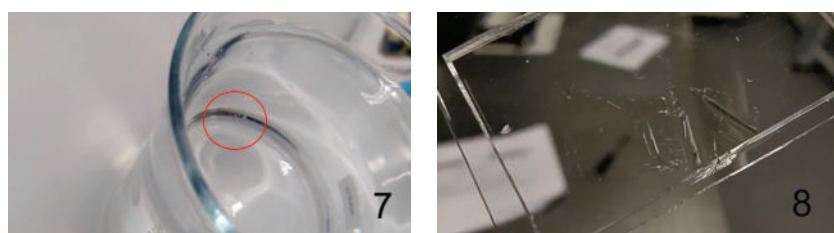
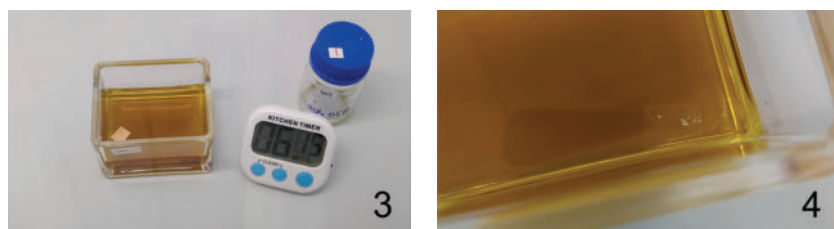
Laboratory Coat Gloves
Safety Goggles

SOURCES



References

- Chen, Yi, Xiao Lei Gong, and Jing Gang Gai (Aug. 2016). "Progress and Challenges in Transfer of Large-Area Graphene Films". In: *Advanced Science* 3 (8). ISSN: 21983844. DOI: [10.1002/advs.201500343](https://doi.org/10.1002/advs.201500343).

IMAGE APPENDIX



WARNINGS

-  **Corrosive Chemicals**
HCl 2% (V) and FeCl₃ are corrosive chemicals
-  **Drippy Containers**
The liquids might drip off the aquariums if not handled carefully

NOTES

Take notice that in the original Cu/Graphene/PMMA supply, the borders DO NOT have any graphene since it was where the duct tape was when depositing the PMMA support layer on the Cu/Graphene sample by spin-coating. Those borders should then also be cut off.

The FeCl₃ used can be stored on its aquarium for following transfers but remind that it should be filtered in order to maintain the most "variable-free" environment in the whole process. Typically the filtering is done after 5 transfers. The filtering should be something simple using some lab fibre diapers or even coffee filters.

The amount of exposure time of graphene in HCl influences its current chemical structure. For better optical properties, thus, more neat graphene is achieved after a higher exposure time since the acid will attack external bonds with, for example, remains of copper attached. On the other hand, higher exposure times also mean more carbon bonds damaged so the structure will deteriorate over time leading to less stability regarding mechanical and electrical properties.

PEOPLE TO CONTACT

[Martin Lopez-Garcia](#) for NAPS lab access.
[Francisca Guedes](#) about chemicals usage.
[Vitor Silva](#) for graphene supply.

A.3 Optoelectronic Experiments



Figure 64: *RS PRO™ Conductive Silver Ink.*

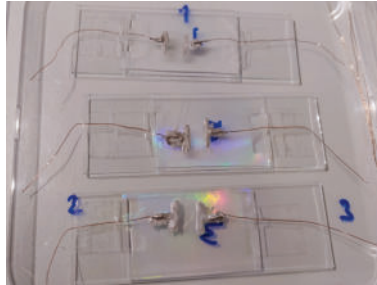


Figure 65: Conductive Silver Ink contact implementation on a batch of samples manufactured by the method mentioned in 3.2.

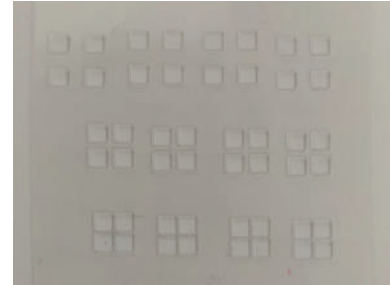


Figure 66: Test PET shadow mask with different inscribed layouts. Contact distances are 5, 1, and 0.2 mm, from top to bottom.

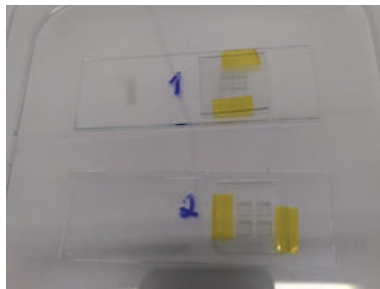


Figure 67: PET shadow mask placed on top of samples.

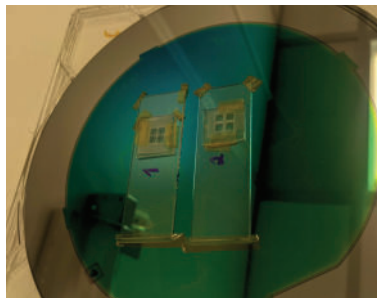


Figure 68: Samples attached to a silicon wafer before sputtering.

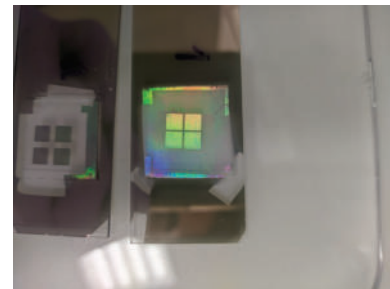


Figure 69: Light diffraction enhancement of sputtered gold contacts on a sample manufactured by the method mentioned in 3.2.

Statistical Analysis

B.1 Useful Equations

Arithmetic mean:

$$\bar{x} = \frac{1}{n} \sum_{i=0}^n x_i \quad (\text{B.1})$$

Standard deviation:

$$\sigma_x = \sqrt{\frac{1}{N-1} \sum_{i=1}^N (x_i - \bar{x})^2} \quad (\text{B.2})$$

Relative standard deviation:

$$\%_{\sigma} = \frac{\sigma}{\bar{x}} \times 100 \quad (\text{B.3})$$

Coefficient of determination:

$$R^2 = 1 - \frac{\sum_{i=0}^N (x_i - \bar{x})^2}{\sum_{i=0}^N (x_i - \hat{x}_i)^2} \quad (\text{B.4})$$

Relative error:

$$\delta_x = \frac{|x - \bar{x}|}{x} \times 100 \quad (\text{B.5})$$

B.2 Raw Data

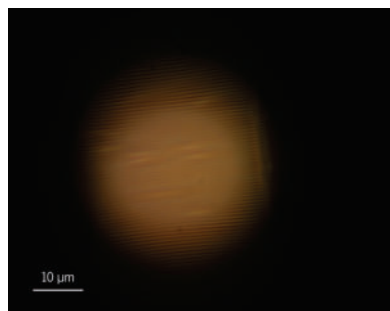


Figure 70: WB1.1 Spot 1, 40× objective BF

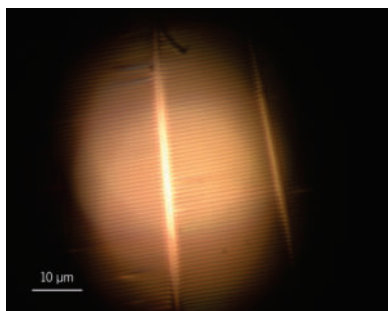


Figure 71: WB2.1 Spot 1, 40× objective BF

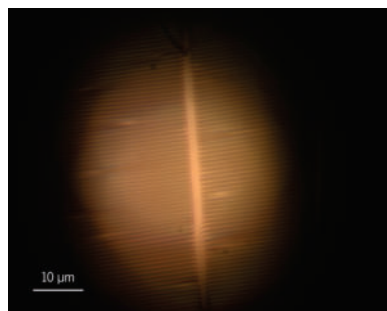


Figure 72: WB3.1 Spot 1, 40× objective BF

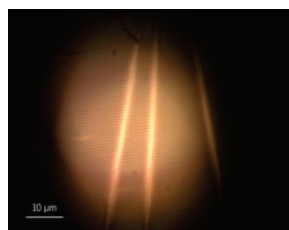


Figure 73: WB4.1 Spot 1, 40× objective BF

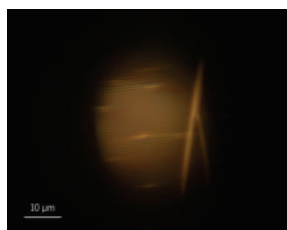


Figure 74: WD2.1 Spot 1, 40× objective BF

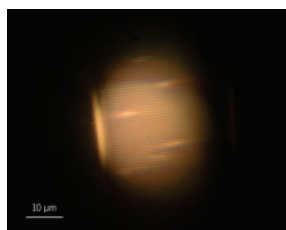


Figure 75: WD3.1 Spot 1, 40× objective BF

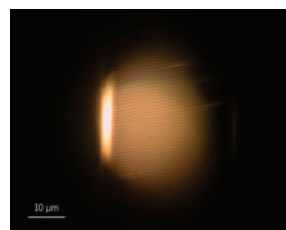


Figure 76: WD5.1 Spot 1, 40× objective BF

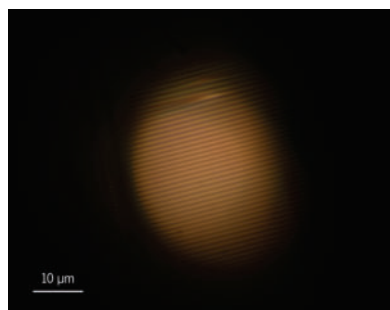


Figure 77: WD7.1 Spot 1, 40× objective BF

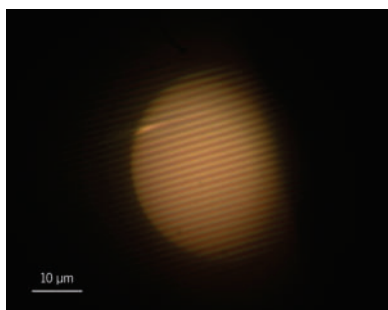


Figure 78: WD8.1 Spot 1, 40× objective BF

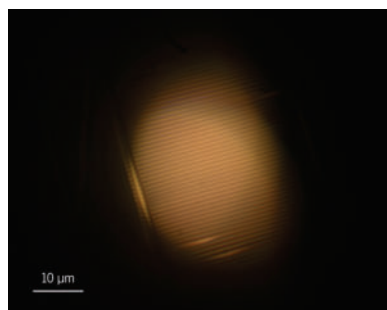


Figure 79: WD9.1 Spot 1, 40× objective BF

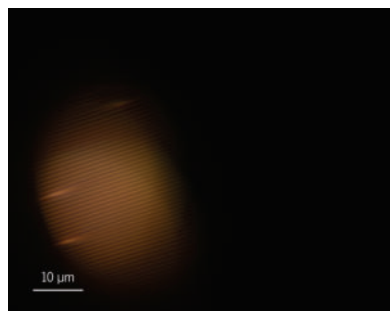


Figure 80: WD10.1 Spot 1, 40× objective BF

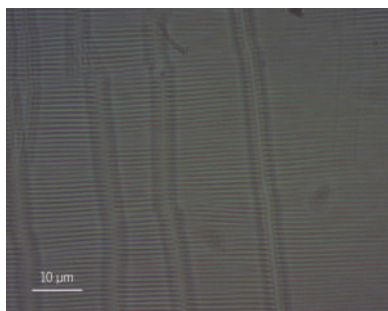


Figure 81: RB5.1 Spot 1, 40× objective DF

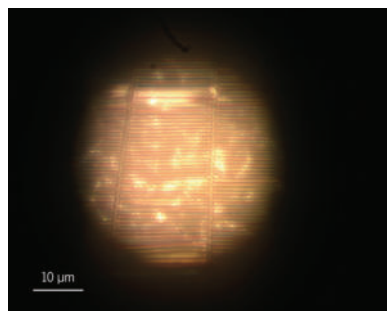


Figure 82: RB6.1 Spot 1, 40× objective BF

B.3 Processed Data

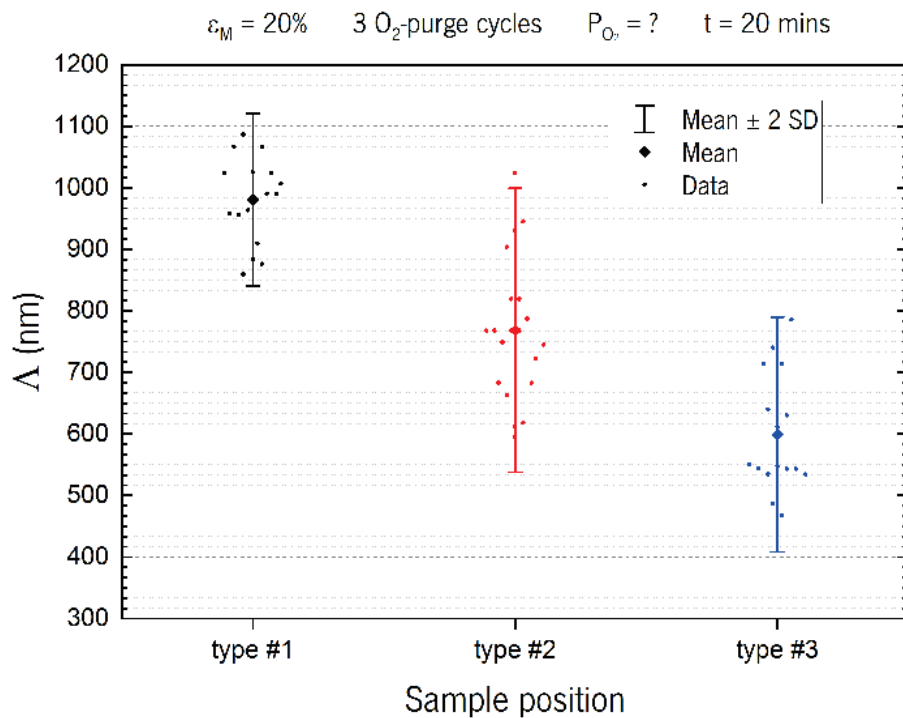


Figure 83: First calibration attempt of the oxygen plasma up time. Oxygen pressure was not considered.

Table 7: Values of Δ obtained from batches fabricated by the method mentioned in 2.3 with no delay time after plasma treatment (see appendix B.2) by the procedure shown in 1.3.3.

Wrinkles Batch	1			2		
	1	2	3	1	2	3
Δ_1 (nm)	764.19	693.72	564.17	855.15	612.44	567.33
Δ_2 (nm)	762.07	678.49	535.99	753.88	651.26	626.55
Δ_3 (nm)	764.16	645.45	547.18	773.76	665.32	523.39
Δ_4 (nm)	781.3	651.26	553.09	741.37	667.2	467.05

3			4		
1	2	3	1	2	3
845.22	703.98	523.39	781.3	657.95	543.06
848.11	784.97	526.84	724.08	695.31	565.41
927.09	707.56	588.06	803.98	663.92	544.34
900.03	707.56	565.41	775.3	686.92	535.99

Table 8: Statistical analysis of table 7.

Sample Type	$\bar{\Lambda}$	$2\sigma_{\Lambda}$	$\%_{\sigma}$
1	800.06	116.51	7.28
2	679.58	76.80	5.65
3	548.58	68.46	6.24

Table 9: Values of Λ obtained from batches fabricated by the method mentioned in 2.3 with varying delay time after plasma treatment (see appendix B.3) by the procedure shown in 1.3.3 and respective statistical analysis.

Wrinkles Delay (Resting Time)	2 (24h)			9 (24h vacuum)		
	Sample Type	1	2	3	4	5
Λ_1 (nm)	709.64	599.48	526.84	850.06	752.86	588.81
Λ_2 (nm)	731.35	672.44	533.72	850.06	727.93	580.14
Λ_3 (nm)	758.13	623.7	473.06	850.06	727.93	597.43
Λ_4 (nm)	685.31	649.95	532.35	827.85	719.1	586.34
$\bar{\Lambda}$ (nm)	721.11	636.39	516.49	844.51	731.96	588.18
$2\sigma_{\Lambda}$ (nm)	53.75	54.83	50.42	19.23	25.19	12.41
$\%_{\sigma}$	3.73	4.31	4.88	1.14	1.72	1.05

3 (48h)			10 (48h vacuum)			7 (72h)		
1	2	3	1	2	3	1	2	3
785.37	663.92	580.14	919.54	794.9	604.73	999.53	837.33	605.97
825.22	638.93	542.73	952.02	808.58	611.44	1024.38	822.2	590.46
815.46	649.95	585.49	943.14	801.93	592.2	1042.79	811.52	633.58
803.98	677.62	564.17	943.11	794.88	607.74	1011.71	801.51	613.3
807.51	657.61	568.13	939.45	800.07	604.03	1019.60	818.14	610.83
29.66	29.12	33.26	24.11	11.38	14.46	32.03	26.55	31.02
1.84	2.21	2.93	1.28	0.71	1.20	1.57	1.62	2.54

8 (72h vacuum)			5 (96h)		
1	2	3	1	2	3
996.57	837.34	613.85	1002.79	805.14	584.12
983.61	819.42	606.2	989.5	799.41	607.55
992.4	829.64	616.2	992.79	795.94	617.1
1001.22	854.93	595.85	1008.89	810.35	609.88
993.45	835.33	608.03	998.49	802.71	604.66
12.96	25.96	15.88	15.49	11.00	24.74
0.65	1.55	1.31	0.78	0.69	2.05

Table 10: Values of Λ obtained from batches fabricated by the method mentioned in 3.2 only on graphene sections (see appendix B.3) by the procedure shown in 1.3.3.

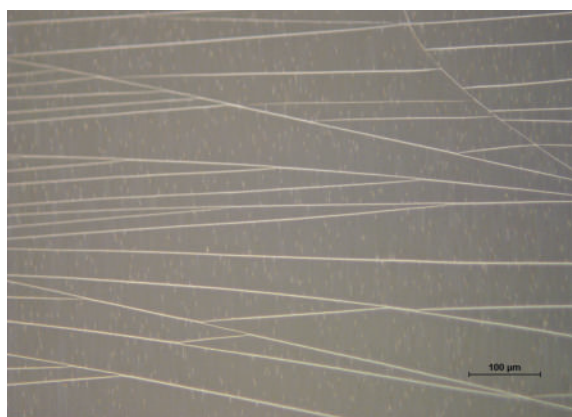
Recipe Batch	5			6		
	1	2	3	1	2	3
Λ_1 (nm)	1021.73	808.4	600.51	1015.02	801.51	633.3
Λ_2 (nm)	959.53	853	601.31	1015.02	798.53	612.44
Λ_3 (nm)	1023.86	863.53	695.3	1018.76	803.98	632.22
Λ_4 (nm)	1021.73	890.91	669.41	1028.8	852.02	635.02

Table 11: Statistical analysis of table 10.

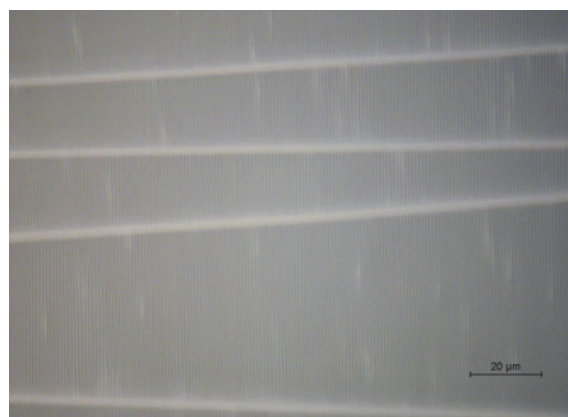
Sample Type	$\bar{\Lambda}$	$2\sigma_{\Lambda}$	$\%_{\sigma}$
1	1013.06	41.35	2.04
2	833.99	65.83	3.95
3	634.94	61.90	4.87

Additional Measurements

C.1 Optical Microscopy

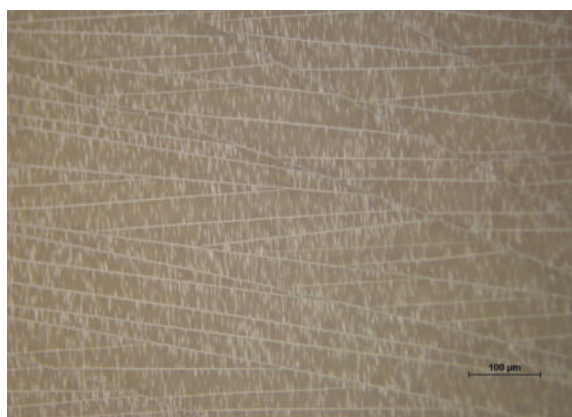


(a) 20× objective BF

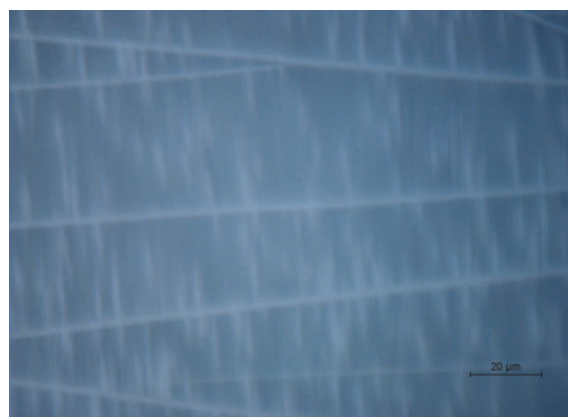


(b) 100× objective BF

Figure 84: Type #2 sample fabricated by the method mentioned in section 2.3.

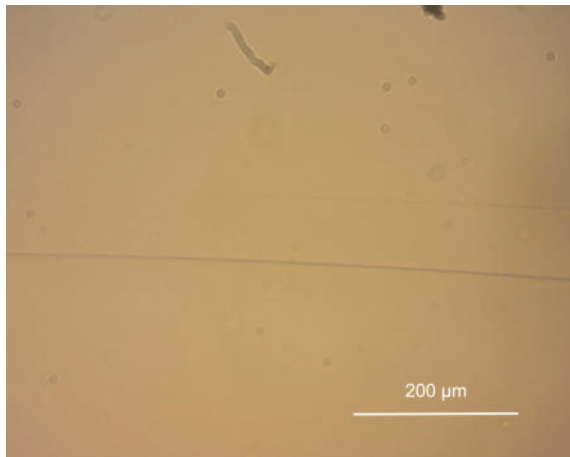


(a) 20× objective BF

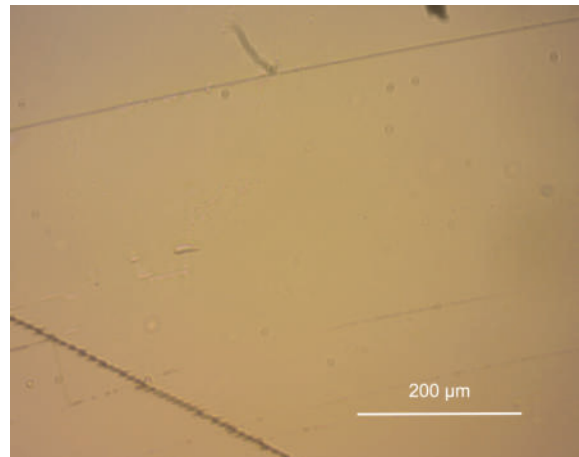


(b) 100× objective BF

Figure 85: Type #3 sample fabricated by the method mentioned in section 2.3.

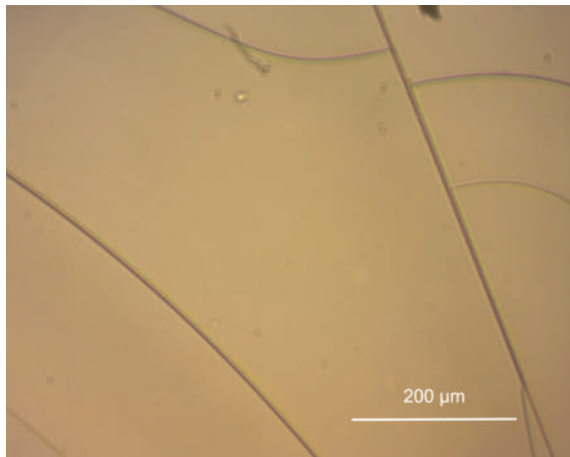


(a) Measured spot #1, 4× objective, DF.

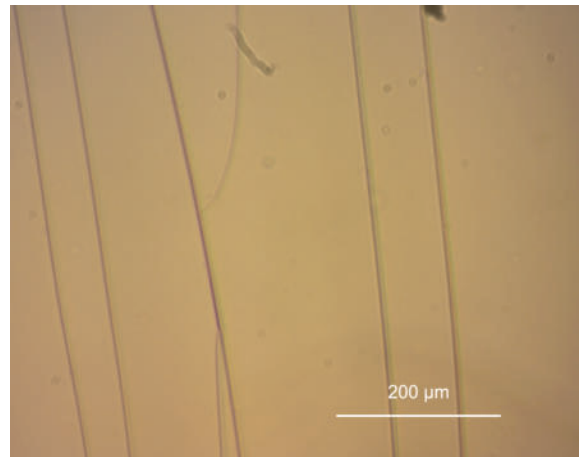


(b) Measured spot #3, 4× objective, DF.

Figure 86: Oxygen plasma-treated flat PDMS sample after pure acetone bath with intervals of 15 minutes.

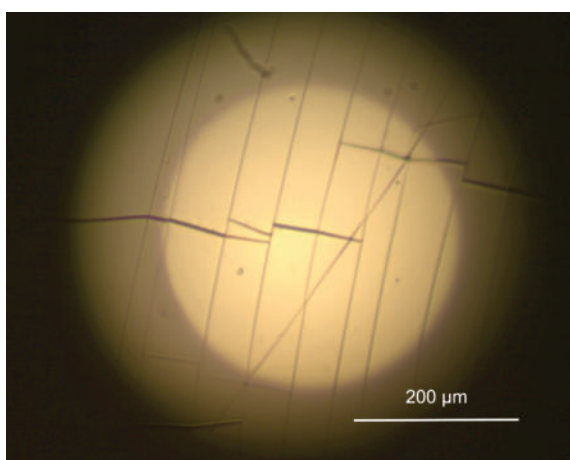


(a) Measured spot #1, 4× objective, DF.

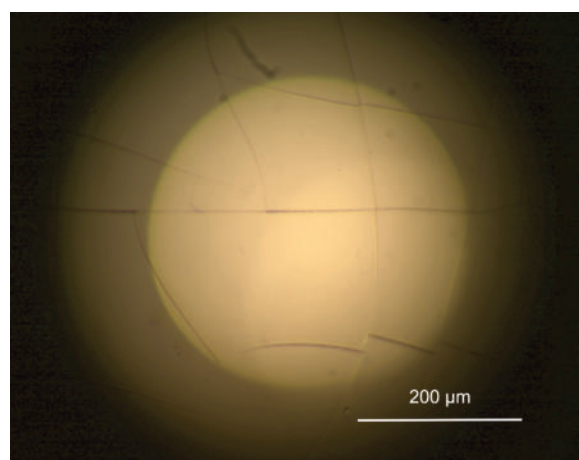


(b) Measured spot #3, 4× objective, DF.

Figure 87: Oxygen plasma-treated flat PDMS sample after pure acetone bath with intervals of 30 minutes.

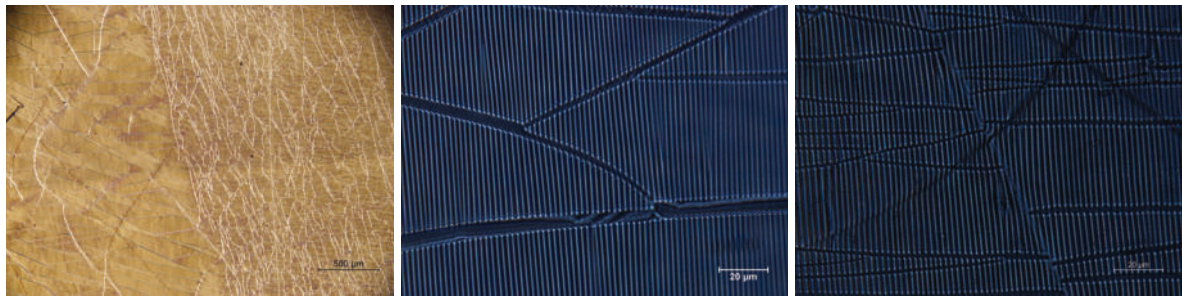


(a) Measured spot #1, 4× objective, BF.



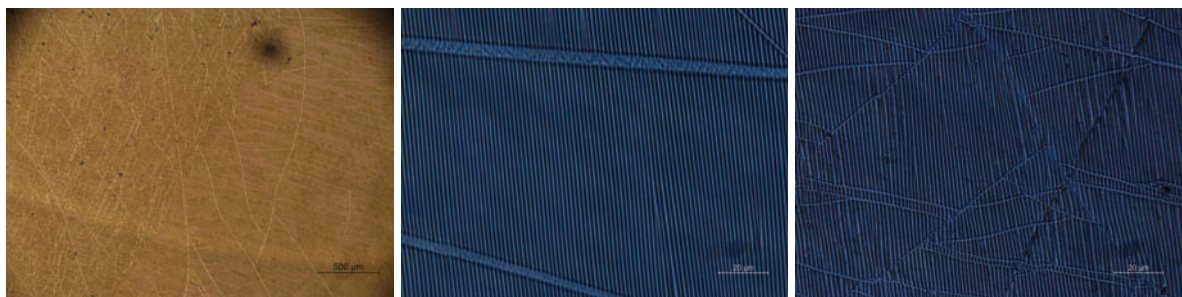
(b) Measured spot #3, 4× objective, BF.

Figure 88: Oxygen plasma-treated flat PDMS sample after pure acetone bath with intervals of 60 minutes.



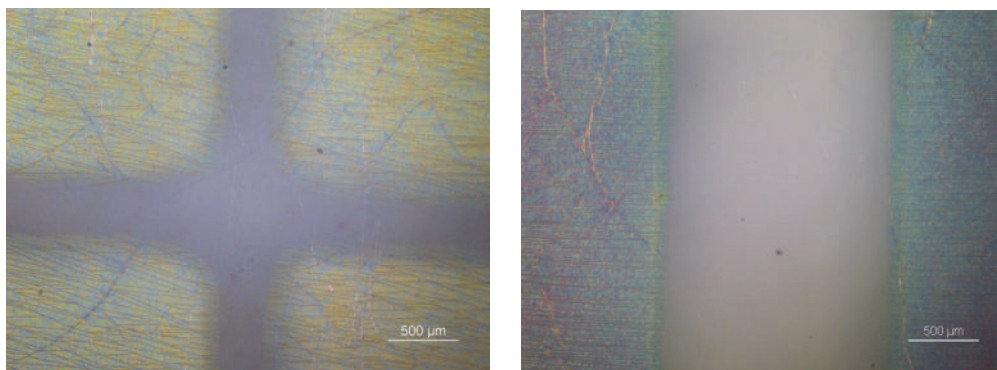
(a) 5× BF, graphene section border (b) 100× BF, section without graphene (c) 100× BF, section with graphene

Figure 89: Type #1 sample fabricated by the process mentioned in the section 3.2 overexposed with oxygen plasma.



(a) 5× BF, graphene section border (b) 100× BF, spot without graphene (c) 100× BF, spot with graphene

Figure 90: Type #2 sample fabricated by the process mentioned in the section 3.2 overexposed with oxygen plasma.



(a) Contacts distance of 200 μm

(b) Contacts distance of 1 mm

Figure 91: 5× objective images of samples fabricated by the method mentioned in section 3.2 with overexposed oxygen plasma. Colorful zones are sputtered gold contacts.

C.2 Atomic Force Microscopy

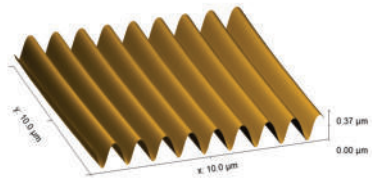


Figure 92: 3D representation of type #1 sample of WD7

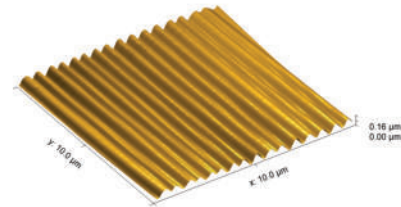


Figure 93: 3D representation of type #3 sample of WD7

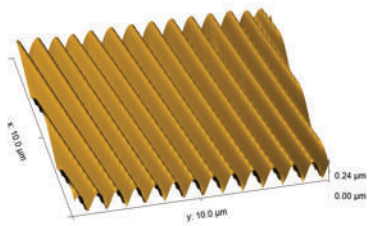


Figure 94: 3D representation of type #1 sample of WD2

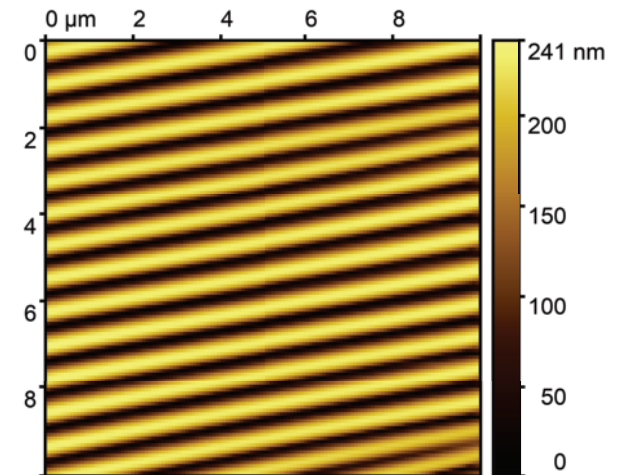


Figure 95: 2D topographical plot of type #1 sample of WD2

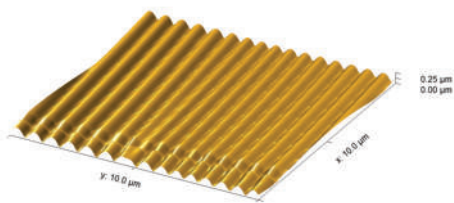


Figure 96: 3D representation of type #2 sample of WD2

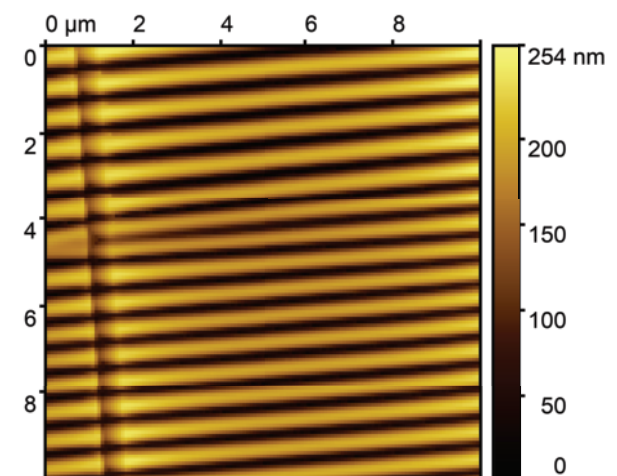


Figure 97: 2D topographical plot of type #2 sample of WD2

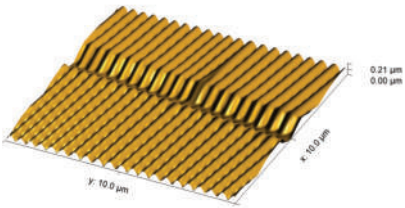


Figure 98: 3D representation of type #3 sample of WD2

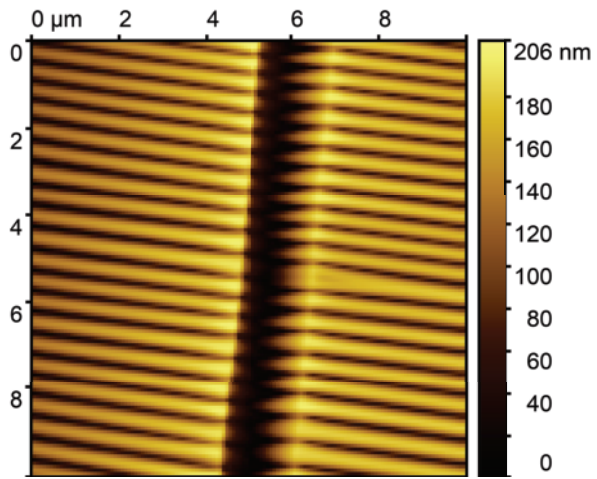


Figure 99: 2D topographical plot of type #3 sample of WD2

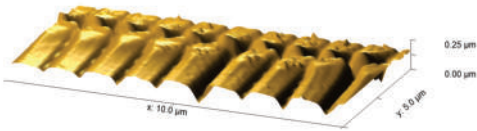


Figure 100: 3D representation of type #1 sample of RB6

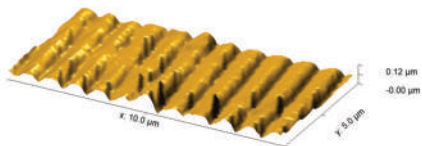


Figure 101: 3D representation of type #2 sample of RB6

C.3 Raman's Spectroscopy

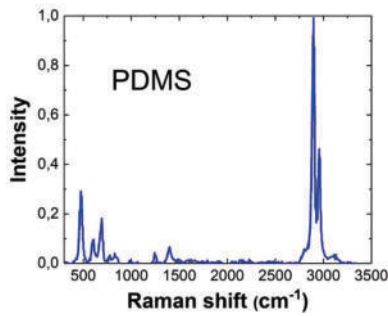


Figure 102: Theoretical Raman's spectrum of pristine PDMS. Retrieved from [92].

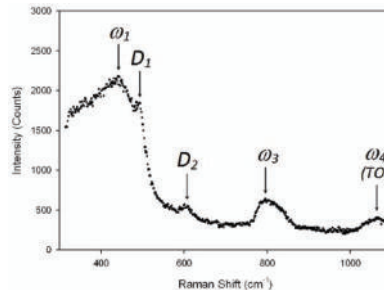


Figure 103: Typical Raman's spectrum of fused silica. Retrieved from [93].

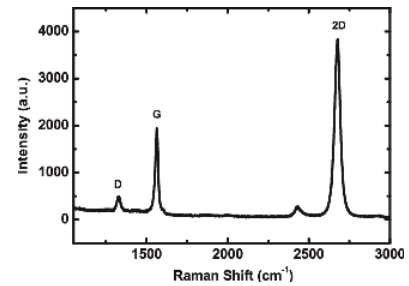


Figure 104: Raman's spectrum of monolayer graphene on a 2 mm SiO₂ substrate. Retrieved from [94].

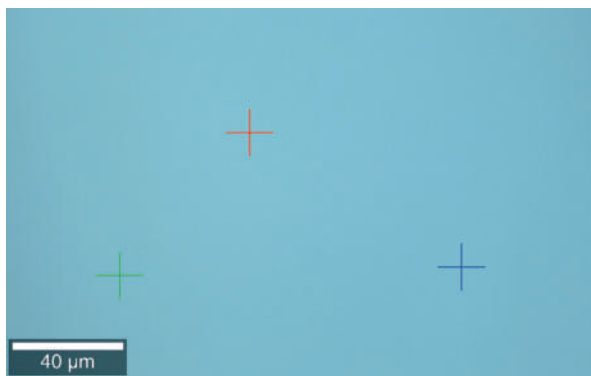


Figure 105: Measured section of flat pristine PDMS. Crosses are measured spots.

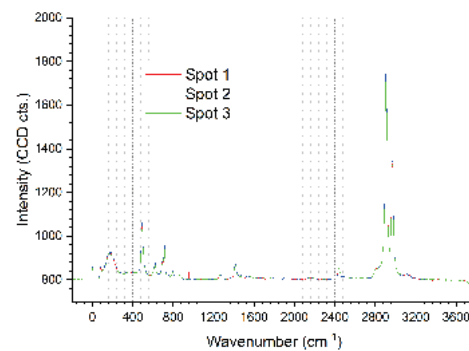


Figure 106: Raman's spectra obtained on flat pristine PDMS. Integration time of 2s, 10 acquisitions.



Figure 107: Measured section of oxygen plasma-treated flat PDMS. Crosses are measured spots.

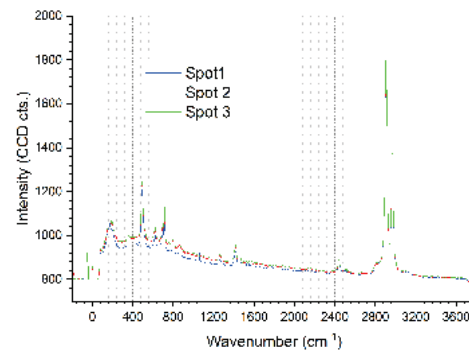


Figure 108: Raman's spectra obtained on flat treated PDMS. Integration time of 2s, 10 acquisitions.

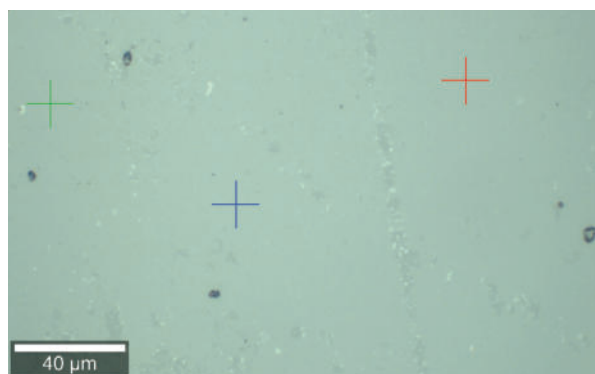


Figure 109: Measured section of graphene transferred onto a flat glass substrate. Crosses are measured spots.

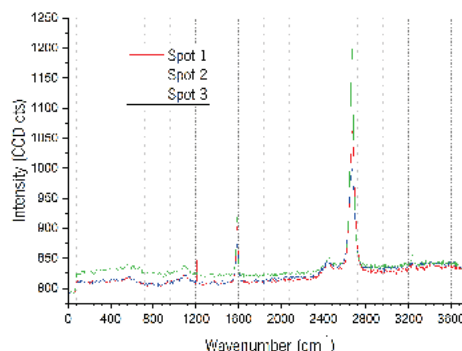


Figure 110: Raman's spectra obtained on graphene transferred onto a flat glass substrate. Integration time of 1s, 10 acquisitions.

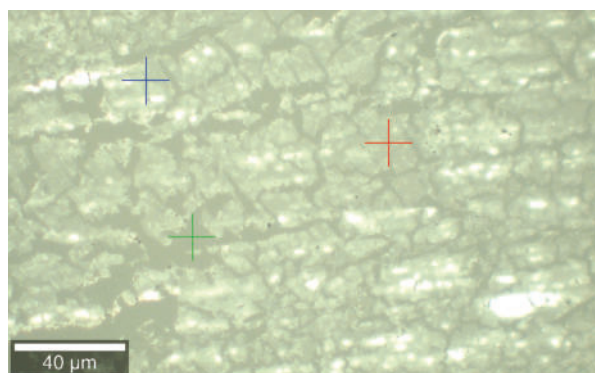


Figure 111: Measured section of graphene transferred onto a flat untreated PDMS substrate. Crosses are measured spots.

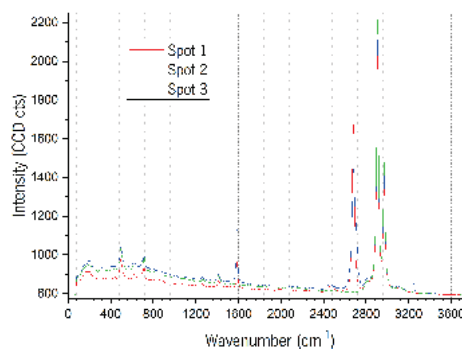


Figure 112: Raman's spectra obtained on graphene transferred onto a flat untreated PDMS substrate. Integration time of 1s, 10 acquisitions.

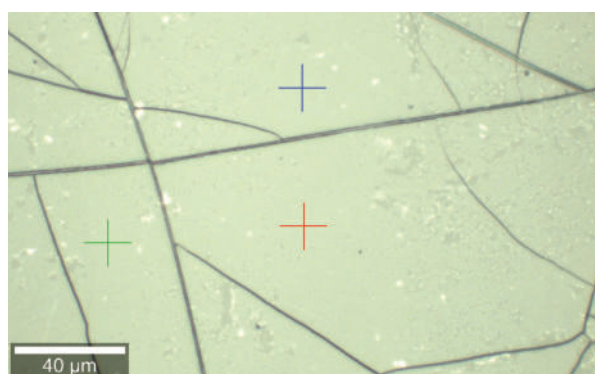


Figure 113: Measured section of graphene transferred onto a flat treated PDMS substrate with no resting time. Crosses are measured spots.

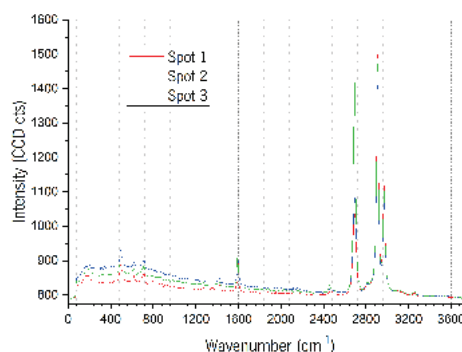


Figure 114: Raman's spectra obtained on graphene transferred onto a flat treated PDMS substrate with no resting time. Integration time of 1s, 10 acquisitions.

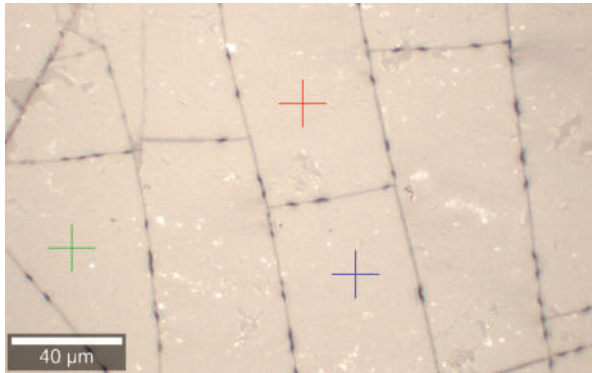


Figure 115: Measured section of graphene transferred onto a flat treated PDMS substrate with 72h of resting time. Crosses are measured spots.

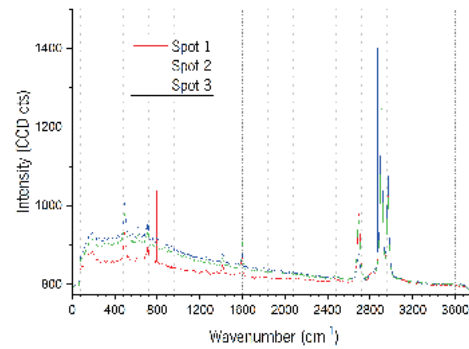


Figure 116: Raman's spectra obtained on graphene transferred onto a flat treated PDMS substrate with 72h of resting time. Integration time of 1s, 10 acquisitions.

C.4 Scanning Electron Microscopy

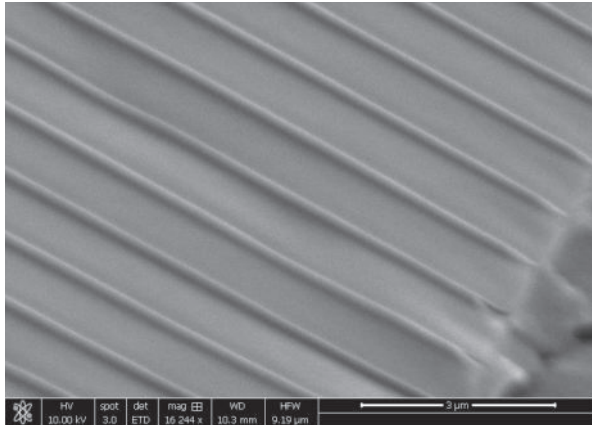


Figure 117: WD7.1, 16 244× mag., 10 kv at SEM

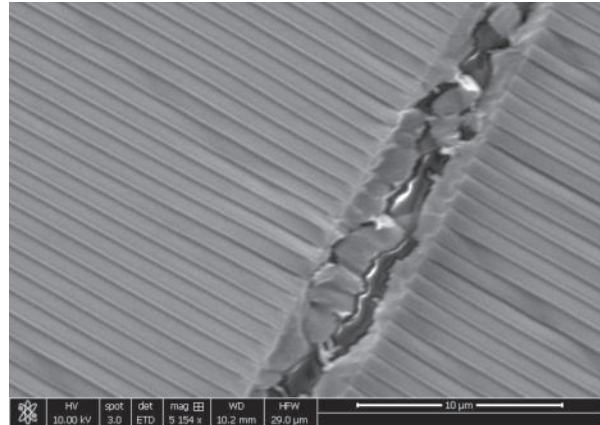


Figure 118: WD7.1, 5 154× mag., 10 kv at SEM

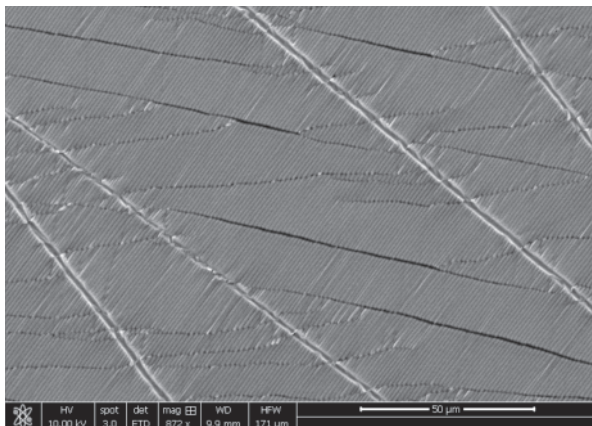


Figure 119: WD7.2, 872× mag., 10 kv at SEM

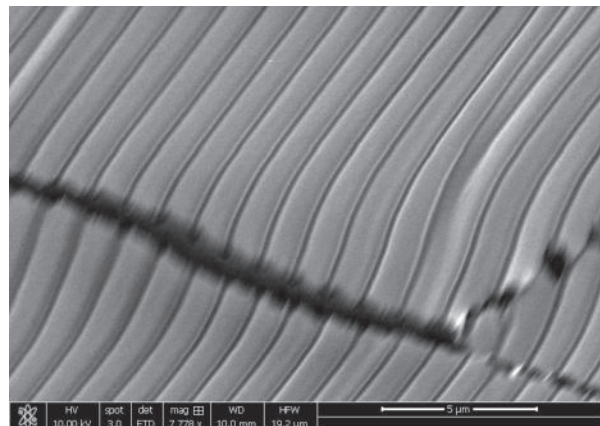


Figure 120: WD7.2, 7 778× mag., 10 kv at SEM

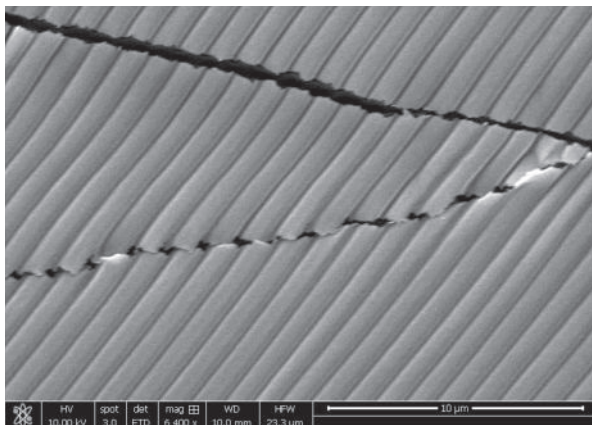


Figure 121: WD7.2, 6 400× mag., 10 kv at SEM

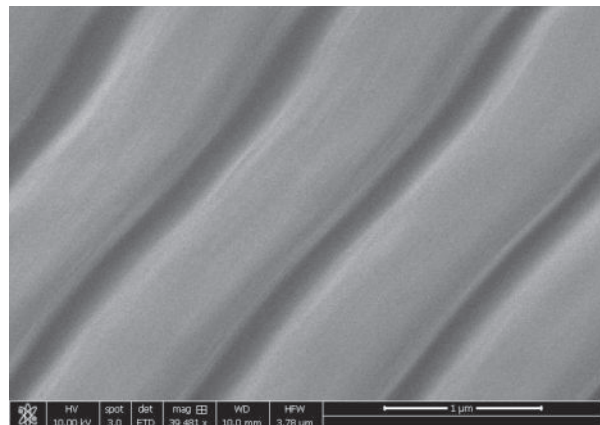


Figure 122: WD7.2, 39 481× mag., 10 kv at SEM

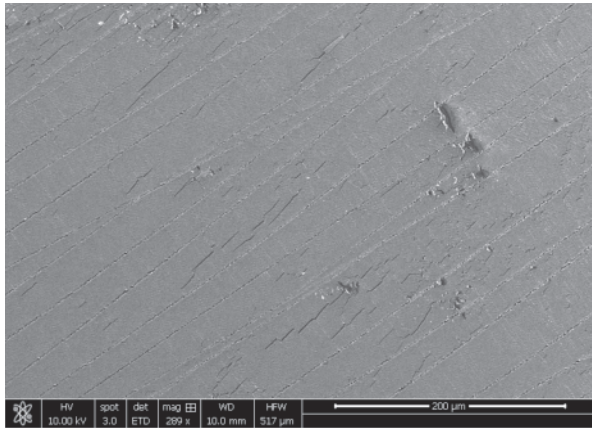


Figure 123: WD7.3, 289× mag., 10 kv at SEM

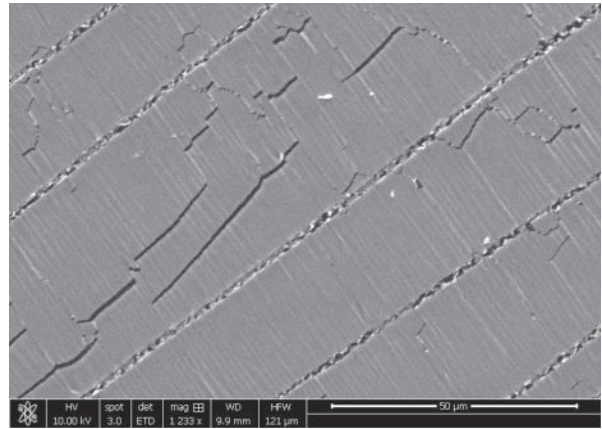


Figure 124: WD7.3, 1 233× mag., 10 kv at SEM

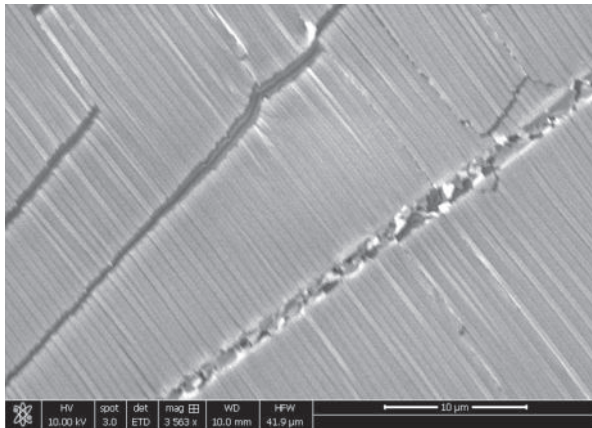


Figure 125: WD7.3, 3 563× mag., 10 kv at SEM

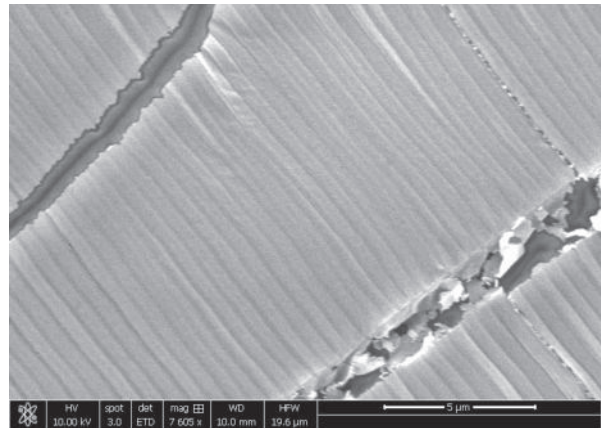


Figure 126: WD7.3, 7 605× mag., 10 kv at SEM

C.5 Angular Reflection Spectrophotometry

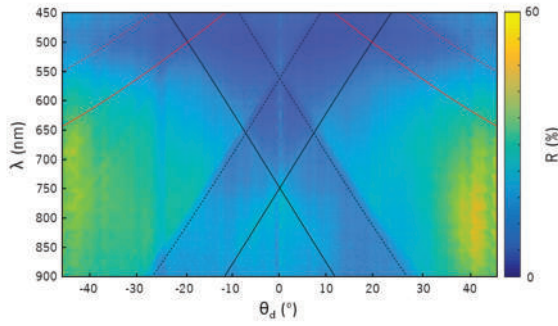


Figure 127: ARS RB6.2 (no graphene)

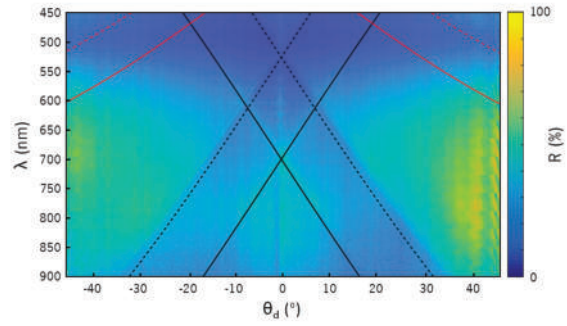


Figure 128: ARS RB6.3 (no graphene)

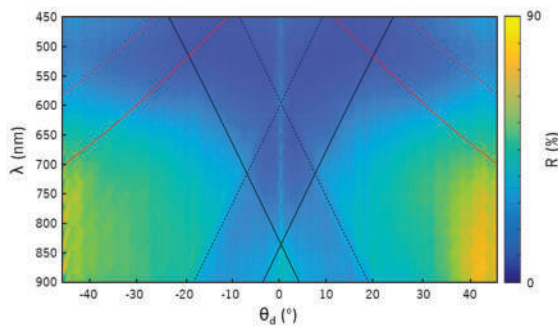


Figure 129: ARS WD2.1

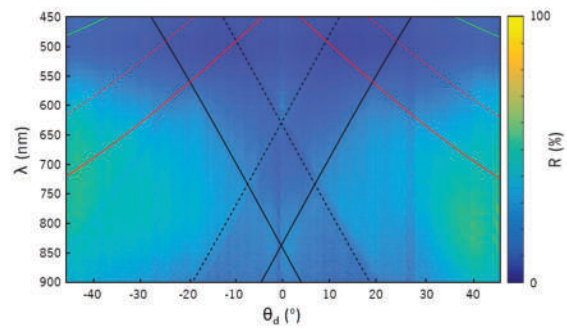


Figure 130: ARS WD9.1

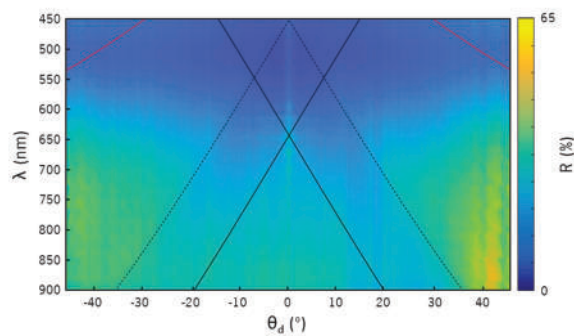


Figure 131: ARS WD2.2

